ZÁPADOČESKÁ UNIVERZITA V PLZNI

FAKULTA ELEKTROTECHNICKÁ

Katedra materiálů a technologií

DIPLOMOVÁ PRÁCE

Generators Outer Corona Protection and Semi conductive slot coating

Luboš Polančík **2021**

ZÁPADOČESKÁ UNIVERZITA V PLZNI
Fakulta elektrotechnická
Akademický rok: 2020/2021

ZADÁNÍ DIPLOMOVÉ PRÁCE
(projektu, uměleckého díla, uměleckého výkonu)

Jméno a příjmení:	**Bc. Luboš POLANČÍK**
Osobní číslo:	**E19N0042P**
Studijní program:	**N2612 Elektrotechnika a informatika**
Studijní obor:	**Komerční elektrotechnika**
Téma práce:	**Koronové ochrany čel a drážkové části vinutí generátorů**
Zadávající katedra:	**Katedra materiálů a technologií**

Zásady pro vypracování

Diplomová práce je realizována ve spolupráci se zahraničním výrobním podnikem. Jedná se o výrobce generátorů v Rakousku. Preferovaným jazykem zpracování diplomové práce je anglický jazyk.

1. Popište funkci a aplikaci vodivých a polovodivých ochran na tyčích statorového vinutí turbogenerátoru.
2. Specifikujte materiály použitelné pro tyto aplikace a proveďte přehled výrobců a typů materiálů.
3. Vyberte a popište možné vhodné diagnostické postupy měření ochrany proti koroně v drážkové části a na výstupu vinutí z drážky.
4. Na vzorcích koronových ochran proveďte měření vnitřní a povrchové rezistivity a výsledky podrobte korelační analýze.
5. Na základě naměřených a analyzovaných dat určete povrchový vodivostní profil koronové ochrany.

Proveďte celkové zhodnocení práce a jejích přínosů.

Rozsah diplomové práce: **40 – 60 stran**
Rozsah grafických prací: **podle doporučení vedoucího**
Forma zpracování diplomové práce: **tištěná/elektronická**

Seznam doporučené literatury:

1. Hauschild, W. High-Voltage Test and Measuring Techniques, Springer 2014
2. Küchler, A.: High Voltage Engineering, Springer 2017
3. Mentlík, V. a kol. Diagnostika elektrických zařízení, BEN 2008
4. Bouda, V.: Materiály pro elektrotechniku, ČVUT 2000
5. Elektronické informační zdroje

Vedoucí diplomové práce: **Ing. Josef Pihera, Ph.D.**
Katedra materiálů a technologií

Datum zadání diplomové práce: **9. října 2020**
Termín odevzdání diplomové práce: **27. května 2021**

L.S.

Prof. Ing. Zdeněk Peroutka, Ph.D.
děkan

Doc. Ing. Aleš Hamáček, Ph.D.
vedoucí katedry

V Plzni dne 9. října 2020

Dodatek k zadání Diplomové práce

Fakulty elektrotechnické ZČU v Plzni v akademickém roce 2020/2021

V souvislosti s krizovým opatřením vyhlášeným dle krizového zákona a mimořádným opatřením vydaným podle zvláštního zákona, na základě kterých došlo k omezení osobní přítomnosti studentů v prostorách vysoké školy a s ohledem na nutnost využití infrastruktury FEL při vypracování kvalifikační práce v období tohoto omezení a v plné míře s přihlédnutím k realizovatelnosti práce po dobu trvání tohoto omezení se v intencích čl. 54 odst. 4 Studijního a zkušebního řádu Západočeské univerzity v Plzni upravuje zadání práce takto:

Body 1, 2, 3, 5, 6 zůstávají v plném rozsahu.

1. Popište funkci a aplikaci vodivých a polovodivých ochran na tyčích statorového vinutí turbogenerátoru.
2. Specifikujte materiály použitelné pro tyto aplikace a proveďte přehled výrobců a typů materiálů.
3. Vyberte a popište možné vhodné diagnostické postupy měření ochrany proti koroně v drážkové části a na výstupu vinutí z drážky.
5. Na základě naměřených a analyzovaných dat určete povrchový vodivostní profil koronové ochrany.
6. Proveďte celkové zhodnocení práce a jejích přínosů.

Bod 4. původní znění

4. Na vzorcích koronových ochran proveďte měření vnitřní a povrchové rezistivity a výsledky podrobte korelační analýze.

je změněn na:

4. Na vzorcích koronových ochran proveďte měření povrchové rezistivity

Beru na vědomí a souhlasím.

V Plzni dne 7.5.2021

V Plzni dne 7.5.2021

Josef Pihera

Digitálně podepsal Josef Pihera
Datum: 2021.05.07 13:45:33 +02'00'

……

Josef Pihera

……

Luboš Polančík

V Plzni dne

prof. Ing. Zdeněk Peroutka, Ph.D.

Digitálně podepsal prof. Ing. Zdeněk Peroutka, Ph.D.
Datum: 2021.05.07 19:51:40 +02'00'

……

prof. Ing. Zdeněk Peroutka, Ph.D.

děkan Fakulty elektrotechnické
Západočeské univerzity v Plzni

Abstract

This diploma thesis focuses on Outer Corona Protection in electrical rotating machines. This thesis overview of partial discharges is given, along with an overview of how to protect the machines against them. Furthermore, some experiments are described, which are about square resistance and other properties of OCP. Lastly, measurements on OCP materials are performed and described.

Keywords

Outer Corona Protection, Semi-conductive Slot Coating, Partial Discharges, Corona Discharges, Slot Discharges, Surface Discharges, Square Resistance, Measurements

Declaration

I, Bc. Luboš Polančík declare that I have written this diploma thesis independently under the supervision of the supervisor and that I have listed all sources used to write this thesis.

Signature

In Pilsen 20.5.2021 Bc. Luboš Polančík

Acknowledgement

Firstly, I would like to thank my family for their incredible support, without which I would have never gotten this far in my studies. Great gratitude also belongs to my supervisor, Ing. Josef Pihera, Ph.D., who made this thesis possible and always provided valuable advice whenever I needed it. I would also want to thank my colleague and classmate, Bc. Pavel Rous, who significantly contributed with his expertise.

Content

Introduction

Synchronous machines have a broad range of possible applications and designs, especially after synchronous machines' arrival using permanent magnets. In the past, apart from being used as generators of electrical power, they were used as compensators of power factor. However, their most significant contribution still lies in the production of electricity for the electricity distribution system. High power alternators can be divided into two basic types: hydro alternators used primarily in hydropower plants powered by water, second turbo-alternators driven by steam turbines. Asynchronous machines can be used as generators, but they are rarely used for this purpose for various reasons. Turboalternators mainly operate as two-pole machines. As a two-pole, their rotating speed is 3000 rpm in networks operating at 50Hz. Value 3000 rpm can be calculated using equation (1). [22] [23]

$$n_s = \frac{60\,f}{p}\ [rpm] \tag{1}$$

Due to their massive power output, they have to be very massive. Due to their relatively high rotating speed and the resulting centrifugal forces, the diameter cannot be “very wide”. Turboalternators tend to have an inner diameter of one meter, but they are very long, sometimes even tenfold longer than wide. [23][24]

The rotating synchronous machines can generate over 200MW of power, which makes them very structurally tricky and expensive. Because of that, the protection of the machine is essential and also challenging. High voltages generated by this machine puts pressure on the development of insulating materials. The machine must remain operatable for many years without any significant failures. Therefore, the insulating materials must be well

designed in terms of thermal stability and mechanical stress. Of course, it must protect against the effects of high voltage and its electrical field. [1]

List of symbols and abbreviations

Ω……..Ohm – Unit of electrical resistance
R…….…….…….Resistance [Ω]
$R_{□}$…….……... Square Resistance [Ω/□]
ρ……..…….……...…Resistivity
V…….……Volt – Unit of electrical voltage
A…….……Amper – Unit of electrical current
U…….……Electrical Voltage [V]
I……..……..Electrical Current [A]
W…….……Unit of Power
C…….……Capacitance [F]
n…….……..Revolutions [rpm]
p…….……..Pole pairs
f…….…...Frequency [Hz]
DC…….……...Direct Current
AC……...Alternating Current
m……..Meter – Unit of distance
E……...Electrical field [V/m]
J……Current density [A/m^2]
°C…….Degree of Celsius – Unit of temperature
s……Second – Unit of time
min……...Minute – Unit of time

1 Discharge activity in rotating machines

There are several types of stresses influencing a rotating machine's insulation system during its lifetime. This fact leads to perceptible changes in the properties of the used materials. The insulation is under mechanical stress, electrical and thermal stress. All these influences gradually shorten the service life of the insulation. In generators, where a single-phase voltage is above 6kV, discharge activity occurs, which does not lead to the direct destruction of insulation but causes several processes that contribute to the possible failure of the whole insulation system. [2] [20]

1.1 Corona

Corona discharge is a single discharge that can occur in high voltage applications. If the intensity of the electric field between the electrodes increases enough, it eventually ignites corona discharge. Corona discharge manifests by the typical colouration of the electrode area. The discharge can be seen with the eye, but only to a limited extent. Some of the light emitted by the discharge is in a visible spectrum, but it extends into the ultraviolet spectrum. The principle of corona discharge formation depends on the attached polarity, which significantly complicates discharge problems in alternating voltage. This phenomenon is also observable even under atmospheric conditions on power lines, building, and ship's masts. Sailors used to refer to this phenomenon as St. Elmo's fire. In this case, the corona discharge is incomplete. The discharge doesn't interfere from one electrode to the other, and it creates tufted discharge only around one electrode due to the unevenness of the electric field strength in the area. As mentioned before, the formation of corona discharge depends on the polarity. The mechanism of forming the discharge is different in each case. However, ignition occurs at approximately the same voltage. In the case of the negative voltage on the electrode, positive ions are attracted to the cathode, and free electrons are released. These

free charge carriers move through space at a speed that depends on the applied voltage. If the voltage is sufficient, the carriers gain enough kinetic energy to excite electrons of neutral molecules and atoms in the environment. The transition back from the excited state to the original energy level causes energy release in the form of photons. It is this deexcitation that causes the typical glow of the corona discharge. In the area around the curved electrode, where the electric field intensity is the strongest, electrons can be accelerated to cause a neutral atom's ionisation, completely releasing particles from valence bands and forms two separate particles, a free electron and a positive ion. Deexcitation and subsequent emission of photons also occur in the recombination of the positive ion and negative electron. As the ionisation of the dielectric increases due to an external electric field's influence, a space between the electrodes is created, which creates its own electric field. This area has a predominance of positive ions towards the cathode and a predominance of negatively charged electrons towards the anode. As with the dielectric polarisation, the inner field has the opposite direction to the external one. This fact causes the resulting electric field, given by the sum of these two fields, to have lower intensity. With a decrease in the electric field's intensity, electrons' speed also decreases, preventing further ionisation and excitation. The electron then only drift towards the anode. For this reason, are the corona discharges referred to as incomplete discharge. When applying a positive polarity to a curved electrode, the ignition principle is different, mainly the mechanism of ionisation. An avalanche of electrons is formed at the corona discharge's outer boundary, and electrons move towards the anode. The ionisation process is based on the intake of energy from photons. It is, therefore, so-called photoionization. [1]

An almost constant electric field intensity is kept on the electrode's surface during the corona discharge formation, which helps with ionisation. With the voltage increase, spatial charge also increases, which has the same polarity as the electrode. The resulting space

charge is replenished supplied by the ionisation layer and moves away from the electrode, forming the corona discharge. This movement of space charge causes losses and is referred as corona current. The formation of space charge can be seen in Figure 1. [1]

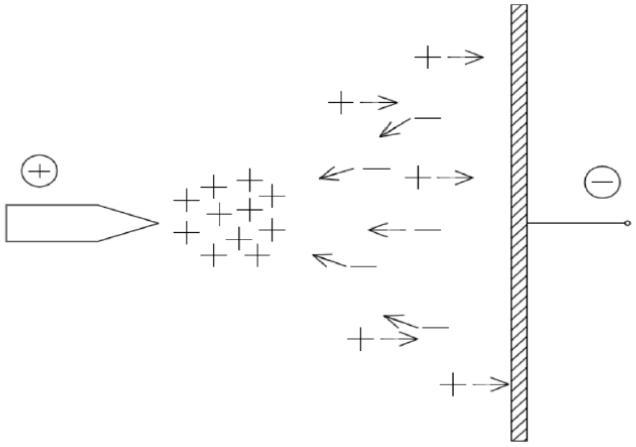

Figure 1 Spatial charge around a curved anode, taken from [19]

1.2 Surface discharges

Surface discharges are, like corona discharges, an incomplete discharge. However, their characteristic feature is that surface discharges move on the electrode's surface (on the insulation). The main difference is that they do not close through the air, but they close between the insulation's surface and the machine's core. The discharge movement is caused by inhomogeneity of electric field, which can arise in some electrical systems and machines, such as stator bars protruding slot of an electrical rotating machine. In the exit area from the slot–enwinding area, a sharp transition occurs in terms of electric field intensity. The curvature of such an electric field is a suitable environment for the formation of surface discharges. Lines of force tend to bend towards the grounded magnetic circuit. Due to the curvature of the lines of force, a tangential component is present, which causes the discharge to move along the insulation's surface. Surface discharges can be significantly longer than

corona discharges. If the voltage increases even further after the corona state, it can cause thermal ionisation. In this case, change from corona strands into characteristic luminous tufts occurs. Surface discharges can spread on the surface very easily because the discharge channels have very low resistance. Thus, at the end of the channel, the voltage is still very high. Due to sudden ionisation, the discharge can move very fast, and due to very low resistance, the arc can be pulled into considerable distances. [1] Visualisation of the electric field at the end of a slot can be seen in Figure 2.

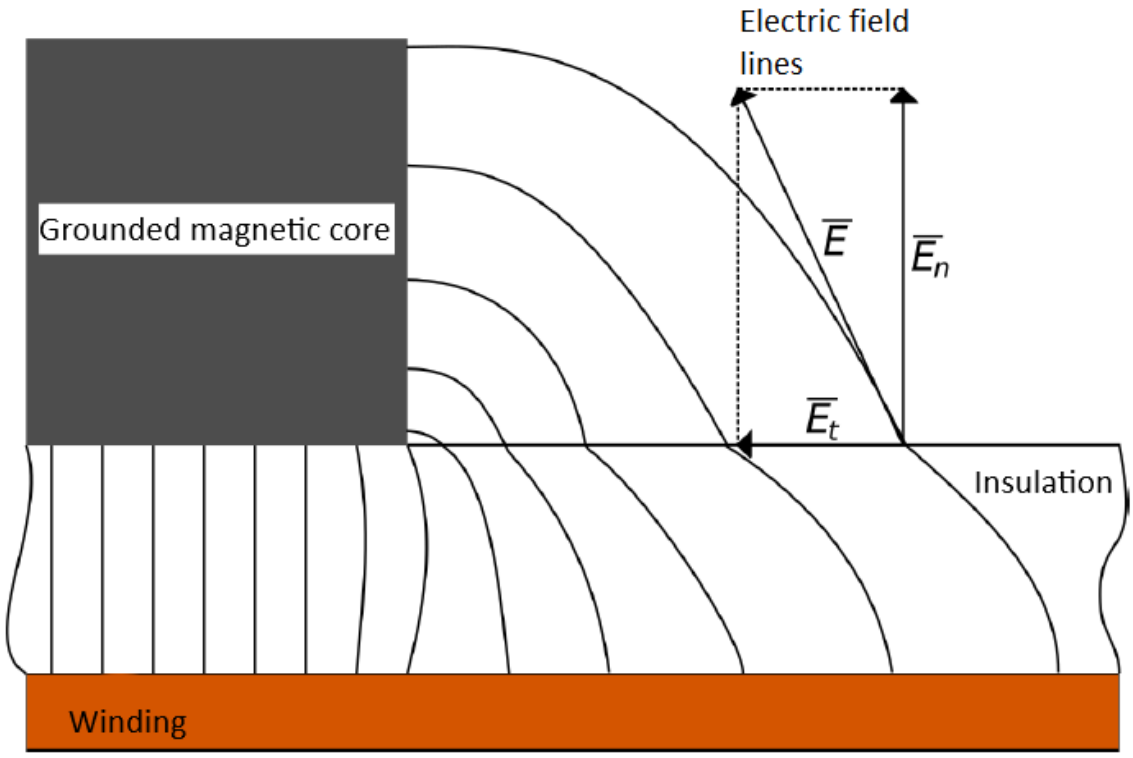

Figure 2 Distribution of the electric field near the end of the slot, taken a modified from [1]

1.3 Slot discharges

In the insulation of form-wound stator bars of rotating electrical machines working under high voltage, small cavities filled with gas may occur due to the material's imperfections. They may also arise during the manufacturing process. They can also be formed by intense local stress of the electrical field. There are many different types of cavities, as seen in Figure 3. Electrodes are marked as 1 and 2, and the cavity itself is labelled

as 3. A solid insulator containing a cavity filled with gas can be seen in Figure 3a. A typical example of the cavity formed by insulator detaching from the electrode can be seen in Figure 3b. A typical case of delamination can be seen in Figures 3c and 3d. [3] [5]

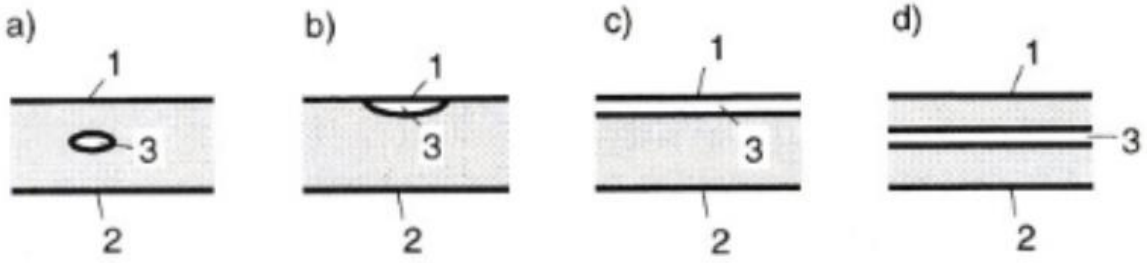

Figure 3 Different types of cavities, taken and modified from [3]

If the voltage on electrodes reaches a specific value (ignition voltage), a discharge will occur if a gas (in general air) filled void is present in this area. These discharges have avalanche or spark discharge character, so they are considered one type of partial discharges. If air (respectively oxygen) combined with discharge activity is present in the cavities, ozone is produced, which has strong corrosive effects. Chemical destruction of the insulator is also caused by chemical products of decay of some insulating materials during the discharge. Furthermore, a destructive effect is caused by the bombardment of the cavity walls by electrons and ions. Continuous stress described in this chapter alone leads to the eventual destruction of the insulation. [5] [31 pages 20 - 24]

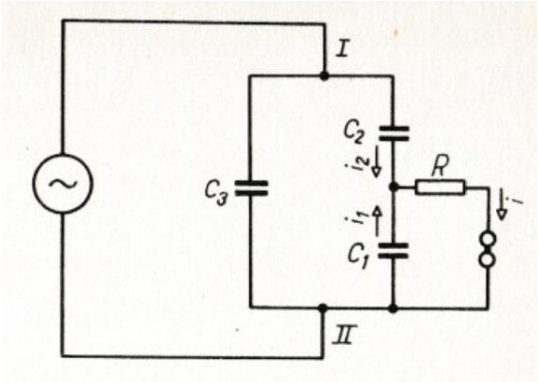

Figure 4 Substitute circuit for an object with a cavity in it, taken from [5]

The substitute circuit seen in Figure 4 is connected to AC voltage through electrode clips I and II. Assuming the voltage rises from zero value to full voltage U, at which the voltage on C_1 reaches the ignition voltage U_{1z}, the relation between U and U_{1z} can be seen in equation 2. [5]

$$U_{1z} = \frac{C_2}{C_1 + C_2} U \tag{2}$$

During the discharge, which appears when the voltage reaches value U_{1z}, voltage drops to quenching voltage. For purposes of simplicity, let's assume that the quenching voltage is zero volts. [5]

The circuit's inductance does not allow the voltage source to give an electrical charge during the discharge. Therefore, the voltage on clips I and II drops from original value U to U_v, which results from equality of charge of group C_1, C_2 and C_3 before and after the discharge.

$$\left(\frac{C_1 C_2}{C_1 + C_2} + C_3\right) U = (C_3 + C_2) U_v \tag{3}$$

Hence the following:

$$U_v = \frac{C_1 C_2 + C_1 C_3 + C_2 C_3}{(C_1 + C_2)(C_3 + C_2)} U \tag{4}$$

After substituting from equation 2:

$$U_v = \frac{C_1 C_2 + C_1 C_3 + C_2 C_3}{C_2 (C_3 + C_2)} U_{1z} \tag{5}$$

The discharge will therefore cause a voltage drop at electrode clips I and II

$$\Delta U = U - U_v = \frac{C_2}{C_3 + C_2} U_{1z} \tag{6}$$

1.4 Influence of partial discharges

Partial discharges cause chemical, thermal and physical changes in the insulator's inhomogeneities (voids), which are irreversible. These processes can lead to a critical failure of the long-term stressed material before its end of service life. This degeneration of electrical insulating materials by partial discharges occurs mainly due to two processes. Chemical degeneration of the dielectric and bombardment of the cavity walls by charged particles (e.g. ions) in the insulation. [2] [21] [29]

1.4.1 Chemical, electro-erosive and thermal stresses

When discharge appears, ozone is formed from oxygen atoms in cavities, which has strong oxidising effects. In extreme cases, when nitrogen oxides are present, ozone can form even more aggressive nitric acid. Even products of self- decomposition of the insulation material by partial discharges can cause chemical destruction. Products of these chemical reactions can further diffuse into the solid insulator and create conductive paths inside the insulation. [3]

If an arc develops in the cavity, it is likely to form a conductive path. At high electric field intensity values, the electric field may cause a pure electric breakdown. The conductive path can gradually propagate through the insulator and impair the insulation properties of the material. Ions and electrons can also cause the destructive effect by bombarding the cavity walls, causing them to erode. Gradual enlargement of the cavity can lead to a total

breakthrough of the insulator. Partial discharges also produce heat, and repetitive occurrences can lead to thermal instability of the material. [3]

1.5 Vibration sparking

Along widely acknowledged partial discharges, less known and studied vibration sparking can occur, which is significantly more dangerous. Vibration sparking can occur at any position within the winding. Another danger of the vibration sparking lies in the fact that it can deteriorate the stator insulation at any voltage level, unlike the partial discharges, which need the voltage to reach the ignition value. [6]

Vibration sparking (VS) occurs due to the bars' movement within the stator slots and if the outer corona layer's resistance is too low. VS appeared first in the sixties, thanks to the introduction of modern epoxy-bonded mica tapes. Before that, asphalt-bonded mica tapes were used. These tapes swelled within the slots during operation. The new type of mica tapes behaved very differently in terms of thermal expansion so that they were almost stable and did not expand much. Without the thermal expansion, the self-tightening effect was missing and allowing looseness of the slots' bars and their movement inside the slots during operation. It is practically impossible to manufacture stator bars to fit perfectly into the slots across their entire length; hence small voids appear. Thermal processes also contribute to creating such voids, as seen in Figure 5. [6]

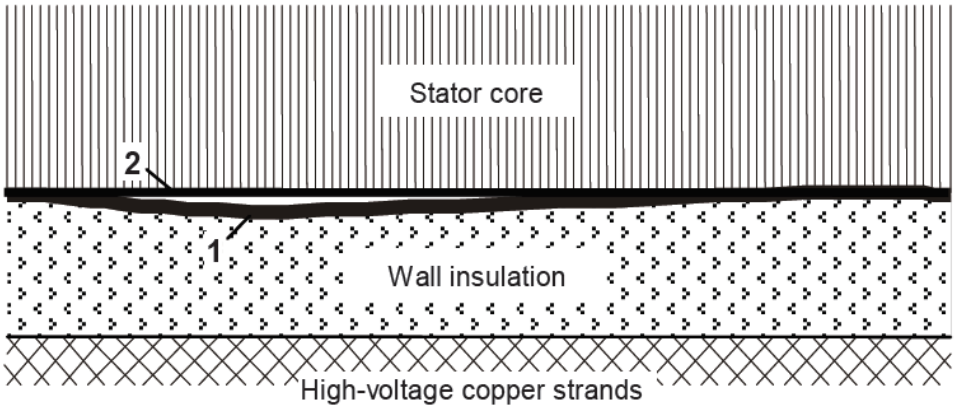

Figure 5 Void between stator bars and stator slot walls, taken from [6]
1: Outer corona layer, 2: Conductive fleece for slot lining

For plain bar surfaces, where the potential difference between bar surface and slot wall exceeds the breakdown strength of air, the partial discharge would occur. To suppress this phenomenon, the standard protection against it today is to apply a slightly conductive coating to the bar's surface. This semi-conductive layer adapts to the earth potential thanks to lateral corona earthing points. However, the potential will be slightly different due to equalisation currents and voltage drops between every earthing point. [6]

In papers [7] [8] [9], along with some assumptions, calculations were made to determine optimal square resistance $R_{\square}$. Square resistance $R_{\square}$ is the resistance between two opposite sides of a square. The paper [6] conclude that the optimal $R_{\square}$ for generators operating at voltage V_N =11 kV is 25kΩ per square. However, there are various factors regarding the resistance of an OCP which must be considered in the insulation design. [6] According to [32], electrical rotating machines, rated 6 kV or more, should have semiconductive coatings with square resistance ranging from 0,3 to 10 kΩ per square in the slot to prevent surface discharges. The IEEE standard [33] says the fully cured semiconductive coating should have square resistance in a range of 0,1 – 500 kΩ per square, which gives a much bigger range of possible values for optimal square resistance. Thus, determining the exact ideal value of R□

is not an easy process, and deep analysis is needed for each individual application of semiconductive slot coating. [6] [7] [8] [9] [32] [33]

2 Protection against partial discharges

In every generator, the stator coil consists of a copper conductor, on which the insulation is wound. This insulation is further provided with a corona protection layer. There are two main types of corona protections. The outer corona protection (OCP) in the slot part of the winding and the end corona protection (ECP) on the exit of windings out of the magnetic circuit respectively stator core. [2] [32]

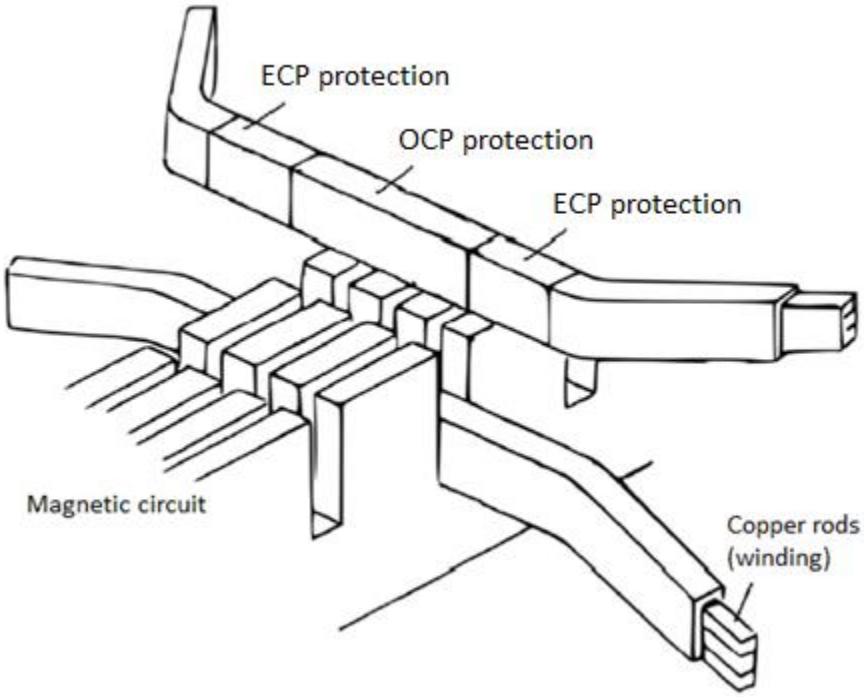

Figure 6 Arrangement of corona protections, taken and modified from [2]

The OCP protection layer must provide a steady electrical connection of the laminated stator core's ground potential to the insulation. The protection must be conductive enough to achieve this, but it cannot be conductive too much; otherwise, it could cause eddy currents in the laminated stator core. It might also cause vibration sparking if the bar or coil is loose in the slot. It is also essential to have evenly distributed resistivity in this layer. Significant

derivations from an even resistivity distribution can lead to a local increase of temperature and even discharges. [6] [10] [18]

To characterise materials, it is common to use square resistance $R_{\square}$ as its core property. Square resistance is derived from surface resistance and is calculated using equation (7), where R stands for measured resistance, w is the width of electrodes used to measure resistance, and l is the length between the electrodes. [10].

$$R_{\square} = R \cdot \frac{w}{l} \ [\Omega] \tag{7}$$

Paper [10] claims*: "This approach might be sufficient for a quick assessment of the local OCP tape surface resistance. However, a more complex view is required to approximate the electrical behaviour of an OCP system."* Because every corona protection is composed of three materials, conductive particles, carrier material, and a binder resin, all of which influence the protection's final properties. They claim that for a more precise description of the material, electrical resistivity must be known in all three directions of space as seen in equation (8), where A is the area in which current flows, l is the length of the measured part and indexes L, C, T stand for the direction in which the measurement is done (L = lengthwise direction, C = cross direction, T = transitional direction). [10] For better understanding, look at Figure 7.

$$\rho_{L,C,T} = R_{L,C,T} \cdot \frac{A}{l} \tag{8}$$

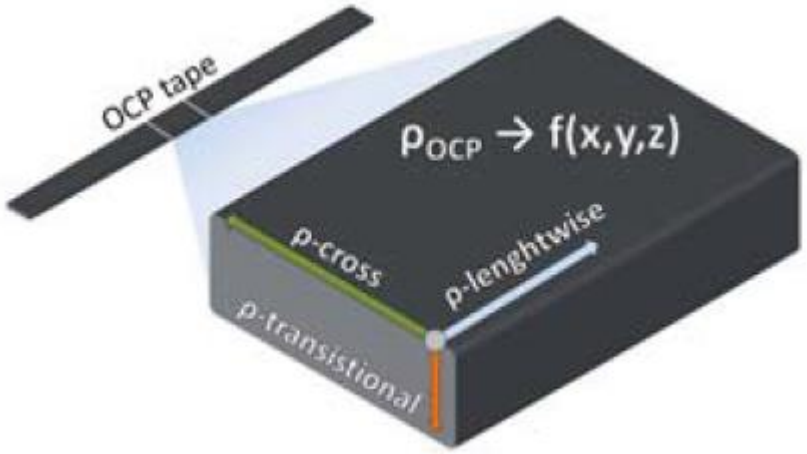

Figure 7 Schematic description of directional resistivities, taken from [11]

At large turbine generators, which use GVPI (Global Vacuum Pressure Impregnation) technology, the insulation undergoes significant thermodynamic stresses even under the manufacturing process. To handle these thermal stresses, corona protection is made using the so-called Double OCP System method. This method uses two layers of OCP tape layers, which are separated by mica material to ensure that a slight movement between the outer and inner OCP layer is possible without the danger of damaging the electrically exposed interface of the OCP layer and the main insulation. Both OCP layers must be electrically connected, and to achieve that, the conductive tape is interwoven in the bar's lengthwise direction. [10] [11] Double OCP system layout can be seen in Figure 8. More about Double OCP system is written in Chapter 2.1.

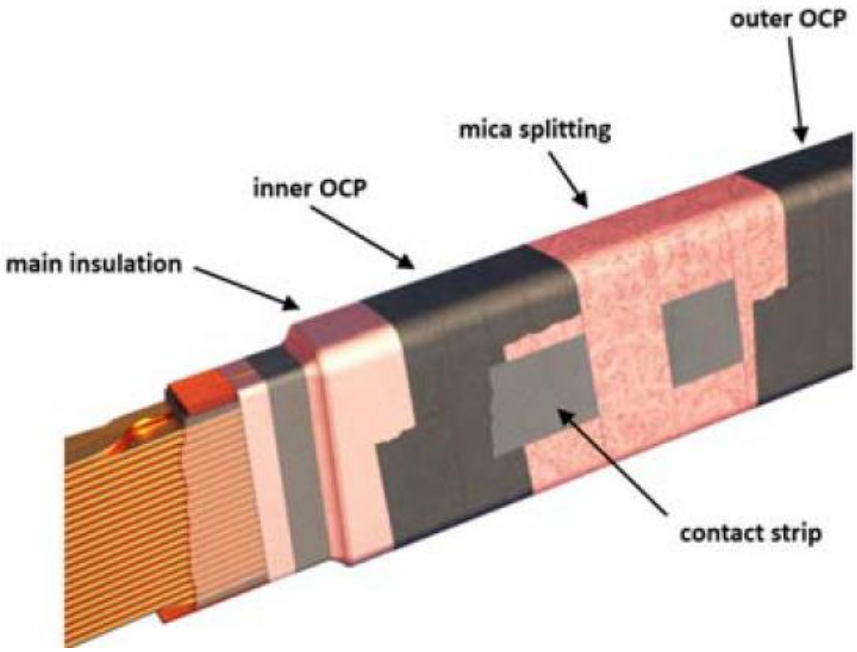

Figure 8 Composition of layers in Double OCP System, taken from [11]

2.1 Corona protection differences between different construction variabilities

Electrical rotating machines have rated power up to 2000MVA operating at nominal voltages reaching up to 27 kV. Machines with this kind of power reach enormous proportions. The size of insulation of such machines demands a different manufacturing approach in contrast with smaller machines with rated power, for example, 500 MVA. [16]

The largest types of machines are characterised by the process of stator completion. So-called Single bar Vacuum Pressure Impregnation (SVPI) approach is needed. Firstly, every single stator bar must go through an impregnation and curing cycle to build up the mica insulation volume. After this process, the surface is mechanically smoothened, and OCP varnish is painted on it to function as the electrical field grading element. This painted layer is additionally laminated with some form of conductive mechanical protection in the form of conductive tapes or wallpapers. This conductive mechanical protection must form a single OCP layer along with the OCP varnish underneath it from the electrical point of view. When the stator bars are impregnated, cured and painted, they are inserted into the stator core slots;

they have to be furthermore equipped with side filler straps in the form of conductive wavelike ripple springs, which help the bars to be fixed tangentially in place. This functions as active protection against excessive movement of the bars in slots due to electro-magnetic forces. These filler straps also help with providing electrical contact of OCP broadside surfaces and the laminated grounded core. To fix the bars radially, ripple spring straps are placed under the slot wedges. [16] [17]

In contrast to manufacturing very large machines with SVPI, medium machines up to 6m in length and 500 MVA of rated power are assembled by applying the Global Vacuum Pressure Impregnation (GVPI) method. With this method, the stator bar insulation system is built up by wrapping the bars with ICP, mica insulation, OCP, and ECP. Stator bars with this dry insulation system is then inserted into stator bar slots. After wedging the slots, connecting end winding and blocking the end winding baskets, the whole stator is impregnated with epoxy resin. The final curing process bonds the OCP tape with the surface of stator core slots. GVPI process introduces strong thermal and mechanical stresses to the insulation. To endure such stresses, the OCP system is realised as a Double OCP layer structure. The inner layer of the OCP bonds to the main mica insulation, and the outer layer bonds to the slot surface. These two layers are separated by the mica splitting layer, which helps with enduring mechanical tension forces caused by thermal expansions. To ensure contact of inner and outer OCP layers, OCP tape is used. The connecting OCP layer is alternatively woven with the mica layer, as seen in Figure 9. In this Figure, the inner layer is not visible because it is hidden behind the splitting materials. [16]

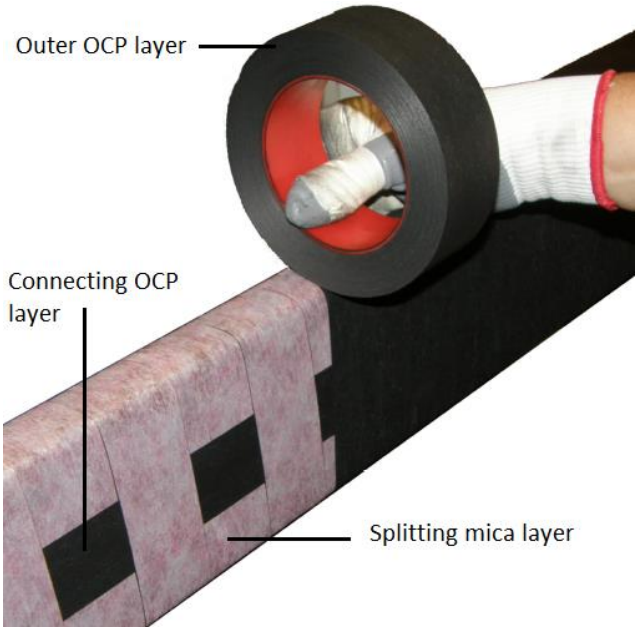

Figure 9 Illustration of double OCP layer system, along with splitting materials, taken and modified from [16]

2.2 One of the possible ways to determine optimal square resistance

As mentioned before, there is no universal square resistivity for OCP materials that could be used on each electrical rotating machine. The authors of the paper [16] performed several simulations using the Finite Element Method (FEM) for GVPI and SVPI stator bars with different OCP square resistance values to better understand OCP systems of large electrical rotating machines. The FEM has proved its practicability in the field of simulations and calculations of the sub-element end corona protection (ECP) in the rotating machine main insulation system. [30] Because OCP systems on large electrical rotating machines are enormous, where its lengths can reach more than 7 meters, it is obvious that a simulation of the complete system is impossible due to the time needed to do the simulation calculations. Also, modelling of the whole system is not applicable because of the aspired high resolution of the thin layers. Therefore, an analysis of the structure was needed to find out how to simplify the model into a suitable representative model. *"This dimensional reduction of the calculated model is feasible if the overall OCP system conclusions are extractable out of this representative model."* [16] In Figure 10, a model of the SVPI stator bar with visually

separated elements can be seen, which was used for simulation. In Figure 11 and Figure 12, results of a simulation of the distribution of electrical potential on the OCP layer and ripple spring on SVPI stator bars can be seen. Figure 11 shows low resistance OCP protection results, and Figure 12 shows how the potential is distributed when high resistance OCP is applied. Relative scaling represented by colours was chosen. The difference between the lowest and highest potential value is different for each result. [16]

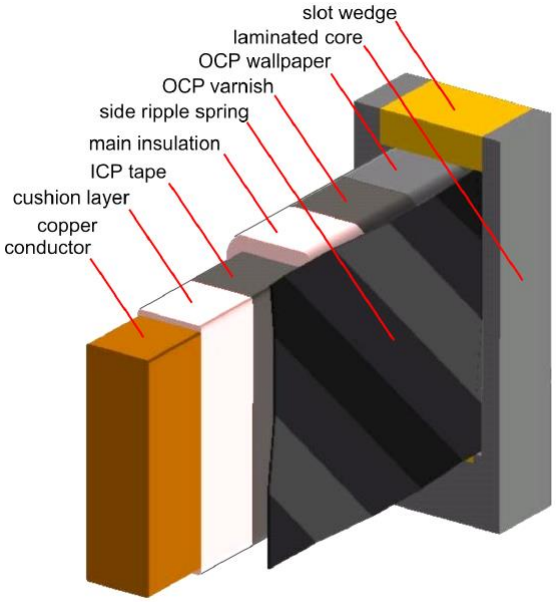

Figure 10 Model of SVPI stator bar section used for FEM simulation with visually separated elements, taken from [16]

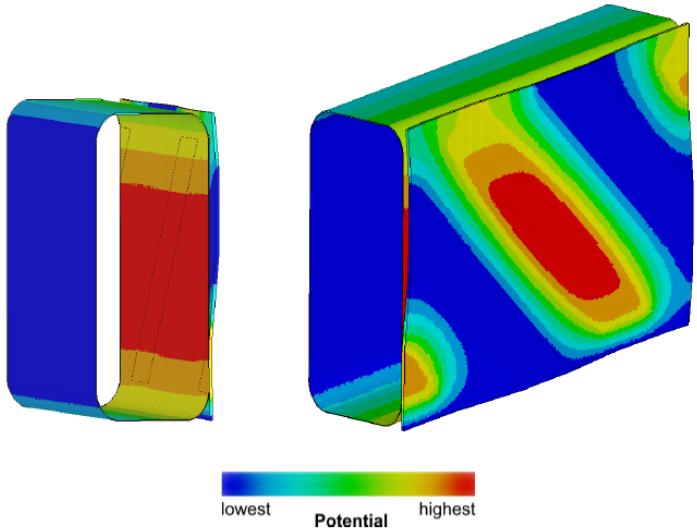

Figure 11 Distribution of electrical potential on OCP layer and ripple spring of SVPI stator bar with low square resistance, taken from [16]

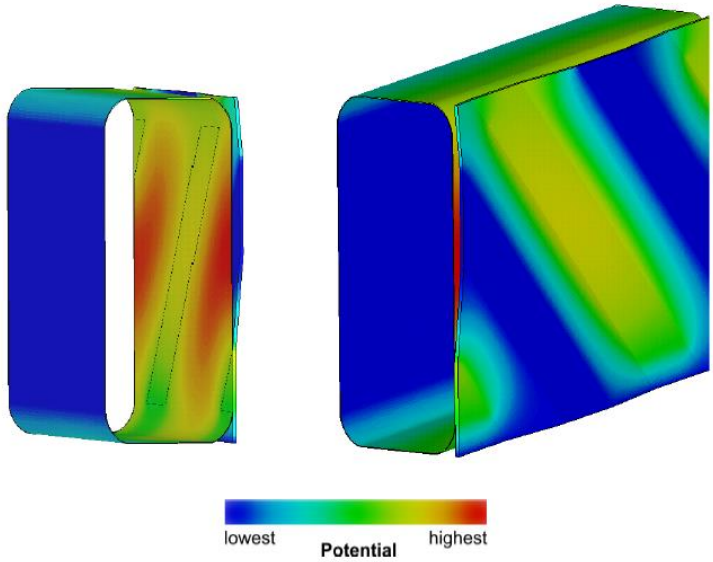

Figure 12 Distribution of electrical potential on OCP layer and ripple spring of SVPI stator bar with high square resistance, taken from [16]

Paper [16] concluded that the FEM method has proven as a sufficient tool for modelling and simulating complex structures such as OCP protections and that this example shows a possible way to accelerate OCP development or to be able to deeply analyse degradation effects by facile varying resistance values as input parameters of the FEM models. [16]

3 Current manufacturers of OCP and ECP protections

Several companies on the market manufactures ECP and OCP products with a variety of properties. This chapter provides a brief overview of manufacturers and their products. The chapter is also supplemented by an overall comparison of their available products. [2]

3.1 Company Von Roll Holding AG

One of the leaders in the corona shielding market is a Swiss company called Von Roll Holding AG. This company has a broad portfolio. They produce insulation materials, components for industrial applications, thermal and fire-resistant insulation and of course, they manufacture products for protecting against partial discharges. They divide these products into three basic types:

- ICP - internal corona protection
- OCP – external corona protection
- ECP – end corona protection

The first ICP product line is used as protection against partial discharges that can occur inside cavities, which formed after Roebel transposition. [2]

The purpose of the OCP product line is to suppress partial discharge between the main insulating layer of the Roebel rod and the rotating machine's magnetic circuit. The application of OCP protection results in equalising the potential along the whole coil with the magnetic circuit's potential. [2][25]

The company manufactures two different varnishes for the ECP product line, the P 8001 and the P 8002, made from modified phenolic resin with a SiC particles as a filler. The tapes for these products are made from woven polyester fabric impregnated with resin with SiC

filler particles. These materials are usable up to temperature class F (155 °C). The tapes are called CoronaShield® 217.XX, where XX indicates the specific type of tape. [2]

The manufacturer divides tapes into three types, which can be described by their dependence on the electric field gradient, as shown in Figure 13.

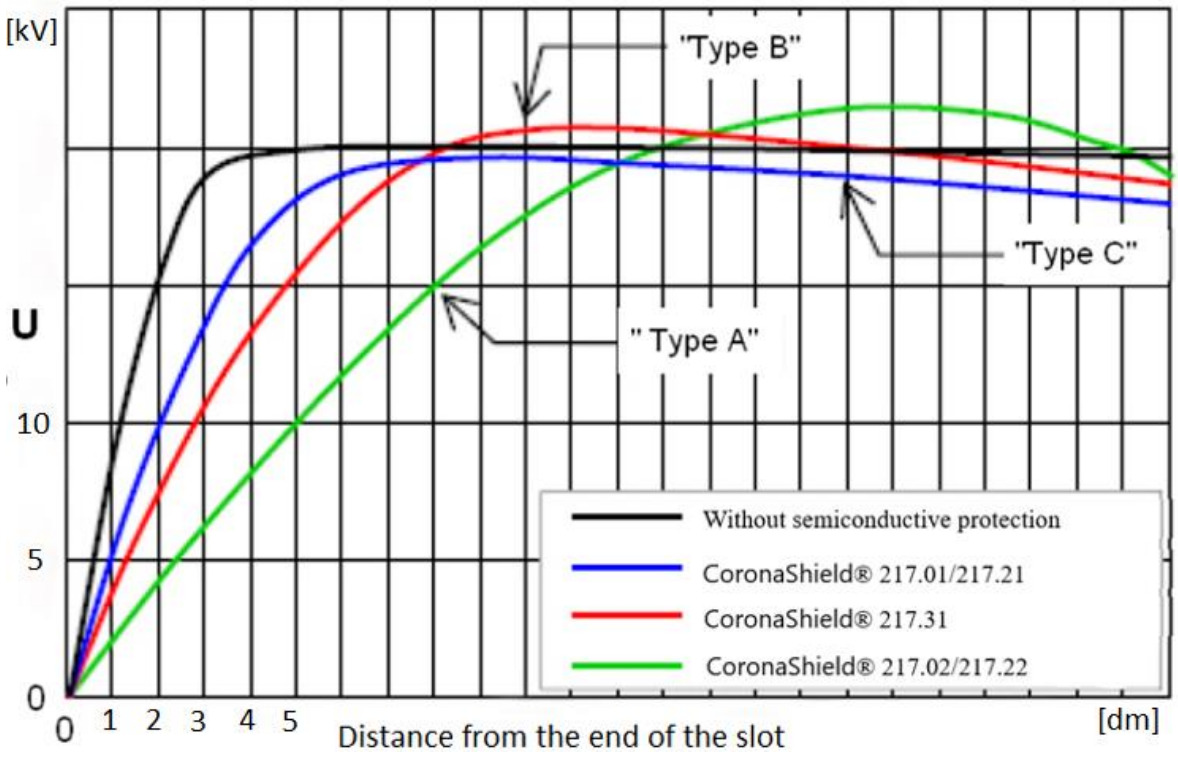

Figure 13 Different dependences of protection types on electric field gradient, taken and modified from [4] [34]

The number 0 in the product's name, displayed after the dot, indicates them on both sides of the tape (for example, CoronaShield® 217.01). On the other side, number 2 represents its absence (for example, CoronaShield® 217.21). [2]

Von Roll Holding AG recommends applying all ECP protections with a 2 cm overlap over the OCP protection. Their ideal length can be determined using equation (9), where l represents the ideal length, and U_z represents testing voltage.

$$l = \frac{U_Z}{2} \tag{9}$$

3.2 Krempel GmbH

Another significant manufacturer is a company from Germany called KrempelGmbH. In addition to OCP and ECP protections, they also produce insulating materials and special laminates. Their only product in the ECP protection field is ECP tape AKASIC 4b. The protection is self-shrinking in the longitudinal direction. This procedure ensures good contact with insulation, and it also does not form cavities under ECP protection. [2]

3.3 Isovolta AG

Company Isovolta AG from Austria produces only OCP and ECP anti-corona protections and does not manufacture any varnishes. They make two different types of ECP tapes, first is EGSB® 2969 for use with Resin Rich technology and the second is called EGSB® 2709 for use with VPI technology. [2]

3.4 Comparison of selected manufacturers

There are more manufacturers in this field. They are all compared in Table 1 and Table 2. In the tables, you can find manufacturers already mentioned, and some new ones are compared.

Table 1 Comparison of parameters of OCP tapes, taken from [4]

Manufacturer	Tape marking	Thickness [mm]	Extension [%]	Tensile strength [N/cm]	Surface resistivity [Ω/□]
VonRoll	CoronaShield® C 215.51	0,1 ± 0,02	≥ 10	≥ 30	200 - 400
	CoronaShield® C 215.51-03	0,1 ± 0,02	≥ 10	≥ 30	400 - 1000
	CoronaShield® C 215.55	0,085 ± 0,02	≥ 8	≥ 30	200 - 400
	CoronaShield® C 215.63	0,17 ± 0,03	≥ 5	≥ 12	200 - 400
	CoronaShield 250 N 85	0,085 ± 0,01	-	21±4	100 - 400
	CoronaShield 2500	0,125 ± 0,015	-	38±5	100 - 400
	CoronaShield® 2500 NB 70	0,07 ± 0,01	≥ 5	≥ 35	1500 - 3000
Chhaperia	C1530-1	0,08 ± 0,03	≥ 8	≥ 25	500 - 1800
	C1530-1A	0,09 ± 0,02	≥ 8	≥ 30	200 - 800
	C1530-1B	0,09 ± 0,03	≥ 15	≥ 60	1000 - 5000
Vidyut	VID-ANTICOR 3.85	0,085 ± 0,002	8	> 30	40 - 400
	VID-ANTICOR 5.110	0,115 ± 0,015	15	> 50	200 - 1000
Krempel	06 EWR 15 AA	0,18 ± 0,036	≥ 8	≥ 20	400 - 6000
	07 EWR 05 AA	0,13 ± 0,026	≥ 9	≥ 28	400 - 5000
	10 EWR 02 AA	0,2 ± 0,04	≥ 10	≥ 12	400 - 20000
	12 EWR 01 AA	0,29 ± 0,058	≥ 4	≥ 12	400 - 6000
	03 ELR 19 AA	0,05 ± 0,01	≥ 10	≥ 12	400 - 1000
	06 ELR 14 AA	0,1 ± 0,02	≥ 15	≥ 40	1000
	06 ELR 14 CB	0,12 ± 0,024	≥ 12	≥ 60	1200
	06 ELR 14 CC	0,1 ± 0,02	≥ 15	≥ 40	150 - 1500
	03 EFR 13 AA	0,08 ± 0,016	≥ 12	≥ 30	1000 - 2000
	03 EFR 13 BA	0,08 ± 0,016	≥ 12	≥ 30	400
	07 EFR 18 AA	0,14 ± 0,028	≥ 10	≥ 60	400 - 5000
	07 EFR 18 BA	0,14 ± 0,028	≥ 14	≥ 60	400 - 5000
	04 ESR 22 AA	0,22 ± 0,044	≥ 14	≥ 20	400 - 1000
	04 ESR 22 AA-sk	0,24 ± 0,048	≥ 14	≥ 20	400 - 1000
Isovolta	CONTAFEL® 2716	0,11 ± 0,02	-	≥ 40	200 - 600
	CONTAFEL® ME 3107	0,11 ± 0,02	-	≥ 40	200 - 600
	CONTAVAL® 2017	0,3 ± 0,15	-	-	500 - 50000
	CONTAFEL® 3080	0,08 ± 0.02	-	≥ 40	500 - 1500
	CONTAFEL® H 0865	0,12 ± 0.02	-	≥ 40	150 - 250
	CONTAFELPREG® 2564	0,18 ± 0,03	-	≥ 25	10000
	CONTAGLAS® 2912	0,07 ± 0,02	-	≥ 120	500 - 1500
Consulation Supplies	3.85	0,085 ± 0,02	8	> 30	200 - 400
	5.11	0,12 ± 0,02	15	> 50	50 - 250

Table 2 Comparison of parameters of ECP tapes taken from [4]

Manufacturer	Tape marking	Thickness [mm]	Extension [%]	Tensile strength [N/cm]	Surface resistivity [Ω/□]
VonRoll	CoronaShield® SC 217.01	0,22 ± 0,03	≥ 12	≥ 80	-
	CoronaShield® SC 217.02	0,22 ± 0,03	≥ 12	≥ 80	-
	CoronaShield® SC 217.31	0,25 ± 0,05	≥ 10	≥ 80	-
Chhaperia	C1530-2	0,2 ± 0,04	≥ 10	≥ 60	$5 \cdot 10^{4}$-$5 \cdot 10^{6}$
	C1530-2A	0,2 ± 0,04	≥ 10	≥ 60	$5 \cdot 10^{7}$-$5 \cdot 10^{9}$
	C1530-2B	0,2 ± 0,05	≥ 15	≥ 60	10^{10} - 10^{12}
Vidyut	VIDSTRESS 8.300	0,2 ± 0,05	≥ 8	≥ 60	-
	VIDSTRESS 10.350	0,25 ± 0,05	≥ 8	≥ 60	-
Krempel	AKASIC 4b	0,2 ± 0,02	≥ 20	≥ 50	-
Isovolta	EGSB® 2709	0,24 ± 0,04	≥ 10	≥ 80	$\geq 10^{11}$
	EGSB® 2969	0,15 ± 0,03	≥ 20	≥ 40	$\geq 10^{11}$
Consulation Supplies	8.3	0,2 ± 0,03	≥ 8	>100	-
	5.125	0,13 ± 0,02	≥ 8	>100	-

4 Diagnostics methods for the OCP properties

4.1 Measurement of surface and volume resistivity

The standard that deals with measuring surface and volume resistivity of solid electrical insulating materials is IEC 62631-3-1:2016. This standard gives as an example three most used methods – voltammetric method, Wheatstone bridge method and ammeter method, which are recommended for resistance measurement. The standard describes each of the listed methods in its own chapter. In practice, we can also encounter other methods, for example, the compensation method. [26]

In general, we can divide the methods into direct and comparative:

- Direct methods: they are based on simultaneous measurement of a DC voltage connected to an unknown resistor and the current flowing through the measured resistor [26]

- Comparison methods: they are based on determining the ratio of an unknown resistor to a known resistor in a bridge circuit or comparing currents flowing through known and unknown resistors at constant voltage [26]

4.1.1 Accuracy

The voltammetric method requires a voltmeter with an average accuracy; the sensitivity and accuracy of the method depend mainly on the characteristics of the instrument for measuring electrical current. [26]

The Wheatstone bridge method requires a sensitive current detector as a zero indicator, and the accuracy is determined mainly by the known resistors in the arms of the bridge. [26]

The accuracy of the ammeter method depends on the accuracy of the known resistor, stability and linearity of the current measuring instrument, and respective measuring devices. [26]

The accuracy of these methods is also affected by external factors such as parasitic currents caused by interfering external voltage. To reduce these effects as much as possible, different types of protection when measuring is used. For example, to eliminate the influence of external interfering voltages, shielded protective conductors in all critical parts of the

circuit can be used. Conductors like this capture parasitic currents of the environment, which would affect the results. [26]

4.1.2 Sources of voltage

For measuring the surface and volume resistivity of insulation, a very stable source is required. The current change caused by a voltage change must be negligible against the measured current. The standard specifies the testing voltages connected to specimen: 100, 250, 500, 1000, 2500, 5000, 10 000, 15 000 V. The most common values used are 100, 500, and 1000 V. In some cases, the resistance of the sample depends on the polarity of the connected voltage. In cases where this phenomenon occurs, this fact must be stated. For these cases, as a result, the geometric mean (arithmetic mean of the logarithmic exponents) of the two values is used. If the resistance of the specimen depends on the voltage, the test voltage must be stated. [26]

4.1.3 Electrode systems

The electrodes must have good contact with the sample surface. Their material must not affect the properties of the tested material. They must have a good conductivity and must be corrosion resistant. Furthermore, the material should allow easy and fast application, good contact with the tested specimen and should not introduce appreciable errors due to electrode resistance. [26]

Here is a short list of materials used as electrodes:

- Conductive silver varnish – These types of silver varnishes that dry in the air or are baked at low temperatures allow moisture to diffuse through them, allowing the tested specimen to be conditioned even after electro application. This is a welcomed feature when studying the effects of humidity and temperature on

resistance. Before using a conductive varnish as an electrode material, it should be determined whether the solvent in the varnish does not affect the electrical properties of the tested specimen. [26]

- Spray-coated metal – The sprayed metal can be used to achieve satisfactory adhesion to the tested specimen. Thin sprayed electrodes have certain advantages because they are ready to use immediately after the application. They are usually sufficiently porous so that the tested specimen can be conditioned. This fact must be checked before the conditioning. [26]

- Vapour deposited or sputtered metal – Vapor deposited or sputtered metal can be used under the same conditions as the spray-coated metal. It is necessary to determine that the tested specimen is not affected by ion bombardment or vacuum exposure. [26]

- Colloidal graphite – This type of electrode is used for hygroscopic materials in aqueous or other suspensions. [26]

- Conductive rubber – The conductive rubber should be soft enough to achieve effective contact with the tested specimen. Its advantage is that it can be easily and quickly applied or removed from the tested specimen. [26]

- Metal foil – Metal foil is suitable for measuring volume resistivity but not for measuring surface resistivity. Commonly used metals are lead, aluminium and tin. It is usually glued to the tested specimen with a minimum amount of adhesive in the form of vaseline, oil or other suitable material. The electrodes should be applied and smoothed with sufficient pressure to remove any wrinkles

and excess adhesive. This electrode system can be used successfully only on the specimen with a very smooth surface. The thickness of the adhesive should not exceed 2,5 μm. [26]

For measuring surface and volume resistivity, a three-electrode system is used, as seen in Figure 14. For plate and tubular materials, the electrode arrangement can be seen in Figure 15.

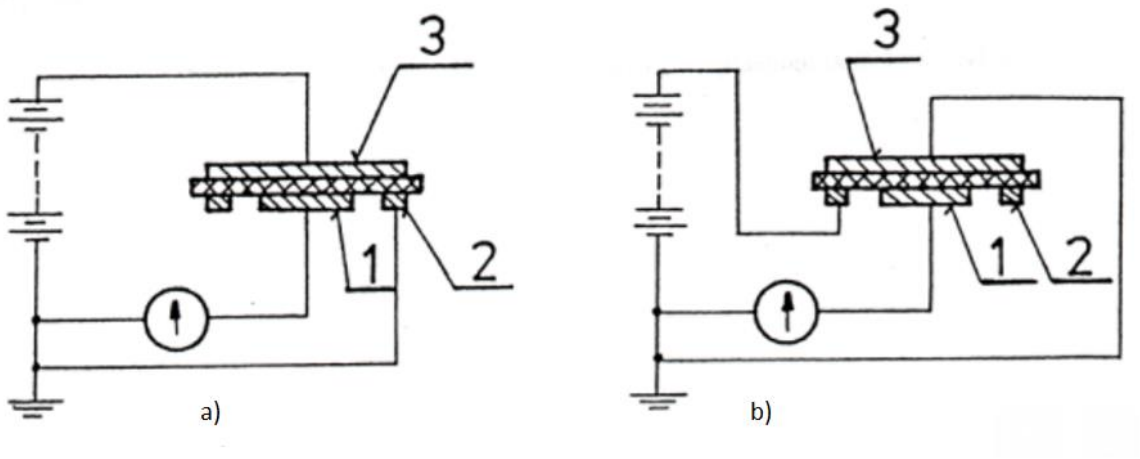

Figure 14 Basic three-electrode system used for measuring (a) volume and (b) surface resistivity

a) Volume resistivity

1 – measuring electrode

2 – grounded electrode

3 – voltage electrode

b) Surface resistivity

1 – measuring electrode

2 – voltage electrode

3 – grounded electrode

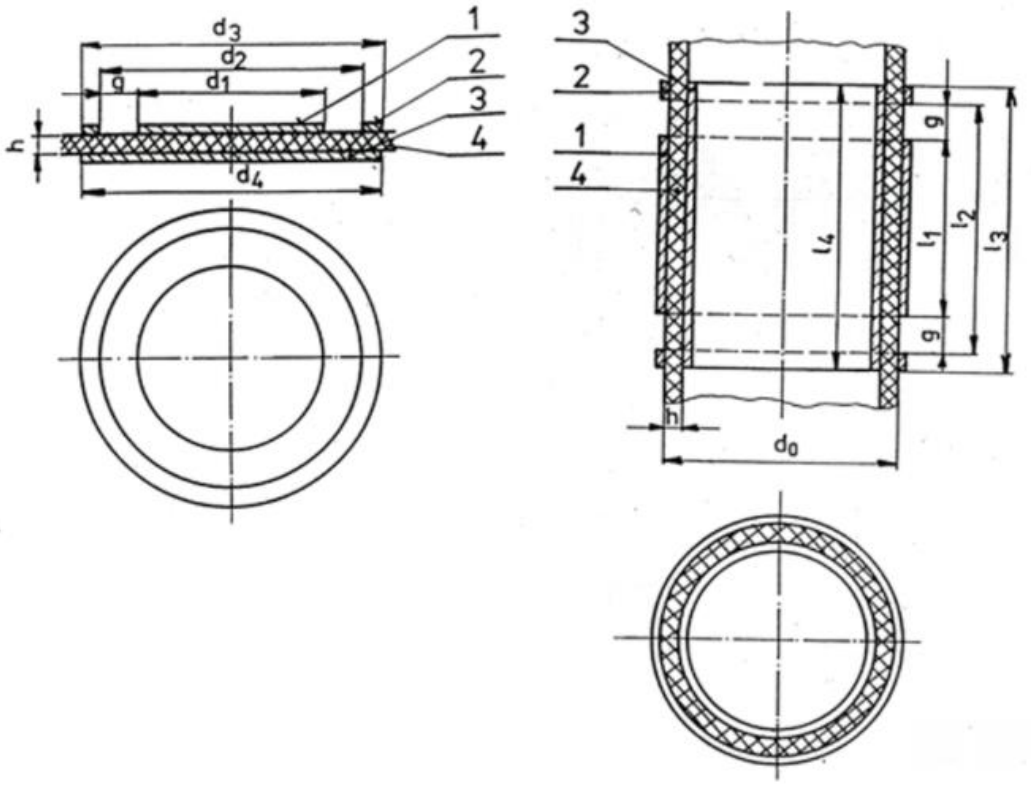

Figure 15 Electrode system for measuring the resistivity of tubular and plate materials, 1 – electrode number 1, 2 – electrode number 3, electrode number 3, 4 – measured material

Circular electrodes are most often used for plate materials. The diameter of the measuring electrode should be at least ten times the thickness of the tested specimen (in practice, at least 25mm). The diameter of the voltage electrode and the outer diameter of the grounding electrode should be at least equal to the inner diameter of the protective electrode increased by twice the thickness of the tested specimen. The diameter of the measuring electrode is selected from the series of 25, 50, 75 and 100mm. The gap between the measuring and protective electrodes should be minimal. When measuring the volume resistivity, it should be 1mm. When measuring surface resistivity, the gap should be equal to twice the thickness of the tested specimen, but at least 1mm. [26]

For tubular specimen, the length of the measuring electrode should be at least ten times the thickness of the sample (in practise at least 25mm); the same approach decides the length of the voltage electrode as for the plate materials. [26]

For liquid insulators, capacitors with a three-electrode arrangement are used to measure volume resistivity, which is then used to measure the loss factor. [26]

4.1.4 Tested specimen

Conditioning of the tested specimen

Conditioning means the adaptation of specimen to the environment and its influences such as humidity, temperature, pressure, etc. The conditioning to which the tested specimen is subjected depends on the material used to make the tested specimen and should be specified in the standard for individual materials. Recommended conditions are subject to IEC 212, and the relative humidity associated with various solutions are given in IEC 260. Volume and surface resistivity is particularly sensitive to temperature changes. The change in resistivity is exponential, so it is necessary to measure specimen under specified conditions. Long conditioning is required to determine the effects of moisture on volume resistivity because water absorption into the dielectric is a relatively slow process. Water absorption usually decreases internal resistivity. For some materials, it takes months to be fully conditioned. [26]

Manipulating with tested specimen

When handling specimen, parasitic currents between the electrodes mustn't significantly affect the measured results. It is very important that during the manipulation, the application

of electrodes does not create any leakage paths that will inevitably affect the measurement results. [26]

4.1.5 Test procedure

Volume resistivity

Before the measurement, the specimen must be brought to a dielectrically stable state; therefore, it is necessary to short-circuit the measuring electrodes 1 and 3 (see Figure 14), observe the changing short-circuit current (I_0), and, if necessary, increase the sensitivity of the measuring device. We continue until the short-circuit current reaches a roughly constant value, small compared to the expected steady value after 100 minutes. If the current changes direction, it must still be short-circuited, even if it passes through 0. We try to record the magnitude and direction of the current I_0 when it is constant, which can take several hours. In the next step, DC voltage is connected with a timer at the same time. Unless it is specified otherwise, measurement readings should be taken after each of the following polarization times: 1min, 2 min, 10 min, 50 min and 100 min. When two subsequent measurements give the same value, the test may be terminated, and the value obtained is used to calculate the volume resistivity. The time of the first measurement, which gave the same values is recorded. If a steady value has not been reached even after 100 minutes, the volume resistivity is given as a function of polarization time. [26]

Surface resistivity

Measurement starts with connecting specified DC voltage and determining the resistance between electrodes 1 and 2 (see Figure 14). The resistance must be measured after 1 minute of polarization, even if the current does not reach a stable value at this time. [26]

Calculating volume resistivity

Volume resistivity is calculated with equation (10).

$$\rho = R_x \cdot \frac{A}{h} \tag{10}$$

In equation (10), ρ [Ωm] stands for volume resistivity, R_x [Ω]stands for volume resistance measured, A [m^2] stands for effective area of the electrodes, and h [m] stands for the average thickness of the specimen. The equations for determining the effective area of the electrodes vary, depending on the arrangement of the electrodes. The following equations apply for several basic electrode arrangements: [26]

$$circular\ electrodes: \quad A = \pi(d_1 + \frac{g)^2}{4} \tag{11}$$

$$rectangular\ electrodes: \quad A = (a + g) \tag{12}$$

$$square\ electrodes: \quad A = (a + g)^2 \tag{13}$$

$$tubular\ electrodes: \quad A = \pi(d_0 - h)(l_1 + g) \tag{14}$$

Where d_0, d_1, g, h, and l_1 are dimensions described in Figure 15, and a stands for the length of the electrode and b stands for the width of the electrode. All these dimensions are in metres.

For some materials, short-circuit current may be not neglectable relative to the steady-state current value during polarization. In these cases, the volume resistance is determined by equation (15). [26]

$$R_x = \frac{U_x}{I_s \pm I_0} \tag{15}$$

In equation (15), R_x represents measured resistance, U_x voltage connected to the electrodes, I_s stands for steady current flow during polarization after 1 min, 10 min and 100min and I_0 is short-circuit current before polarization. The minus sigh is used if I_0 has the same direction as I_s; otherwise, sigh plus is used. [26]

Calculating surface resistivity

Surface resistivity is calculated with equation (16), where R_x [Ω] stands for measured resistance, p [m] is effective electrode circumference, g [m] is the distance between electrodes, and ρ is the surface resistivity itself. Effective electrode circumference depends on an electrode arrangement again. Equations (17), (18), (19) and (20) are for calculating effective circumference for basic electrode arrangements. [26]

$$\rho = R_x \cdot \frac{p}{g} \tag{16}$$

$Circular\ electrodes$: $$p = \pi(d_1 + g) \tag{17}$$

$Rectangular\ electrodes$: $$p = 2(a + b + 2g) \tag{18}$$

$Square\ electrodes$: $$p = 4(a + g) \tag{19}$$

$Tubular\ electrodes$ $$p = 2\pi d_0 \tag{20}$$

4.2 Reproducibility

As the electrical resistance of the tested specimen depends on the test conditions and the inhomogeneity of the individual specimen, the measurements often do not have a better reproducibility than ± 10%. It is possible to obtain different results by orders of magnitude under seemingly identical conditions. For different measurements on similar specimens to

be comparable, measurements must be done under the same electric field intensity influence. [26]

4.3 Erosion inception under multiple electric field strengths

The authors of the paper [12] did a series of tests to learn about resistivity against OCP materials' erosion. All their tested samples were simultaneously aged thermally and electrically in an oven. In Figure 16 test setup can be seen. Test setup base is a metal tube insulated by insulation. Furthermore, the specimen is mounted with grounding electrodes, a single layer of OCP material with 50% of overlapping and ECP on the ends of the tube to prevent surface discharges. The observed criterion is the elapsed time until visible erosion signs appear on the surface of OCP material. High voltage was applied to the metal tube, and OCP tape was grounded via grounding electrodes. One of the relevant parameters is electrical field strength because partial discharge activity is considered the main reason for erosion mechanisms. [12]

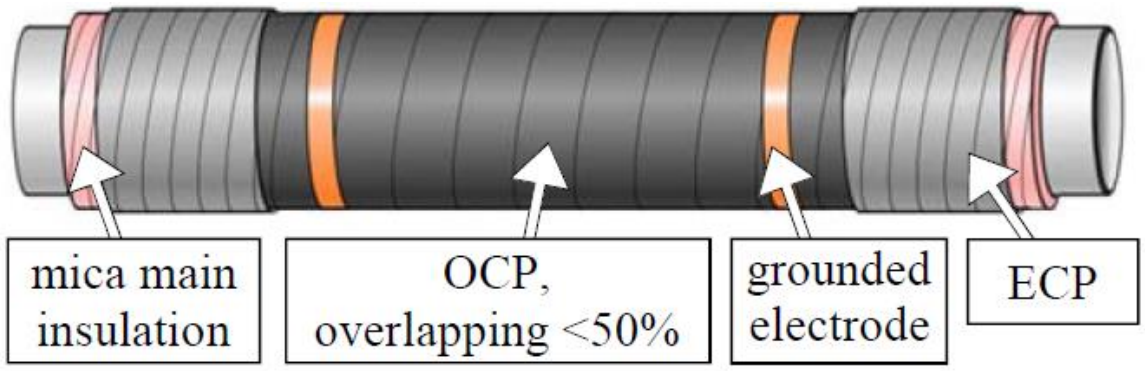

Figure 16 Test setup for evaluation of OCP erosion inception, taken from [12]

For the tested cylindrical specimens, the electrical field strength can be calculated using equation (21), where U represents applied voltage, r_1 represents tube radius, and r_2 stands for the outer radius of the main insulation. Localised field strength variations may occur due to imperfections, but they are not considered for this test. The dependency of erosion

inception time test was performed under constant temperature 130 °C, and the authors of this research paper tested three different OCP tapes. Two commercially available tapes, each made by a different manufacturer (labelled as Tape #1 and Tape #3) and one newly developed corona-protection tape. [12]

$$E_{OCP} = \frac{U}{r_2 \cdot ln\frac{r_2}{r_1}} \tag{21}$$

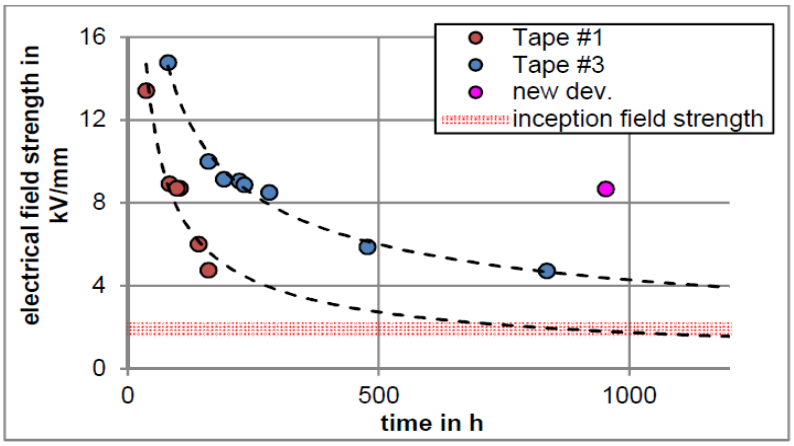

Figure 17 OCP erosion inception time under different electric field strengths at 130 °C, linear plot, taken from [12]

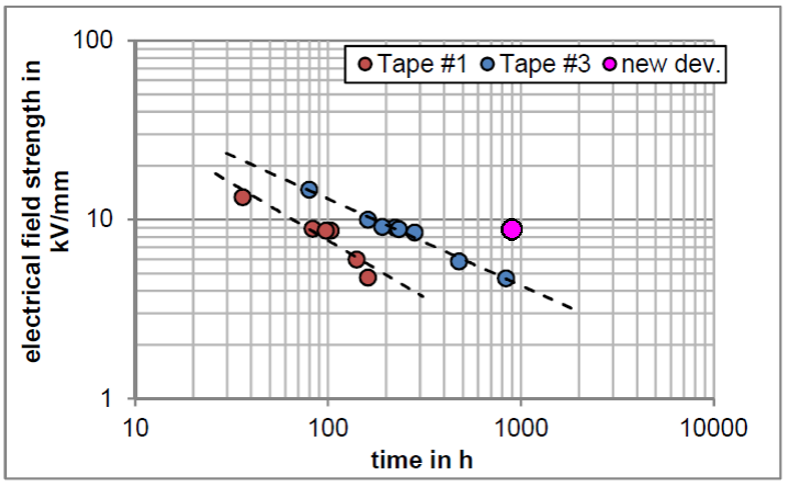

Figure 18 OCP erosion inception time under different electric field strengths at 130 °C, log-log plot, taken and modified from [12]

Each point in the diagrams (Figure 17 and Figure 18) represents an average value of multiple specimens' inception time. This test helps to show differences of resistance against partial discharges between tapes.

4.4 Evaluation of erosion resistivity of corona protection systems

In another paper [13], the authors tried to understand the ageing process of OCP tapes. They focused on the erosion of tape materials and performed a series of experiments. The authors of the paper tried to understand the phenomenon of erosion, which affects mainly air-cooled machines. [27] [28]

The first experiment in paper [13] reproduced erosion phenomenon in laboratory conditions on a simplified specimen. A round bar of aluminium was taped with several layers of mica insulation. This insulation was furthermore covered with OCP tape. The tested specimen can be seen in Figure 19. The left side of the tested specimen had double the amount of layers compared to the right side. The specimen was exposed to heightened electrical and thermal stresses until the first visible signs of degradation were visible, after standard impregnation and curing cycle to ensure the most realistic simulation as possible.

Figure 19 Round profile specimen for simulation of OCP erosion [13]

First visible erosion could be seen on the left side of the tested specimen, where the layer of OCP is thinner. Visible eroded stripes (the white lines pointed by yellow arrows are caused by erosion) could correlate with the edges of mica tape, which is located underneath

the OCP tape. The thicker layer on the left side looks unaffected on its surface. A cut in lengthwise direction through insulation was performed to examine the interface of OCP and insulation. After examination, a cavity on the edge of the main insulation was discovered. This cavity can be seen in Figure 20. The observed cavity clearly extends to the OCP layer. This appeared to be an effect of erosion, which could not penetrate the whole OCP layer because of its thicker material volume. Based on these findings, OCP erosion can be described as a successive degradation of semi conductive material caused by partial discharges. Partial discharges are responsible for this degradation formed due to local highly concentrated electrical field and local thermal hot spots, caused by inhomogeneous permittivity and geometrical alignment of materials used in the manufacturing process. It is also safe to say, that the electric field distribution and hot spots are significant contributors to the intensity of creation of partial discharges, which cause erosion of OCP layers. [13]

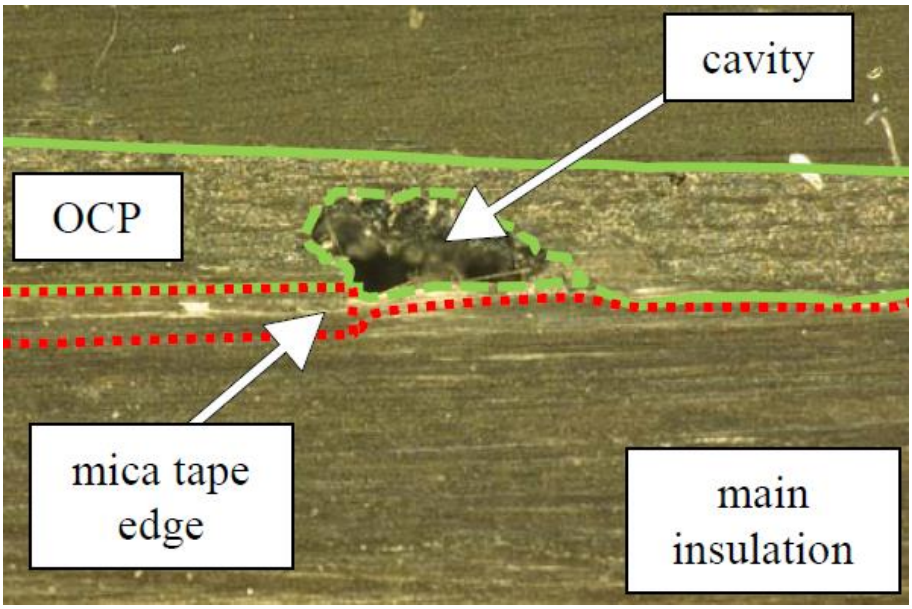

Figure 20 Microscopic picture of examined insulation on the left side of tested specimen [13]

4.5 Measuring surface resistivity of ECP protection

The authors of the paper [14] developed a new filler material for ECP protection with the goal of more precise control of its electrical parameters. This was realized by nano-

technological coating with special doping particles made of stannic oxide (SnO). With this process, the structure of particles can be adjusted by utilizing a more uniform geometric structure with a high aspect ratio and similar dimensions. The aspect ratio allows the expansion of anisotropic oriented current paths tunnel effect with non-linear characteristic. [14] [15]

As a substrate material for SnO particles, mica was used, embedded in the known polymer matrix. The polymer consists of epoxy resin. Mica is known for its corona resistance, low dielectric dissipation factor and its good thermal conductivity properties. By doping with SnO, the composite material gets desired non-linear electrical behaviour. This non-linear property can be further adjusted by the doping concentration and using different coating materials. [14]

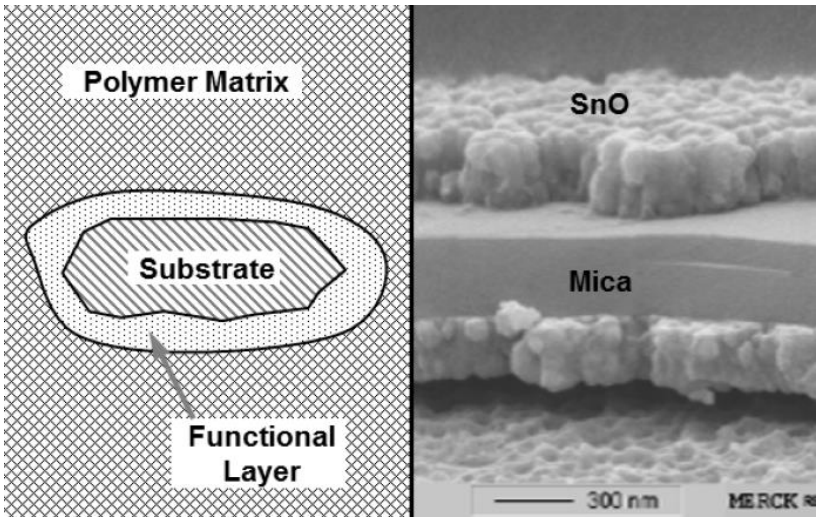

Figure 21 Schematic view of SnO particles embedded in the polymer matrix (left) and photograph of particles made with the electron microscope, taken from [15]

To learn the electrical properties of the ECP protection, the authors of the paper [14] did an experiment. The setup of the experiment can be seen in Figure 22. Two electrodes, made of conductive silver paint, are fixed at the surface of the measured material, which is then fixed on a glass slab. The electrodes are connected to high voltage using a high-temperature

cable and conduct over a feed-through to the DC voltage source and ammeter. With this setup, the square resistivity is measured. With the values of square resistance measured, it is then possible to calculate current density depending on the electrical field strength (E-J curves), which the paper's authors used as the evaluation criterion. The experiment was placed into a climate cabinet to ensure steady temperature and relative humidity for all tested specimens. [14]

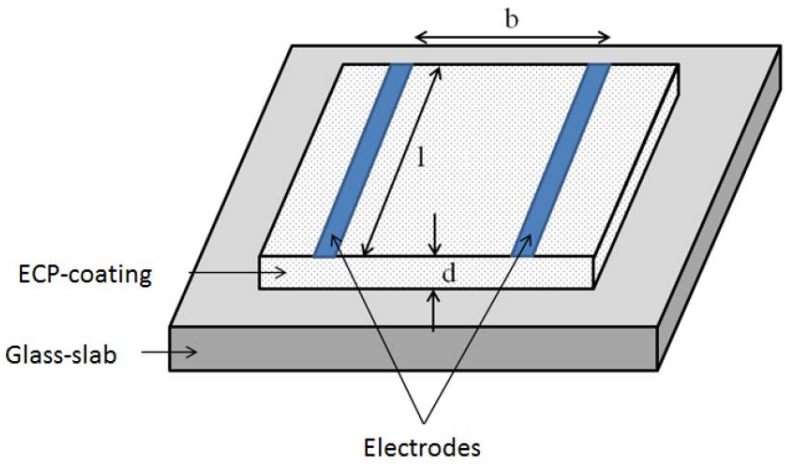

Figure 22 Experiment setup for measuring square resistivity, taken from [14]

For the first set of measurements, the climate cabinet temperature was set to 30°C and relative humidity to 30%. The measurement voltage varied from 500 V to 5000 V DC for modelling the desired E-J curves. Five different specimens were created. Individual specimens were treated with two different doping concentrations (E08 and E12), which could be combined with each other. The ratio between E08 and E12 for different measured specimen can be seen in Table 3. Results of measuring current density depending on the electrical field referred to an applied voltage of 1 kV can be seen in Figure 23.

Table 3 E08 and E12 concentration ratios for tested specimens, taken from [14]

Ratio			
Probe-#	**E08 [%]**	**E12 [%]**	**Layer thickness**
177-1	100	0	40
179-1	65	35	70
178-1	50	50	70
179-2	35	65	70
177-2	0	50	60

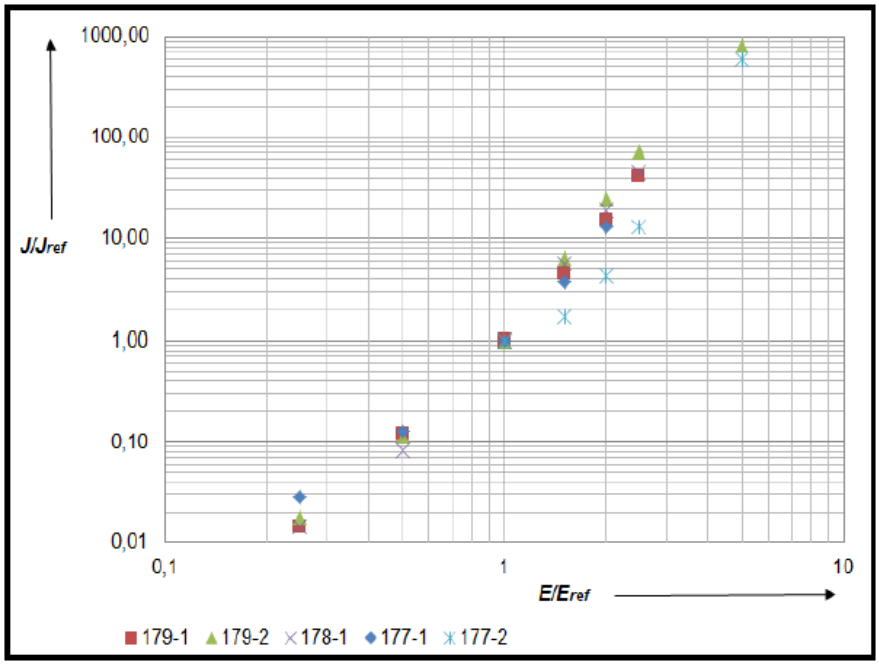

Figure 23 Current density depending on the electrical field referred to an applied voltage of 1 kV, taken from [14]

5 Experimental measurements

5.1 Introduction of first set of materials

To better understand the properties of materials used for anti-corona protection, deep material analysis was performed. In this analysis, raw tapes from well-known tape manufacturers were examined. All of them were examined under an electron microscope. Energy-dispersive X-ray spectroscopy (EDXA) was also performed to analyse the samples

as well as possible. The results of these two experiments can be seen below. Only some of the electron microscope photos are shown in the chapter below, and the rest can be found in attachments. A similar approach was the investigations with EDXA analysis. Tapes are labelled as Material A, B and C to be able to distinguish between them.

5.1.1 Material A

A conductive non-woven tape with a given resistance of 1000 Ω/□, is referred in this chapter as Material A. This tape is described as PET-non-woven with additional polyester threads inserted in machine direction impregnated with a cured carbon-filled resin. This tape contains a small amount of zinc-naphthenate as an accelerator. According to IEC 60085, this tape is in thermal class F. More of its properties can be seen in Table 4.

Table 4 Material A properties

Properties	Units		Test method
Thickness	mm	0,05	DIN EN 29073-2
Area weight	g/m2	45	DIN EN 29073-2
Area weight of backing material	g/m2	30	DIN EN 29073-2
Tensile strength	N/50mm	≥ 60	DIN EN 29073-2
Surface resistance (without accelerator)	Ω/□	1000	DIN VDE 0303-3

5.1.2 Material B

A conductive non-woven tape with a given resistance of 1000 Ω/□ is labelled as Material B in this experiment. The tape consists of polyester fibres in the warp direction and glass fibres in the weft direction. It is impregnated with an electrically conducting binding agent, which is fully cured. As in previous material, zinc-naphthenate is used as an accelerator and is in the same thermal class (Class F) according to IEC 60085. More of its properties can be seen in Table 5.

Table 5 Material B properties

Properties	Units	Values	Test Method
Thickness	mm	0,08	DIN EN 29073-2
Area weight	g/m2	65	DIN EN 29073-2
Area weight of backing material	g/m2	45	DIN EN 29073-2
Tensile strength	N/50mm	≥ 200	DIN EN 29073-2
Surface resistance (without accelerator)	Ω/□	1000	DIN VDE 0303-3
Elongation at break	%	≥ 20	DIN EN 29073-2

5.1.3 Material C

A conductive tape with a given resistance of 1000 Ω/□ is labelled as Material C. This tape is an electrically conducting glass fabric. Material C is also impregnated with zinc-naphthenate as an accelerator and falls into the same thermal class F according to IEC 60085. In Table 6, more of its properties can be seen.

Table 6 Material C properties

Properties	Units		Test method
Thickness	mm	0,09	DIN EN 29073-2
Area weight	g/m2	125	DIN EN 29073-2
Area weight of base material	g/m2	105	DIN EN 29073-2
Tensile strength (without accelerator)	N/50mm	≥ 300	DIN EN 29073-2
Surface resistance (without accelerator)	Ω/□	appr. 1000	DIN VDE 0303-3
Elongation at break	%	≥ 1,5	DIN EN 29073-2

5.2 Microscopy analysis

The microscopy analysis using electron microscope of used materials has been performed and described below. Figures of photos made with electron microscope are below, and they are supplemented by EDXA (Energy Dispersive X-ray Analysis). Two different EDXA analysis were performed, one where there was an entire area analysed and one where only one spot on a picture was analysed.

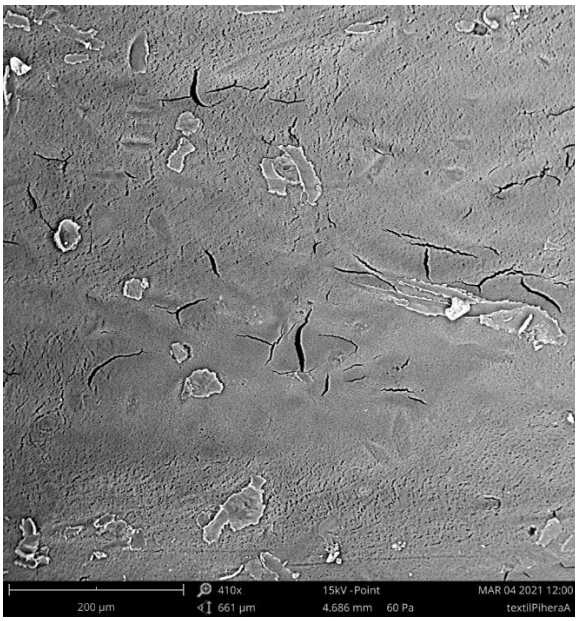

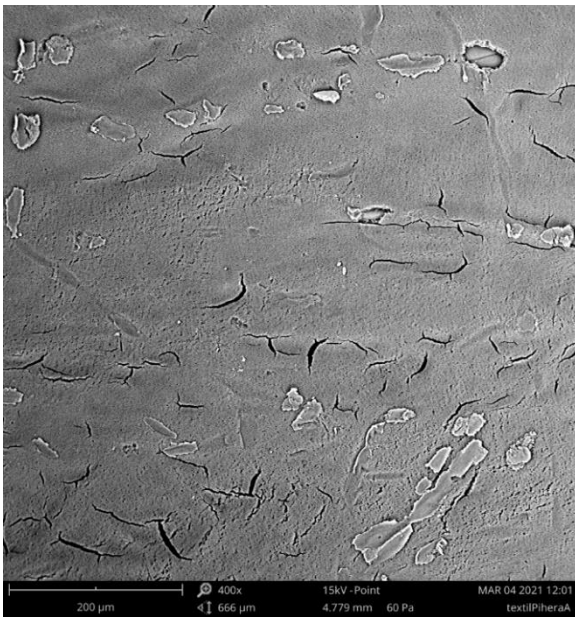

Figure 24 and Figure 25 Photographs of Material A made using an electron microscope

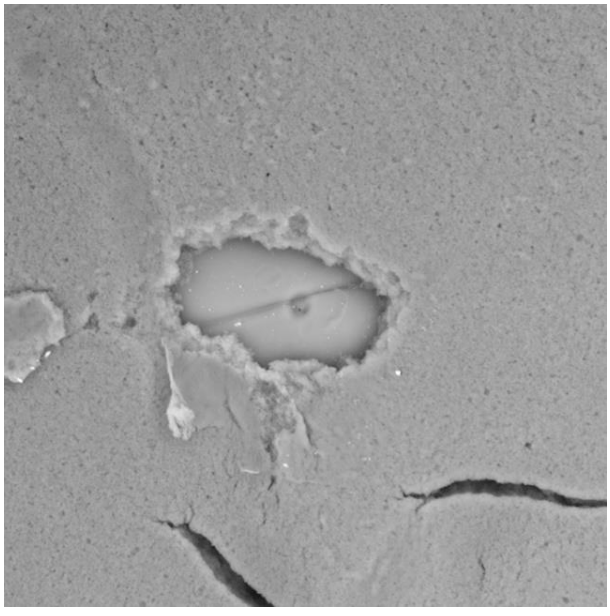

Figure 26 Photograph of an area on Material A, where area EDXA analysis was performed

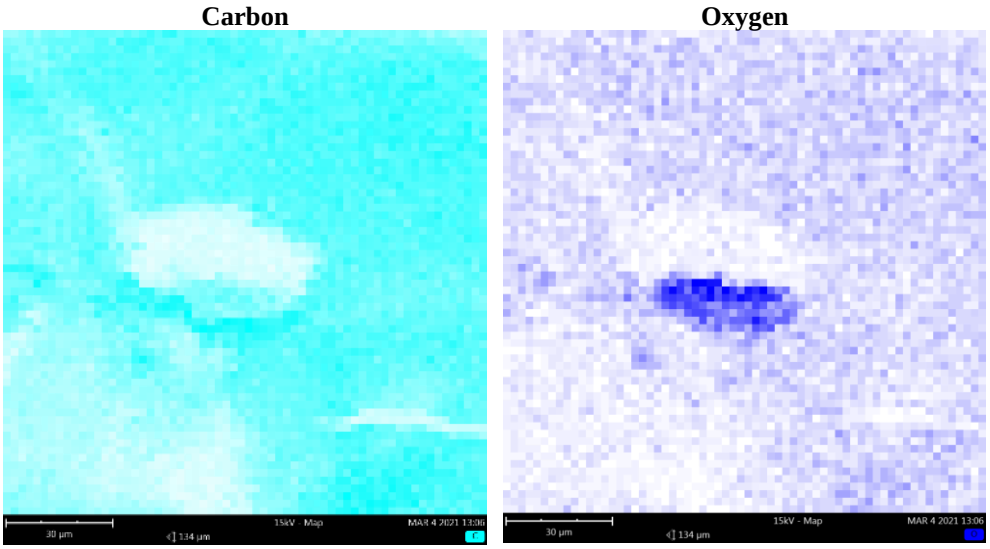

Figure 27 and Figure 28 Results of area EDXA analysis on Material A

Table 7 Results of area EDXA analysis on Material A

Element Number	Element Symbol	Element Name	Atomic Conc.	Weight Conc.
6	C	Carbon	62.47	55.55
8	O	Oxygen	37.53	44.45

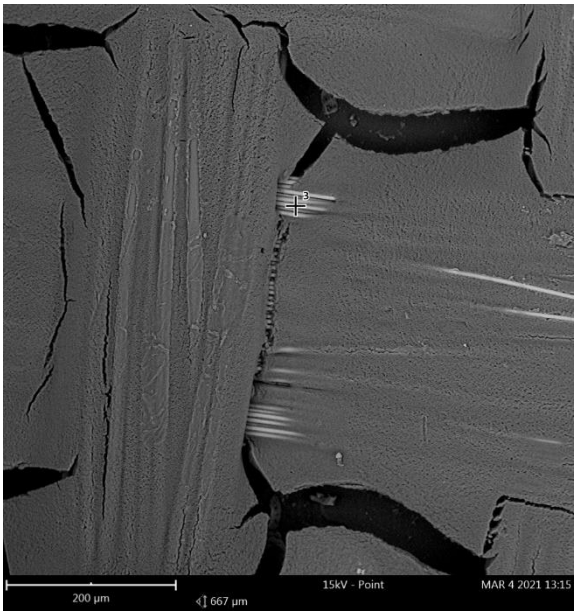

Figure 29 Photograph of an area on Material B, where spot EDXA analysis was performed, the spot where analysis was performed is marked by the black cross

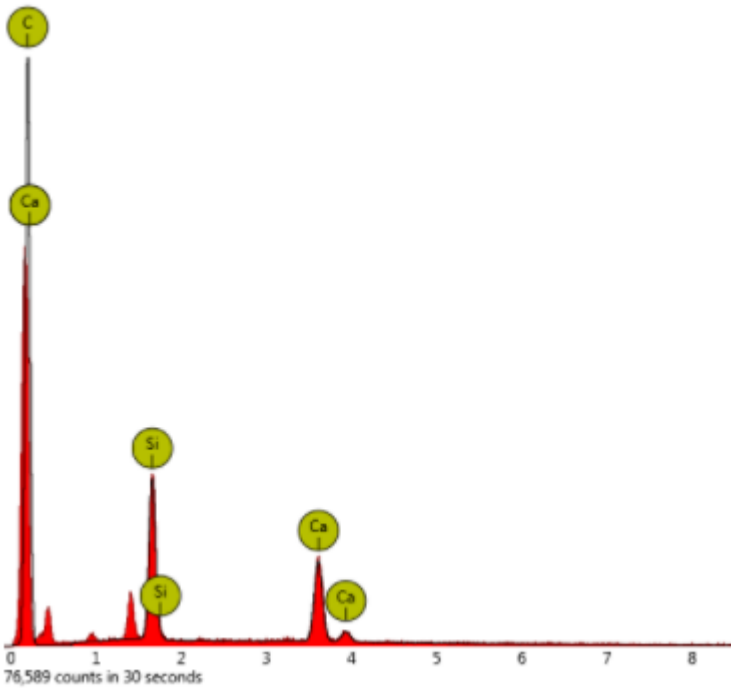

Figure 30 EDXA spot analysis results on material B

Table 8 Results of spot EDXA analysis on Material B

Element Number	Element Symbol	Element Name	Atomic Conc.	Weight Conc.
6	C	Carbon	72.91	49.05
20	Ca	Calcium	12.41	27.85
14	Si	Silicon	14.69	23.10

Figures 24 - 30, along with Table 7 and Table 8, are the only results directly shown in this thesis; as said before, the rest of the results can be seen in attachments. Material A, B and C showed, in EDXA analysis, a large predominance of carbon, along with trace amounts of silicon, calcium, oxygen and zinc.

5.3 Surface resistivity

5.3.1 Introduction to experiment

This experiment is about measuring the finished and fully cured OCP samples. These samples consisted of the main insulation with OCP, which was cut out from a new stator bar. Measurements were about the surface resistance of the samples. Three different methods were used, measuring with copper straps and with two different probes.

Three kinds of samples were sent. One sample is made using Resin Rich technology, and two samples are made using VPI technology. There were sent two insulating bars for each kind of samples. Samples are labelled as TB 51 (Resin Rich), BU 81 (VPI) and BU 34 (VPI).

The first method of measuring has used a probe, which measures surface resistance between two longitudinal lines of conductive materials pressed onto the insulating bar. The second method used a probe with two point-like contacts also pressed onto the bar surface. The third method consisted of attaching multiple copper straps and measuring the material's surface resistance. Further details about used methods are described in individual chapters about each measurement method. Volume resistivity of one bar was also measured.

Because there are two pieces of each sample, they were furthermore divided into samples A and B. Samples can be seen in Figure 31. These samples were also examined under an electron microscope, and EDXA analysis was performed; results can be seen in attachments.

Figure 31 Fully cured and completed OCP samples

5.3.2 Measuring surface resistivity with a longitudinal probe

With the first method using the probe with longitudinal contacts, measurements were taken in three different positions. The bottom, middle and top parts of the samples were measured, as seen in Figure 33. In Figure 33, the weight used to stabilise the probe's contact areas can be seen. The weight weighs 1kg. In Figure 32, the probe itself can be seen. Samples BU 34 were moreover divided into left and right parts because of their width. With this probe, the resistance between the contacts is measured. Results can be seen in Table 9.

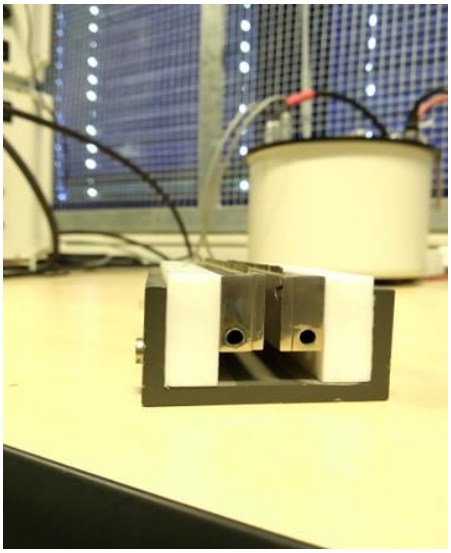

Figure 32 Longitudinal probe

Figure 33 Measuring with a longitudinal probe

Table 9 Results of measuring resistance with a longitudinal probe

TB 51 A [Ω]	TB 51 B [Ω]	BU 81 A [Ω]	BU 81 B [Ω]	BU 34 A [Ω]		BU 34 B [Ω]	
				Left side	Right side	Left side	Right side
125,3	84,2	361	260	826	812	715	515
108,4	82,3	414	351	756	438	971	631
117,7	102,4	358	318	747	1769	951	1191

For calculating surface resistivity ρ_s, equation (22) was used, where l_p represents the electrode's length and d_p represents the distance between electrodes. Results can be seen in Table 10.

$$\rho_S = R \times \frac{l_p}{d_p} \tag{22}$$

Table 10 Surface resistivity calculated from longitudinal probe results

TB 51 A [Ω]	TB 51 B [Ω]	BU 81 A [Ω]	BU 81 B [Ω]	BU 34 A [Ω]		BU 34 B [Ω]	
				Left side	Right side	Left side	Right side
1253	842	3610	2600	8260	8120	7150	5150
1084	823	4140	3510	7560	4380	9710	6310
1177	1024	3580	3180	7470	17690	9510	11910

5.3.3 Measuring surface resistivity with point probe

The next method of measurement was done using a probe with two point-like contacts. The probe detail can be seen in Figure 34. All samples were divided into sections 2cm (horizontally)×3cm (vertically) as seen in Figure 35, Figure 36 and Figure 37, where you can also see the measurement results.

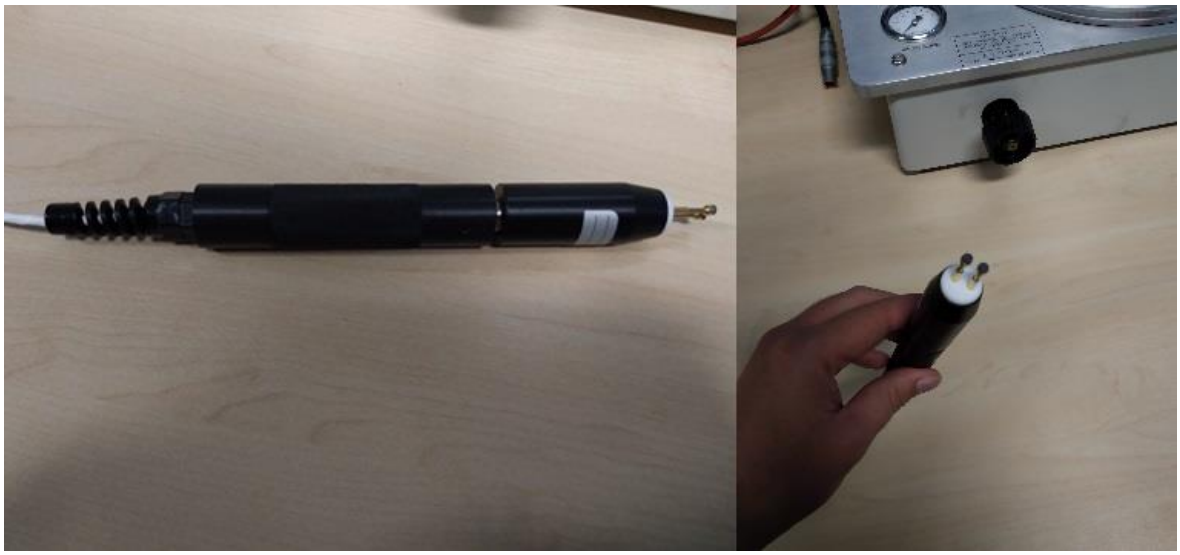

Figure 34 Point probe

Figure 35 Point probe results on samples TB 51, all values are in Ohms [Ω]

Figure 36 Point probe results on samples BU 51, all values are in kilo Ohms [kΩ]

Figure 37 Point probe results on samples BU 34, all values are in kilo Ohms [kΩ]

For calculating surface resistivity, the same formula as in equation (22) was used. As l_p, the electrodes' diameter was used, and as d_p, a gap between the electrodes was used. Results can be seen in Table 11.

Table 11 Surface resistivity of samples calculated from point probe results

TB 51 A [Ω]		TB 51 B [Ω]		BU 81 A [Ω]		
131,14	161,57	117,00	104,14	296,14	446,57	732,86
113,57	143,57	112,29	112,29	564,86	450,86	1572,86
106,29	117,00	121,29	125,57	393,00	289,29	278,57
102,00	106,29	108,86	108,43	701,57	378,43	1675,71
109,29	112,29	107,57	111,43	679,29	1288,71	1525,71
127,71	121,29	132,43	113,57	555,86	366,86	1718,57
123,86	146,57	126,43	127,29	302,14	247,71	478,71
120,43	117,86	126,00	114,00	244,29	562,71	1537,71
120,86	120,00	119,57	126,43	317,14	481,29	744,00
BU 81 B [Ω]			BU 34 A [Ω]			
1020,00	518,57	848,57	250,71	405,86	1078,29	973,29
617,14	398,57	280,71	524,57	926,14	476,57	836,14
326,57	334,29	1697,14	1162,29	873,86	440,57	765,00
3394,29	1654,29	1572,86	933,00	1037,14	676,29	270,86
1260,00	510,00	720,00	866,14	845,14	538,29	345,86
797,14	462,86	681,43	499,71	481,71	464,14	293,57
450,00	445,71	291,43	763,71	335,14	249,86	558,86
1392,86	291,43	304,29	970,71	1365,43	813,43	289,29
878,57	951,43	1457,14	829,29	457,29	924,43	740,57
BU 34 B [Ω]						
510,43	514,71	793,29	281,14			
1241,57	806,57	597,00	648,00			
516,43	405,00	744,86	786,00			
375,43	1236,00	727,29	674,57			
449,57	677,57	363,00	910,71			
282,00	580,29	988,71	936,43			
412,71	546,86	740,57	1219,71			
1042,29	1130,14	399,43	796,71			
1034,57	786,86	963,00	407,57			

5.3.4 Measuring surface resistivity with copper straps

The third method of measurement used copper straps attached to the samples. Each strap was 1 cm wide and between each strap was 2 cm gap. Firstly, the resistance between straps was measured, and then surface resistivity was calculated. Measurement results can be seen

in Table 12. How the straps were attached can be seen in Figure 38. Numbers in Figure 38 represent rows in Table 12 Table 13.

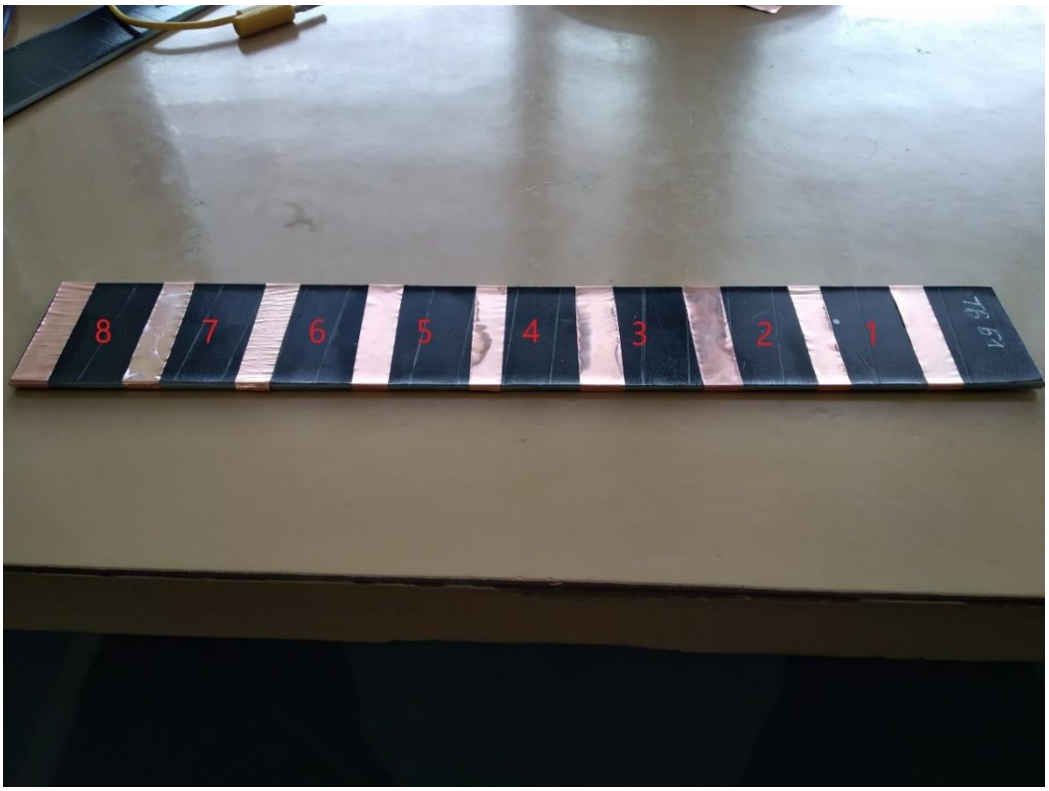

Figure 38 Copper straps configuration on samples

Table 12 Measured resistance using copper straps method

TB 51 A [Ω]	TB 51 B [Ω]	BU 81 A [Ω]	BU 81 B [Ω]	BU 34 A [Ω]	BU 34 B [Ω]
454	384	1101	1395	689	524
440	357	1106	1161	673	478
358	315	2801	3229	591	449
428	363	2069	1691	594	551
354	361	1596	1684	588	501
404	381	977	757	623	598
438	405	1126	1475	704	633
426	367	1395	6430	664	684

For calculating surface resistivity, the same formula as in equation (22) was used again. As l_p, the length of the copper strap was used, and as d_p, the distance between straps, which is 1cm. Results can be seen in Table 13.

Table 13 Surface resistivity calculated from measuring results

TB 51 A [Ω]	TB 51 B [Ω]	BU 81 A [Ω]	BU 81 B [Ω]	BU 34 A [Ω]	BU 34 B [Ω]
908	768	3137,85	3975,75	2824,9	2148,4
880	714	3152,1	3308,85	2759,3	1959,8
716	630	7982,85	9202,65	2423,1	1840,9
856	726	5896,65	4819,35	2435,4	2259,1
708	722	4548,6	4799,4	2410,8	2054,1
808	762	2784,45	2157,45	2554,3	2451,8
876	810	3209,1	4203,75	2886,4	2595,3
852	734	3975,75	18325,5	2722,4	2804,4

5.3.5 Measurement of volume resistivity

The last measurement in this experiment was volume resistivity measurement. Because of the dimensions of the circular probe, only sample BU 34 was able to be measured. The sample was cut into 8×8 cm piece, as seen in Figure 39. When measuring, the voltage must have been applied onto the insulation layer, not a semi-conductive one. When the voltage was applied on the semi-conductive layer, any results could have been acquired.

Figure 39 Sample BU 34 cut into 8x8 cm

1000 Volts were applied to the insulation layer from one of the probe's electrodes, and then the electrical current flowing through the sample into the grounding electrode was measured. The current had a value of 1,4 nA. To determine the probe's effective area,

equation (23) from norm ČSN IEC 93 was used. To calculate the resistivity of the sample, a standard equation (24) was used. The thickness of the sample is l = 4mm, and the dimensions of the probes are: d_1 = 5 cm, g = 4mm.

$$A = \pi \times \frac{(d_1 + g)^2}{4} = \pi \times \frac{(5 \times 10^{-2} + 4 \times 10^{-3})^2}{4} = 2{,}29 \times 10^{-3}\ m^2 \quad (23)$$

$$\rho_V = \frac{U}{I} \times \frac{A}{l} = \frac{1000}{1{,}4 \times 10^{-9}} \times \frac{2290{,}2}{4 \times 10^{-3}} = 714{,}29 \times 10^{9} \times \frac{2290{,}2}{4 \times 10^{-3}} = 4{,}09 \times 10^{11}\Omega\text{m} \quad (24)$$

5.3.6 Statistics

This chapter shows basic statistics, such as average, median, standard deviation and coefficient of variation. All statistical data are shown in the tables below.

5.3.6.1 Average values

Table 14 Average values of resistance and resistivity, calculated from results of longitudinal probe method

	TB 51 A [Ω]	TB 51 B [Ω]	BU 81 A [Ω]	BU 81 B [Ω]	BU 34 A [Ω]		BU 34 B [Ω]	
					Left side	Right side	Left side	Right side
resistance	117,13	89,63	377,67	309,67	776,33	1006,33	879,00	779,00
resistivity	1171,33	896,33	3776,67	3096,67	7763,33	10063,33	8790,00	7790,00

Table 15 Average values of resistance and resistivity, calculated from results of point probe method

	TB 51 A [Ω]		TB 51 B [Ω]		BU 81 A [Ω]		
resistance	273,56	297,22	277,78	270,44	1051,11	1169,89	2661,22
resistivity	117,24	127,38	119,05	115,90	450,48	501,38	1140,52
	BU 81 B [Ω]			BU 34 A [Ω]			
resistance	2628,00	1443,33	2036,11	1763,00	1744,22	1467,89	1315,33
resistivity	117,24	127,38	119,05	115,90	450,48	501,38	1140,52
	BU 34 B [Ω]						
resistance	1520,56	1732,89	1637,78	1726,89			
resistivity	651,67	742,67	701,90	740,10			

Table 16 Average values of resistance and resistivity, calculated from results of copper straps method

	TB 51 A [Ω]	TB 51 B [Ω]	BU 81 A [Ω]	BU 81 B [Ω]	BU 34 A [Ω]	BU 34 B [Ω]
resistance	412,75	366,63	1521,38	2227,75	640,75	552,25
resistivity	825,50	733,25	4335,92	6349,09	2627,08	2264,23

5.3.6.2 Median values

Table 17 Median values of resistance and resistivity, calculated from results of longitudinal probe method

	TB 51 A [Ω]	TB 51 B [Ω]	BU 81 A [Ω]	BU 81 B [Ω]	BU 34 A [Ω]		BU 34 B [Ω]	
					Left side	Right side	Left side	Right side
resistance	117,70	84,20	361,00	318,00	756,00	812,00	951,00	631,00
resistivity	1177,00	842,00	3610,00	3180,00	7560,00	8120,00	9510,00	6310,00

Table 18 Median values of resistance and resistivity, calculated from results of point probe method

	TB 51 A [Ω]		TB 51 B [Ω]		BU 81 A [Ω]		
resistance	281,00	280,00	279,00	265,00	917,00	1042,00	3560,00
resistivity	120,43	120,00	119,57	113,57	393,00	446,57	1525,71
	BU 81 B [Ω]			BU 34 A [Ω]			
resistance	2050,00	1080,00	1680,00	1935,00	1972,00	1256,00	1304,00
resistivity	878,57	462,86	720,00	829,29	845,14	538,29	558,86
	BU 34 B [Ω]						
resistance	1191,00	1581,00	1728,00	1834,00			
resistivity	510,43	677,57	740,57	786,00			

Table 19 Median values of resistance and resistivity, calculated from results of copper straps method

	TB 51 A [Ω]	TB 51 B [Ω]	BU 81 A [Ω]	BU 81 B [Ω]	BU 34 A [Ω]	BU 34 B [Ω]
resistance	427,00	365,00	1260,50	1579,50	643,50	537,50
resistivity	854,00	730,00	3592,43	4501,58	2638,35	2203,75

5.3.6.3 Standard deviations

All standard deviation values in the tables below are calculated from values of resistivity. All values given are in **Ω**.

Table 20 Standard deviations of values from longitudinal probe method results

TB 51 A	TB 51 B	BU 81 A	BU 81 B	BU 34 A		BU 34 B	
				Left side	Right side	Left side	Right side
69,11	90,61	257,21	376,15	353,11	5604,85	1162,53	2951,52

Table 21 Standard deviations of values from point probe method results

TB 51 A		TB 51 B		BU 81 A		
9,42	17,52	7,98	7,96	166,34	292,91	539,34
BU 81 B			BU 34 A			
867,30	407,66	535,77	265,54	327,41	250,17	257,19
BU 34 B						
332,72	265,51	205,51	266,04			

Table 22 Standard deviations of values from copper straps method results

TB 51 A	TB 51 B	BU 81 A	BU 81 B	BU 34 A	BU 34 B
70,77	48,91	1674,24	4916,39	181,44	309,45

5.3.6.4 Coefficient of variation

All coefficients of variation in the tables below are calculated from values of resistivity. All values given in these tables are in percentages.

Table 23 Coefficient of variation values, longitudinal probe method [%]

TB 51 A	TB 51 B	BU 81 A	BU 81 B	BU 34 A		BU 34 B	
				Left side	Right side	Left side	Right side
5,90	10,11	6,81	12,15	4,55	55,70	13,23	37,89

Table 24 Coefficient of variation values, point probe method [%]

TB 51 A		TB 51 B		BU 81 A		
8,04	13,75	6,70	6,87	36,92	58,42	47,29
BU 81 B			BU 34 A			
739,78	320,03	450,04	229,10	72,68	49,90	22,55
BU 34 B						
51,06	35,75	29,28	35,95			

Table 25 Coefficient of variation values, copper straps method [%]

TB 51 A	TB 51 B	BU 81 A	BU 81 B	BU 34 A	BU 34 B
8,57	6,67	38,61	77,43	6,91	13,67

5.4 Temperature properties of OCP

In this experiment, the same samples were used as in the first one. This time though, only one bar from each sample was measured. Selected bars can be seen in Figure 40. This time, two different measurements were performed. One measurement was about learning temperature-dependent resistance and the second one was about learning how the samples will warm up when exposed to electrical current.

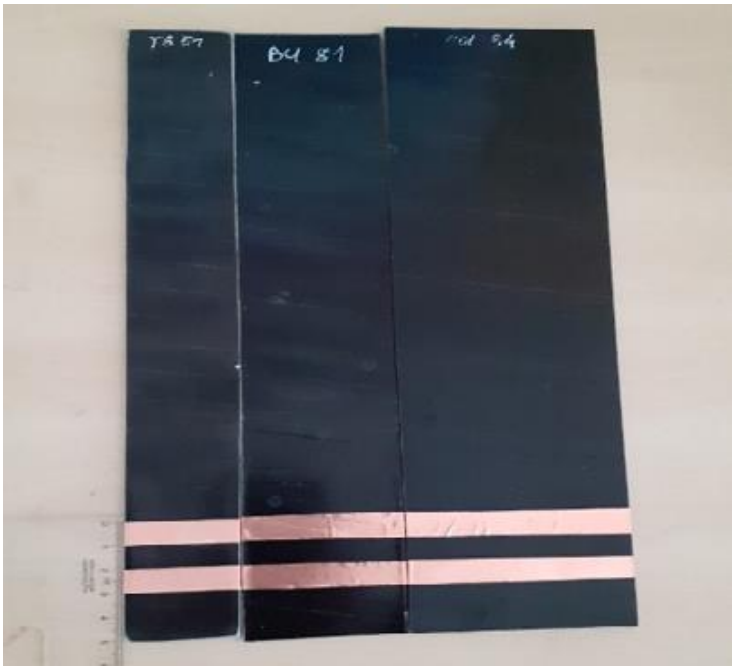

Figure 40 Samples chosen for the experiment

5.4.1 Temperature-dependent resistance

In this chapter, the results of temperature-dependent resistance measurement are shown. For this measurement, a laboratory oven was used, as seen in Figure 41. Measuring electrodes were connected onto copper straps attached to samples, as seen in Figure 42.

Copper straps were attached with conductive glue. Each strap is 1 centimetre wide, and they are 1 cm apart. Bottom straps are placed 2 centimetres from the bottom part of the samples, as seen in Figure 40. Samples were placed in the oven, and then the oven was turned on. For connecting measuring electrodes and measuring devices, silicon wires were used in the oven due to oven heat. Wires ran from the inside out of the oven, so samples could be measured directly in the oven without the need of taking them out for every measurement. The starting temperature was 30 °C, and the maximal temperature was 160 °C. Measurement was taken after every 10 °C of warming up. Results can be seen in Table 26, Graph 1 and Graph 2. A single Graph was made for BU 81 because its values are in order of magnitude different from the remaining 2 samples.

Figure 41 Laboratory oven used for measurement

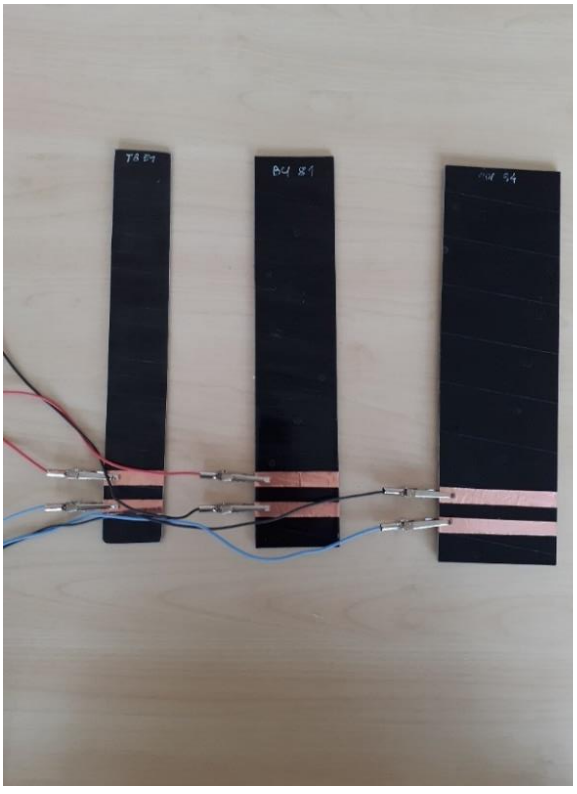

Figure 42 Electrode attachment to the samples

Table 26 Temperature-dependent resistance measurement results

Temperature [°C]	TB 51 [Ω]	BU 81 [Ω]	BU 34 [Ω]
30	229,2	9720	626
40	229,7	9780	627
50	233,6	9880	630
60	244,5	10250	658
70	255	10730	689
80	281,3	12040	792
90	304,5	12890	959
100	335,9	13960	1198
110	443	15530	1446
120	534	23600	1801
130	593	74900	2360
140	624	35620	2853
150	671	127000	3420
160	673	6010000	5110

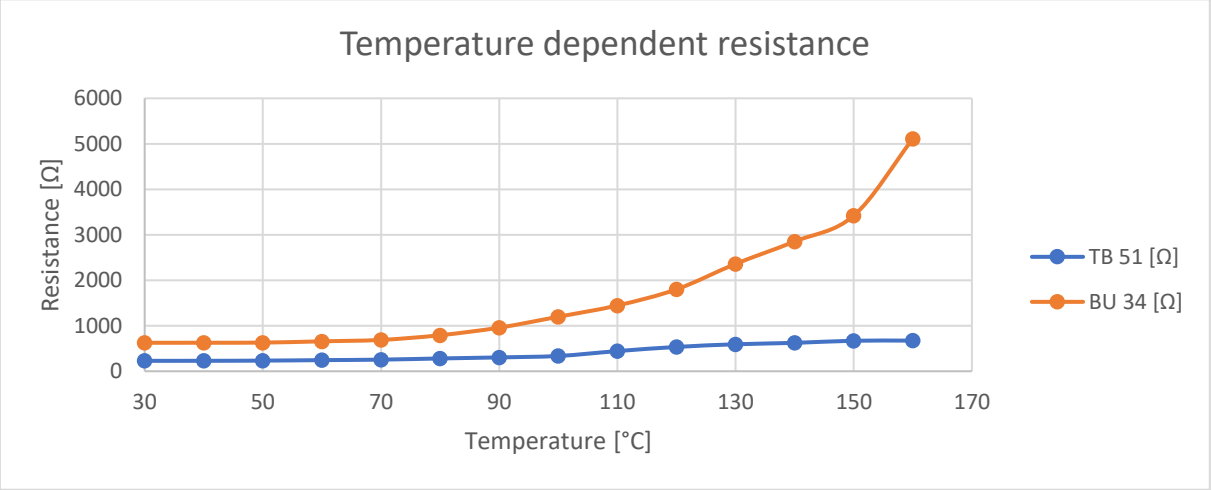

Graph 1 Temperature dependant resistance results for samples TB 51 and BU 34

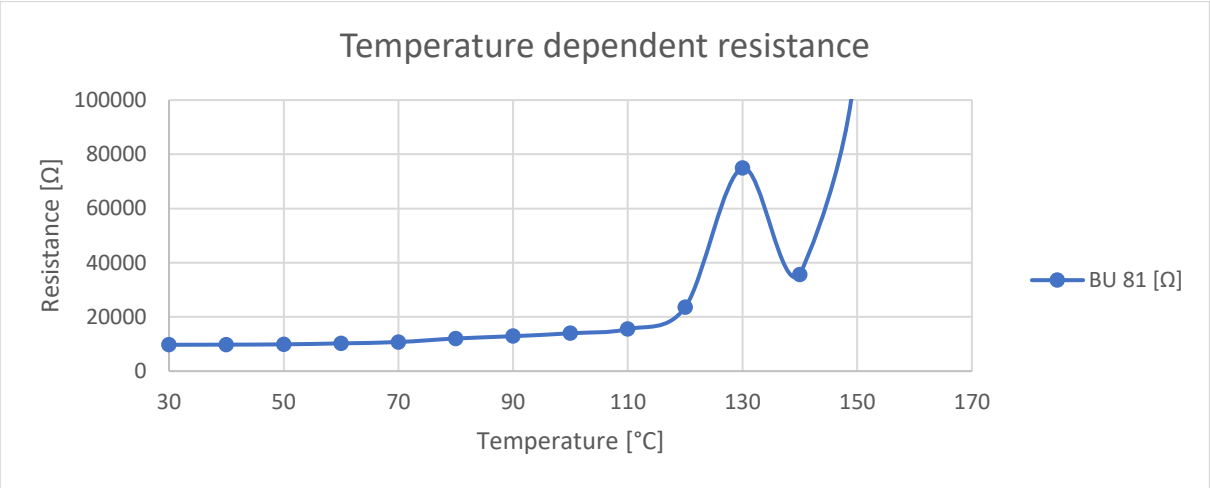

Graph 2 Temperature dependant resistance results for sample BU 81

In Graph 2 on test sample BU 81, significant irregularity can be seen between temperatures 130 and 150. The resistance value for temperature 140 °C is lower than it should be. That is because the measuring device could not deliver any steady value in these high temperatures. From temperature 130 °C, this problem occurred for sample BU 81. Due to this problem, the experiment should be repeated, but because of the circumstances related to Covid 19 pandemic, the experiment could not be performed again in time. Mostly shown value on the display of the measuring device were always chosen after this temperature. Although any accurate value could be measured, it is clear that the resistance continues to grow with temperature even after the 130 °C marks.

5.4.2 Heating up due to flow of electrical current

In this measurement, the temperature profile of the OCP during applied voltage and current has been investigated. An infrared camera was used to measure the temperature. The current was introduced thanks to the applied voltage on the copper straps. Copper straps are the same as in the previous measurement. Starting applied voltage was 50V, ending voltage was 250V, and measurements were done in 50V steps. Whenever some voltage has been applied, measurement was taken one minute after, so the temperature could stabilise on steady value. In Figure 43, the layout of the pictures shown below can be seen. It shows the

electrodes' position, copper straps, lines for measuring temperatures along the X and Y axis used to draw graphs below. These lines slightly differ in some photos because they were arranged every time to get as much relevant data as possible.

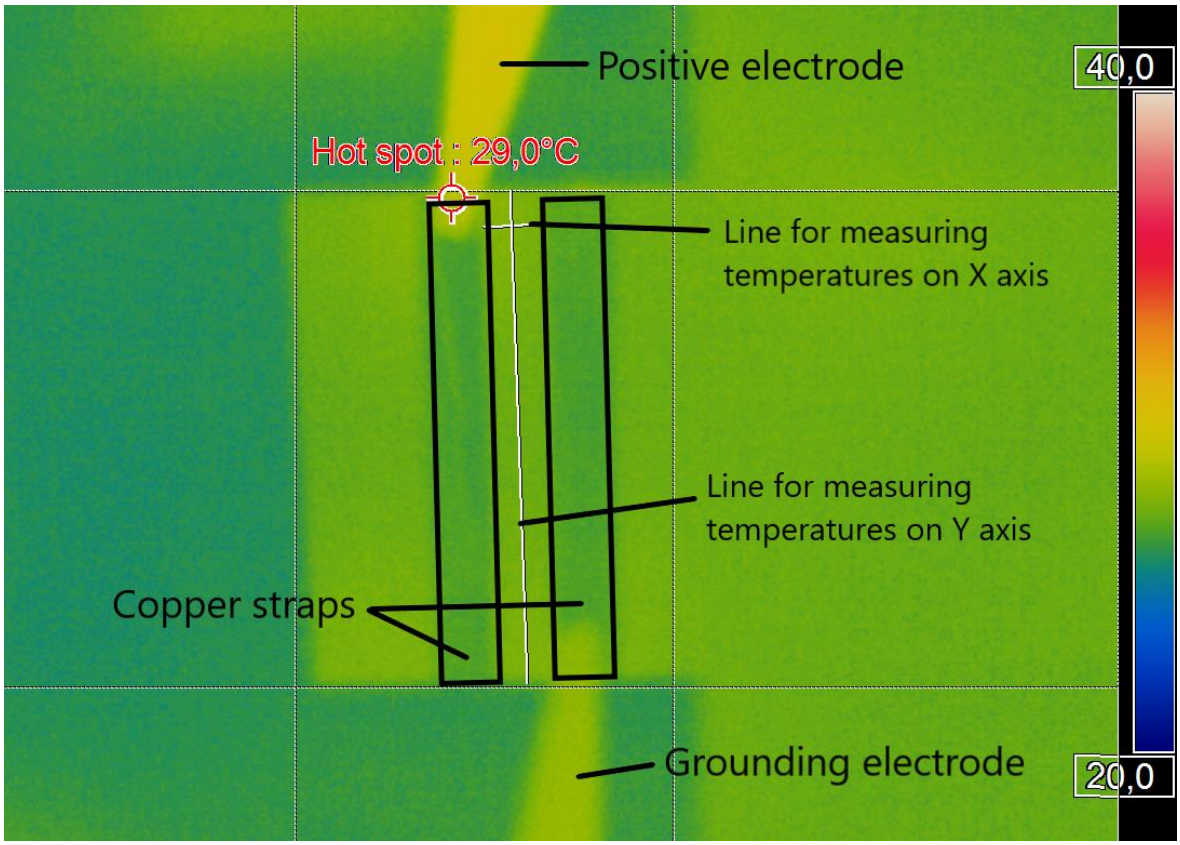

Figure 43 Layout of the photos

5.4.2.1 Infrared camera results

In this chapter, infrared camera results are shown. Due to the enormous number of photos, only some sample photos and graphs are shown. The rest of the results are in thesis attachments.

Firstly, only one scale is used for every sample, so it would be easier to see the temperature difference. Photos with accurate scales are also shown to see better temperature difference in the area and graphs of X and Y axes temperatures. Sample TB 51 could be measured only to 150V because after exposing it to this voltage, it almost caught fire, and

the experiment had to be ended. However, this happened due to a significant thermal overstressing of the OCP designed for Class 155 °C.

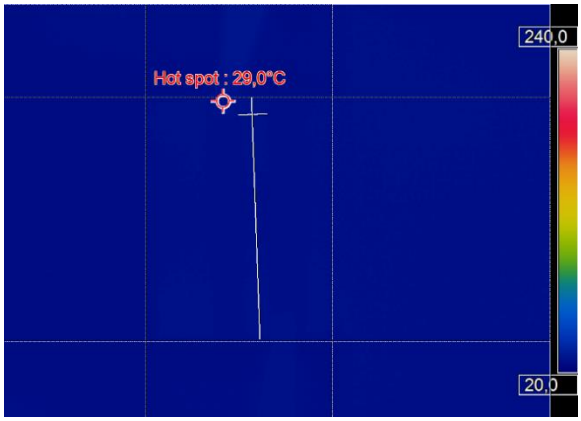

Figure 44 BU 34 50V (one scale)

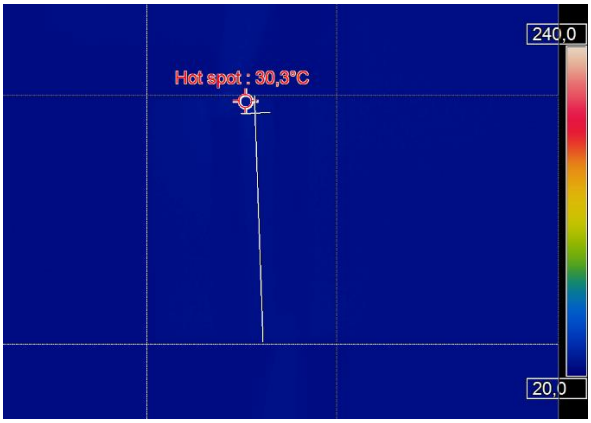

Figure 45 BU 34 100V (one scale)

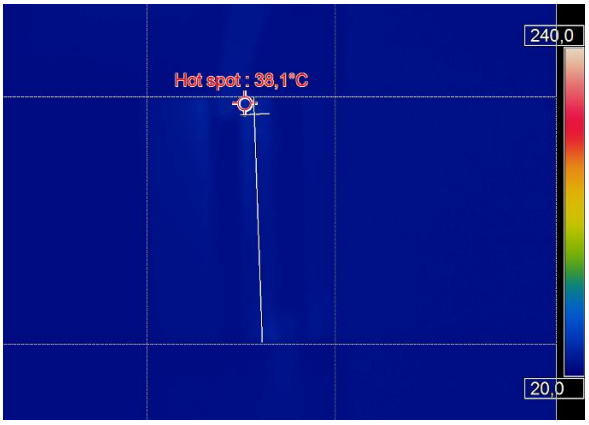

Figure 46 BU 34 150V (one scale)

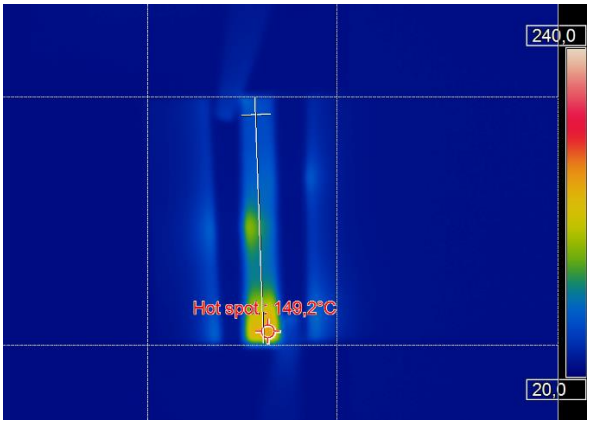

Figure 47 BU 34 200V (one scale)

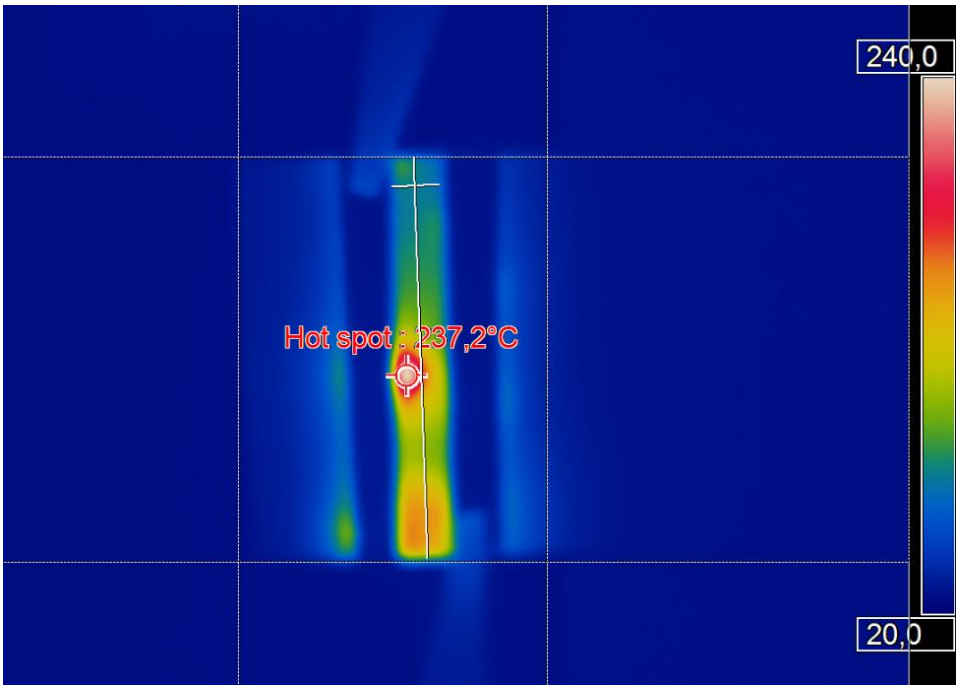

Figure 48 BU 34 250V (one scale)

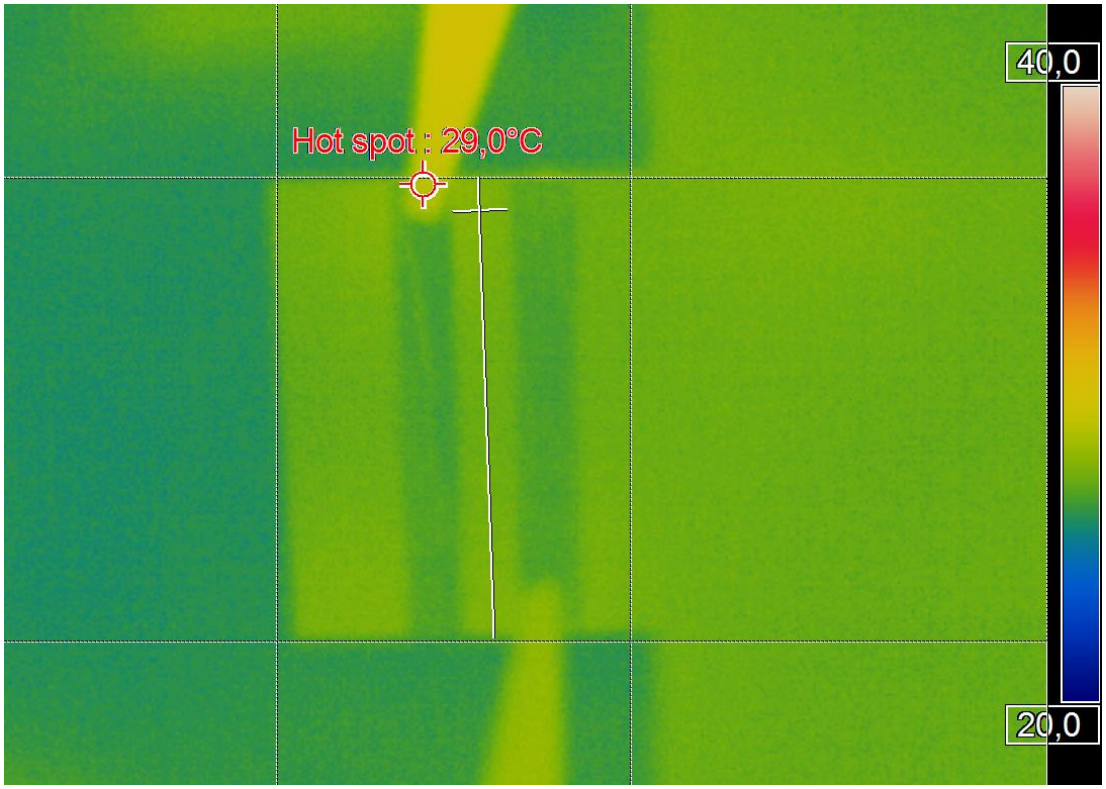

Figure 49 BU 34 50V (multiple scales)

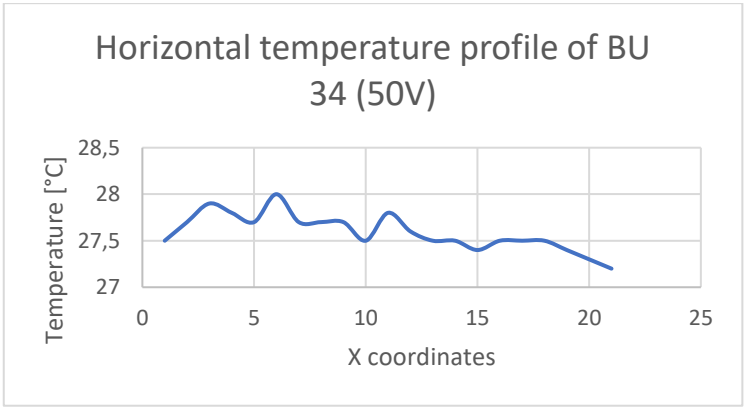

Graph 3 BU 34 50V X coordinates

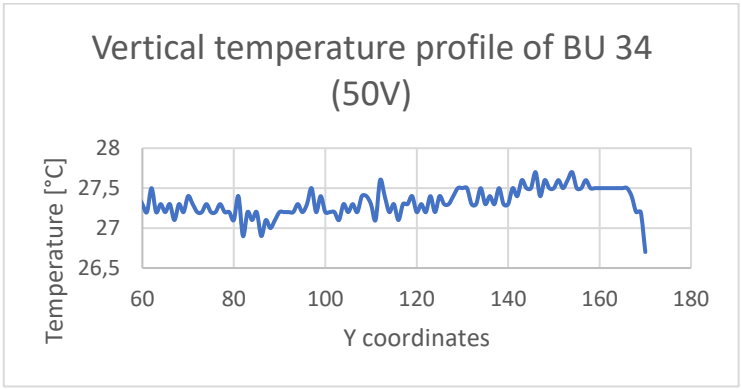

Graph 4 BU 34 50V Y coordinates

5.4.2.2 Additional observations

When measuring with the infrared camera, two of the samples almost caught fire. Sample TB 51 almost caught fire when exposed to 150V. Sample BU 34 almost caught fire when exposed to 250V. Both samples were emitting significant amounts of smoke. However, this happened due to a significant thermal overstressing of the OCP designed for Class 155 °C. With sample TB 51, even one minute of waiting time for the temperature to settle on a stable value could not be done because its temperature rose fast after seconds, and it did not seem to stop. Hence, the test had to be terminated prematurely because of safety reasons. Although sample BU 34 could be adequately measured even for one minute, but with increased caution. Its temperature settled around 235 °C after few seconds, and it did not rise much further. This phenomenon occurred most likely due to some local irregularities or defects in samples. Actual places of these occurrences can be seen in Figure 50 and Figure 51. On sample BU 34, the spot could be seen after measurement with the naked eye without any problem. Spot occurred damaged compared to the rest of the sample, but this did not apply for sample TB 51. After measurement, no visible damages could be seen.

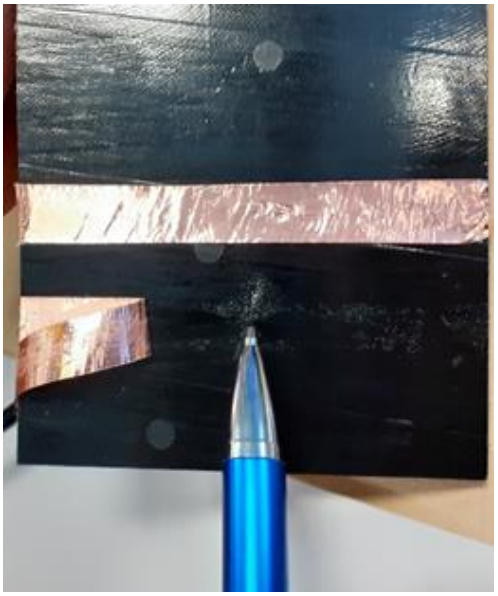

Figure 50 Place where sample BU 34 almost caught fire

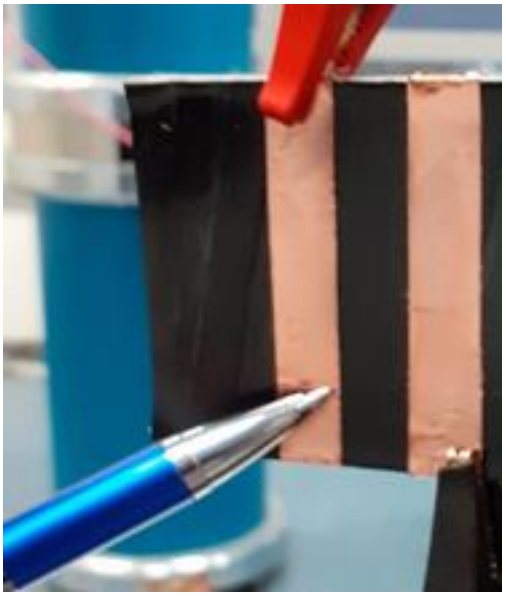

Figure 51 Place where sample TB 51 almost caught fire

Measurement of leakage also took place during the second measurement. Its results, along with temperatures of hot spots, can be seen in Table 27.

Table 27 Overview of leakages and hot spots during the whole measurement

	50 V	100 V	150 V	200 V	250 V
TB 51 hot spot [°C]	28,3	32,1	274,9		
TB 51 leakage [mA]	4,42	4,73			
BU 81 hot spot [°C]	28,1	28,9	40,2	75,6	70,4
BU 81 leakage [mA]	2,49	6,56	7,43	7,68	7,98
BU 34 hot spot [°C]	29	30,3	38,1	149,2	237,2
BU 34 leakage [mA]	3,81	6,46	8,07	7,63	

Leakage value was measured with a voltmeter connected, as displayed in Figure 52. The final value of leakage in mA was calculated from equation (25). In Table 27, some values of leakage are missing. Values for sample TB 51 are missing because the sample itself almost caught fire due to extreme thermal overstress of the OCP, and the last value could not be read to prevent a laboratory accident. For the last value of sample BU 34 same reasoning applies. After one minute of delay for the temperature to stabilise, smoke coming out of the sample was seen, and the voltage source had to be shut down. Hence the last value of leakage could not be read.

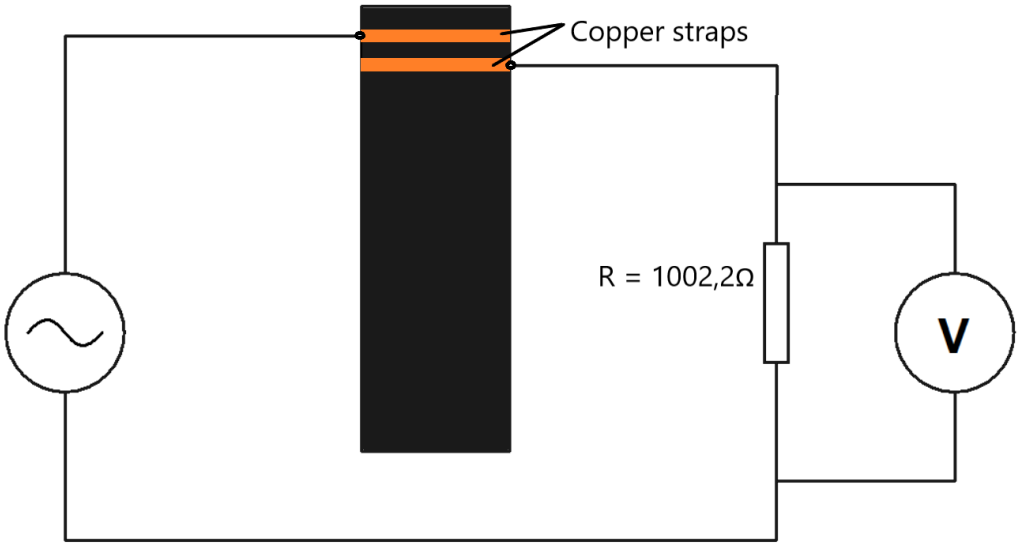

Figure 52 Wiring diagram used to measure leakage values

$$I = \frac{U}{R} \tag{25}$$

Conclusion

This thesis provides an overview of partial discharges and ways of decreasing their influence on the lifetime of electrical rotating machines using semi-conductive tapes. Partial discharges have several negative effects on the insulation of stator bars. These effects are chemical, thermal, electro-erosive, and together, they may shorten the lifetime of any rotating electrical machine. However, it has to be mentioned in this context that partial discharges within a mica based form wound insulation of high voltage stator windings are normal and system immanent. Depending on the location and the intensity of partial discharges they can have either no (respectively negligible) or significant impact regarding accelerated aging. Thus, it is necessary to understand the partial discharge phenomenon and ways how to minimize their occurrence. For this purpose, three different protection tapes are used – Outer Corona Protection (OCP), Inner Corona Protection (ICP) and End Corona Protection (ECP). Each kind of this tapes must be placed on a specific location on the stator bar. ICP must be placed on the stator bar to provide a steady connection between the stator bar and the bars insulation. ECP is placed on the part of the bar, on the insulation, where it exits the slot of the stator core, where it moderates the distribution of the electrical field to decrease partial discharge activity. OCPs place is on the insulation of the bars, in the slot part of the stator bar, where it functions as prevention of slot discharges and has to provide a steady connection between the insulation and stator core. The main attribute of OCP is its square resistance $R_{\square}$, which cannot be too high or too low in order to work as intended. Numerous research papers were published about finding optimal square resistance and finding a way to determine its optimal value. Still, because of the complexity of multiple

factors influencing the behaviour of the insulation and semi-conductive protections, there is not an easy way how to determine the optimal solution for optimal square resistance of OCP.

As part of this thesis, several experiments were performed to describe the properties of OCP tapes. There were two sets of specimens, fully cured OCP samples and raw OCP tapes, both provided by well-known tape manufacturers. Surface resistance was measured on the fully cured OCP together with fully cured main insulation (sample – piece of insulation cut out from a new stator bar) with two different kinds of probes and copper straps. With these measured values, it was then possible to calculate the square resistance. Along with the surface resistance, there was also a measurement to describe the volume resistivity of one sample from the fully cured samples (main unsulation with OCP) set, followed by measurement of the temperature dependence of resistivity of said samples. During the surface resistance experiments, several imperfections occurred. One of the samples showed tricky values of resistance. There was a plan to repeat this experiment, but the Covid-19 pandemic situation did not allow this to happen. The fully cured OCP samples were also examined with an infrared camera to discover how the specimens will heat up if they were exposed to electrical current. The second set of samples, the raw OCP tapes, were examined under the electron microscope. There was an EDXA analysis performed on them to understand the composition of OCP materials better.

References

[1] Kokoška, Martin. *Protikoronové ochrany velkých točivých strojů.* Pilsen, 2018. Diploma thesis. University of West Bohemia in Pilsen. Thesis supervisor Ing. Josef Pihera, Phd.

[2] KRPAL, Ondřej. *Nové přístupy k optimalizaci polovodivých ochran*1. Pilsen, 2014. Dissertation thesis, University of West Bohemia in Pilsen. Thesis supervisor doc. Ing. Eva Kučerová, CSc.

[3] ZÁLIŠ, Karel. *Částečné výboje v izolačních systémech elektrických strojů.* Prague: Academia, 2005. 135 s. ISBN 80-200-1358-X.

[4] WOHLRÁB, Robin. *Způsoby minimalizace částečných výbojů u vinutí točivých strojů.* Pilsen, 2013. Bachelor thesis. University of West Bohemia in Pilsen. Thesis supervisor Ing. Ondřej Krpal.

[5] VEVERKA, Antonín. *Technika vysokého napětí.* Prague: SNTL -Nakladatelství technické literatury, 1978. 04-512-78.

[6] LIESE Manfred, BROWN Martin. *Design-dependent slot discharge and vibration sparking on high voltage windings*, IEEE DEI, Vol. 14, No. 4, pp. 927-932, 2008

[7] JACKSON RJ, WILSON A., *Slot-discharge activity in air-cooled motors and generators*, IEE Proc, Vol. 129, Pt. B, No. 3, pp. 159-167, 1982.

[8] THIENPONT J., SIE T. H., *Suppression of surface discharges in the stator windings of high voltage machines*, Cigré Paper 122, 1964.

[9] WALLASH A., LEVIT L., *Electrical Breakdown and ESD Phenomena for Devices with Nanometer-to-Micron Gaps*, Maxtor Corporation, http://www.wallash.com/spiep.pdf.

[10] A. Litinsky, G. Schmidt, F. Pohlmann and H. Hirsch, "*Analysis of resistance characteristics of multilayered field grading material structures on rotating machines*," 2016 IEEE International Conference on Dielectrics (ICD), Montpellier, France, 2016, pp. 426-430, doi: 10.1109/ICD.2016.7547634.

[11] A. Staubach, G. Schmidt, F. Pohlmann and H. Hirsch, "*Investigation of Ideal Anisotropic Material Properties for Outer Corona Protection Systems in Large Rotating Machines*," 2018 IEEE Electrical Insulation Conference (EIC), San Antonio, TX, USA, 2018, pp. 365-368, doi: 10.1109/EIC.2018.8481019.

[12] A. Litinsky, G. Schmidt, F. Pohlmann and H. Hirsch, "*Advanced Assessment of Outer Corona Protection Material Durability*," 2018 IEEE Electrical Insulation Conference (EIC), San Antonio, TX, USA, 2018, pp. 538-541, doi: 10.1109/EIC.2018.8481083.

[13] A. Litinsky, G. Schmidt, F. Pohlmann and H. Hirsch, "*Ageing of corona protection material on rotating machines*," 2017 IEEE Electrical Insulation Conference (EIC), 2017, pp. 356-359, doi: 10.1109/EIC.2017.8004679

[14] R. Schmerling, F. Jenau, C. Staubach and F. Pohlmann, "*Investigations of modified nonlinear electrical materials for end corona protection in large rotating machines*," 2012 47th International Universities Power Engineering Conference (UPEC), 2012, pp. 1-5, doi: 10.1109/UPEC.2012.6398563.

[15] S. Kempen, S. Lang, F. Pohlmann; *New grading material enables optimized design of end corona protection for large rotating machines*, ISH 2011, Hannover

[16] Guido Schmidt, Franklin Emery and Henning Niels Kölnberger, *MODELLING OF OUTER CORONA PROTECTION SYSTEMS OF LARGE ROTATING MACHINES USING FINITE ELEMENT METHOD*, Siemens AG, Muelheim an der Ruhr, Germany, Siemens Energy Inc., Charlotte NC; USA, accessible at http://vlabs.iitkgp.ac.in/vhvlab/html/pages/CD/topics_a-h/F-084-SCH-F.pdf

[17] A. Wichmann, "*Two Decades of Experience and Progress in Epoxy Mica Insulation Systems for Large Rotating Machines*," in IEEE Transactions on Power Apparatus and Systems, vol. PAS-102, no. 1, pp. 74-82, Jan. 1983, doi: 10.1109/TPAS.1983.318000.

[18] G. Schmidt, A. Litinsky, A. Staubach, „*Enhanced calculation and dimensioning of outer corona protection systems in large rotating machines*“, International Symposium on High Voltage Engineering, 2015

[19] ARTBAUER, J. „*Izolanty a izolácie*“, nakladatelství ALFA, Bratislava, 1969.

[20] E. Sharifi, S. H. Jayaram and E. A. Cherney, "*Temperature and electric field dependence of stress grading on form-wound motor coils*," in IEEE Transactions on Dielectrics and Electrical Insulation, vol. 17, no. 1, pp. 264-270, February 2010, doi: 10.1109/TDEI.2010.5412026.

[21] MENTLÍK, Václav, et al. *Diagnostika elektrických zařízení.* Praha: BEN, 2008. 440 s. ISBN 978-80-7300-232-9.

[22] PETROV, G.N. *Elektrické stroje 2*. Academia, Praha, 1982. ISBN 21-055-82

[23] BARTO., V., ČERVENÝ, J., HRUŠKA, J., KOTLANOVÁ, A., SKALA, B. *Elektrické stroje*. Plzeň : Západočeská univerzita , 2006, 139 s. ISBN: 80-7043-444-9

[24] PETROVIČ KOPYLOV, Igor, et al. *Stavba elektrických strojů*. Praha: SNTL, 1988. 688 s.

[25] BRUTSCH, Rudolf; HILLMER, Thomas. *Corona Protection in Rotating High Voltage Machines.* Inductica. 2006, 1, s. 1-6.

[26] IEC 62631-3-1:2016. *Dielectric and resistive properties of solid insulating Materials*, International standard, 2016, 26 pages

[27] Stone, G.C., Wu, R.: *Examples of Stator Winding Insulation Deterioration in New Generators*. IEEE ICPADM, Harbin, China, 2009

[28] Pohlmann, F., Weidner, J.R., Schattauer, D., Richter, C.G.,: *Design and 25 Years Experience of Turbine Generators with Global VPI Stator Windings*. EPRI generator workshop, Rome, Italy, 2013

[29] M. Lévesque, C. Hudon and E. David, "*Insulation degradation analysis of stator bars subjected to slot partial discharges*," 2013 IEEE Electrical Insulation Conference (EIC), 2013, pp. 479-483, doi: 10.1109/EIC.2013.6554293.

[30] C. Staubach, S. Kempen, F. Pohlmann: “*Calculation of Electric Field Distribution and Temperature Profile of End Corona Protection Systems on Large Rotating Machines by Use of Finite Element Model*”, ISEI, San Diego, USA, 2010

[31] CIGRE brochure 522, *Generator Stator Winding Stress Grading Coating Problem*, 2013

[32] Stone, G.C., Culbert, I., Boulter E. A., Dhirani Hussein, *Electrical Insulation for Rotating Machines*, Wiley-IEEE Press, 2004, ISBN: 9780471682905

[33] "IEEE Guide for the Measurement of Partial Discharges in AC Electric Machinery," in IEEE Std 1434-2014 (Revision of IEEE Std 1434-2000) , vol., no., pp.1-89, 4 Dec. 2014, doi: 10.1109/IEEESTD.2014.6973042.

[34] VON ROLL. Data Sheet: *CoronaShield SC 217.21* [online]. [cit. 2014-10-17]. Aviable at z: http://www.sibel.bg/upl_doc/CoronaShield%20SC%20217.21-EN.pdf

List of Figures

List of Tables

List of Graphs

Attachments

Electron microscopy

This section of attachments shows all photos taken with an electron microscope of OCP tapes from well-known tape manufacturers.

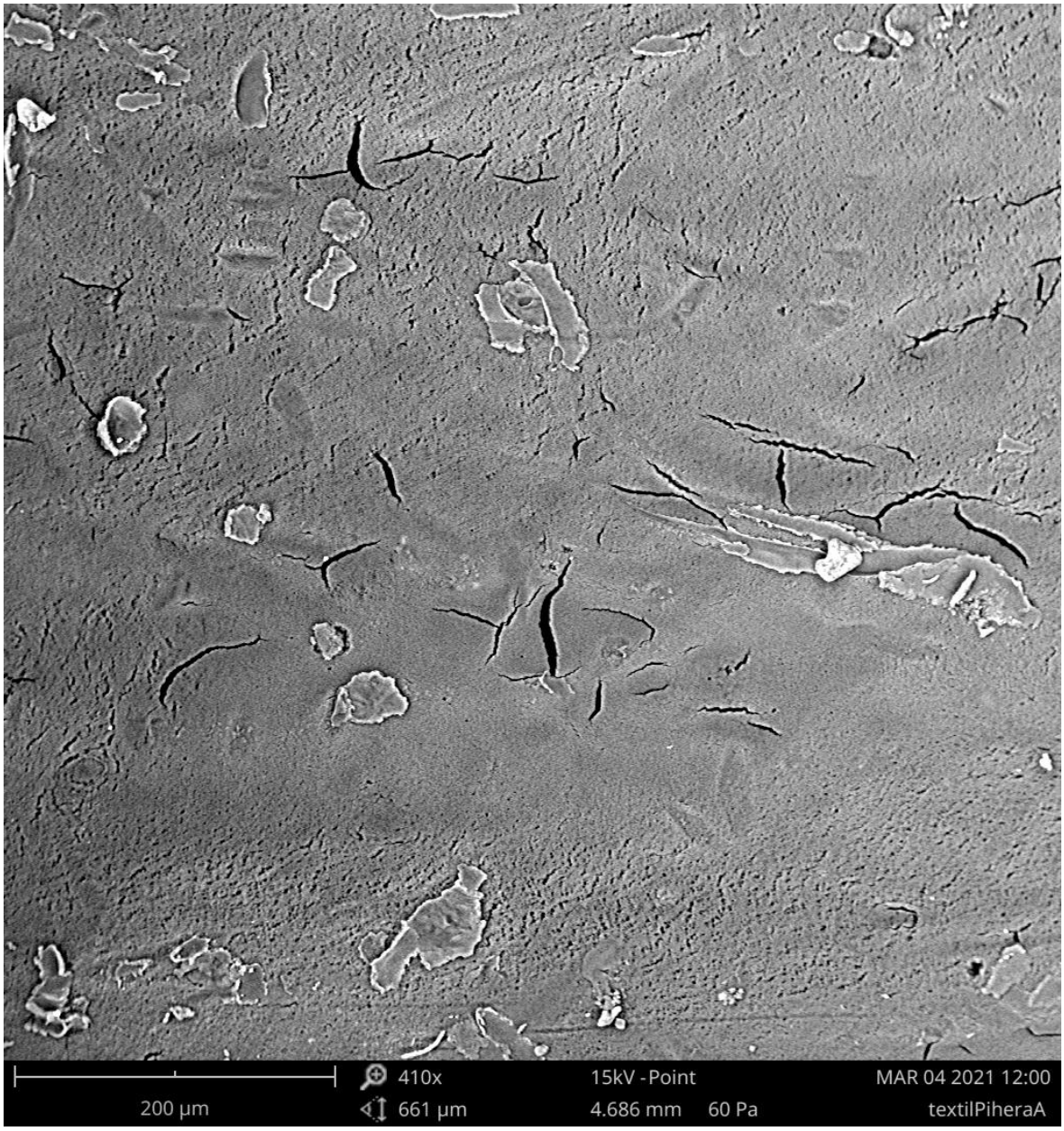

Photograph of tape Material A made using an electron microscope

Photograph of tape Material A made using an electron microscope

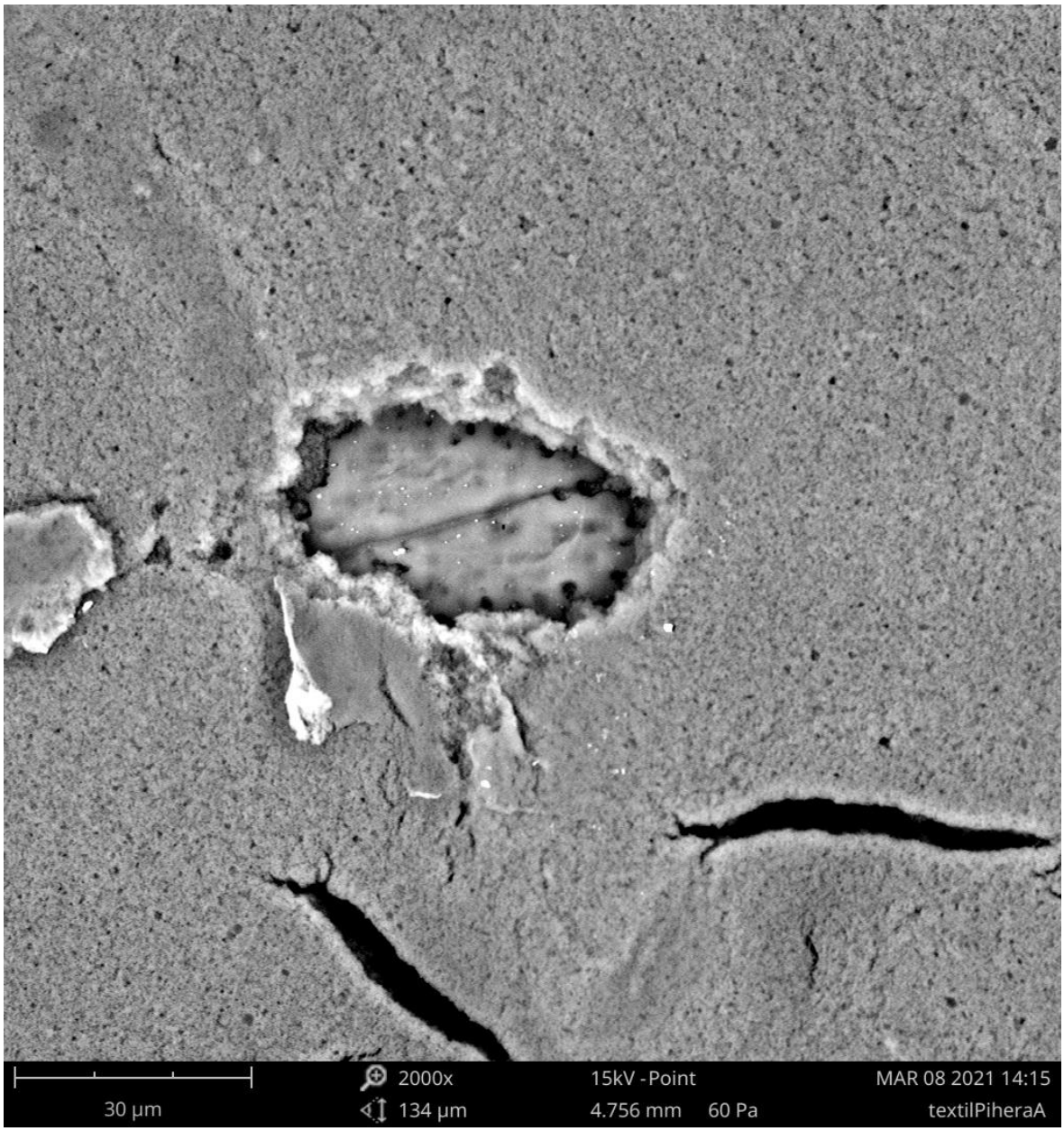

Photograph of tape Material A made using an electron microscope

Photograph of tape Material A made using an electron microscope

Photograph of tape Material A made using an electron microscope

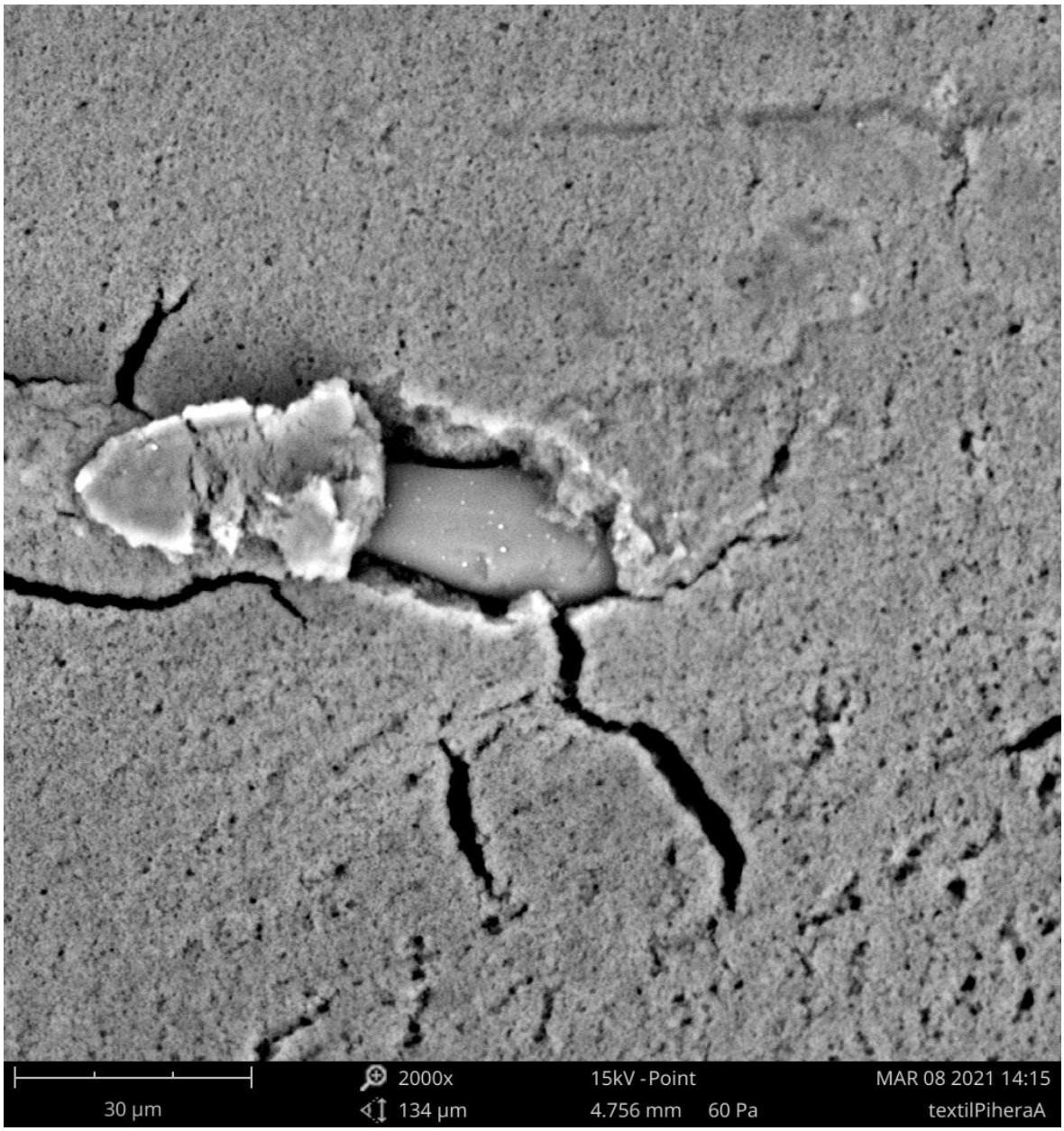

Photograph of tape Material A made using an electron microscope

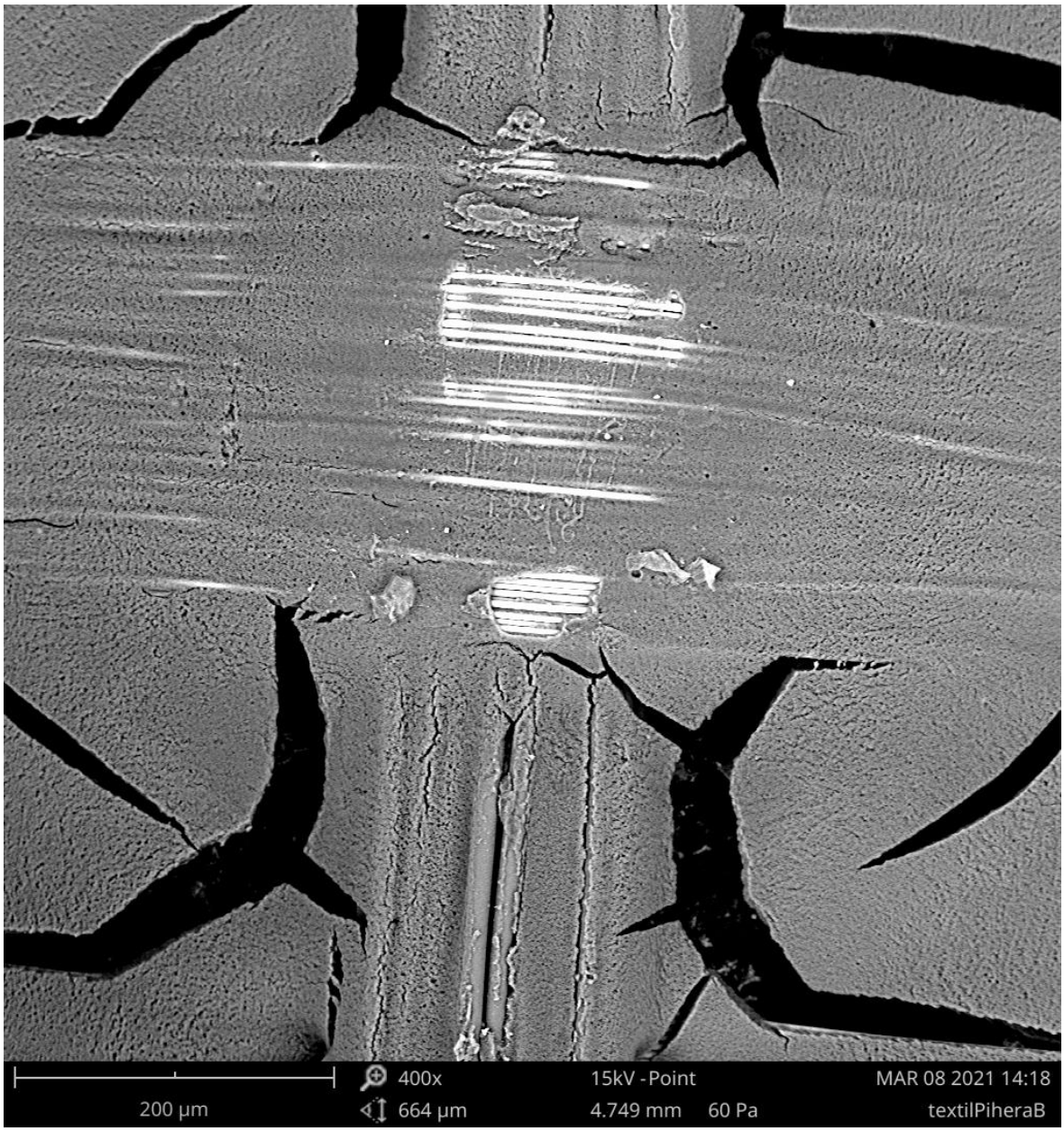

Photograph of tape Material B made using an electron microscope

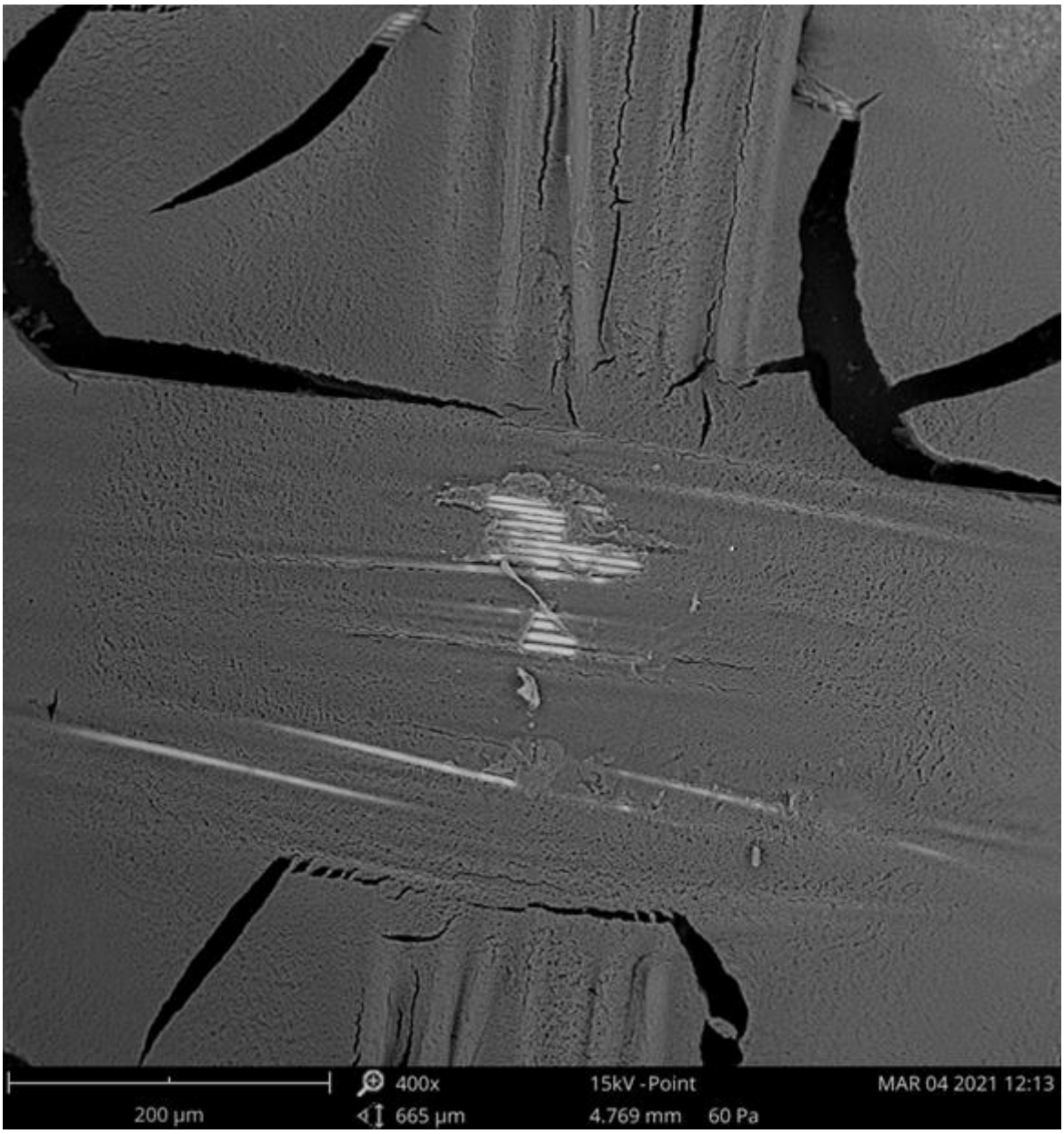

Photograph of tape Material B made using an electron microscope

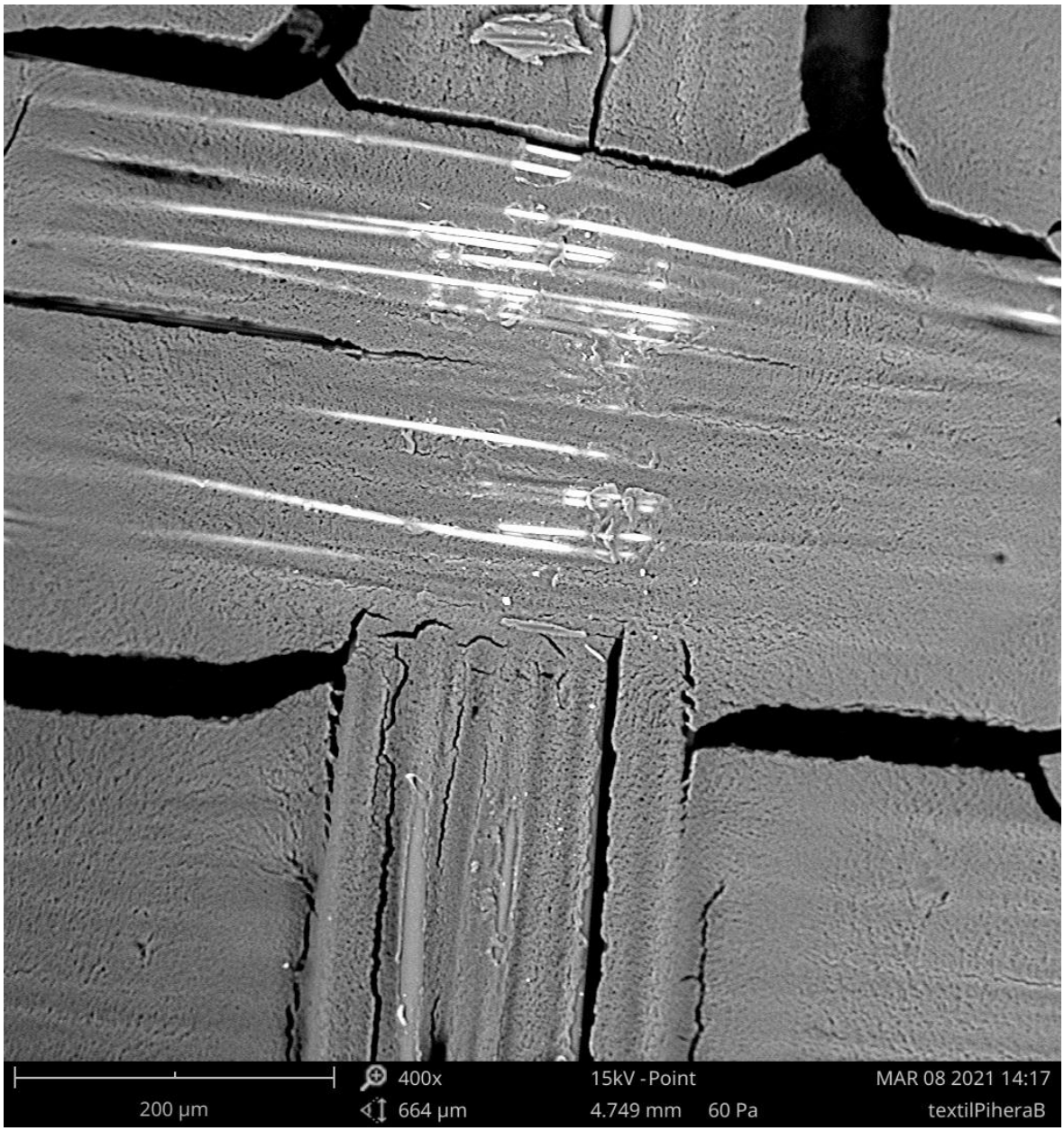

Photograph of tape Material B made using an electron microscope

Photograph of tape Material B made using an electron microscope

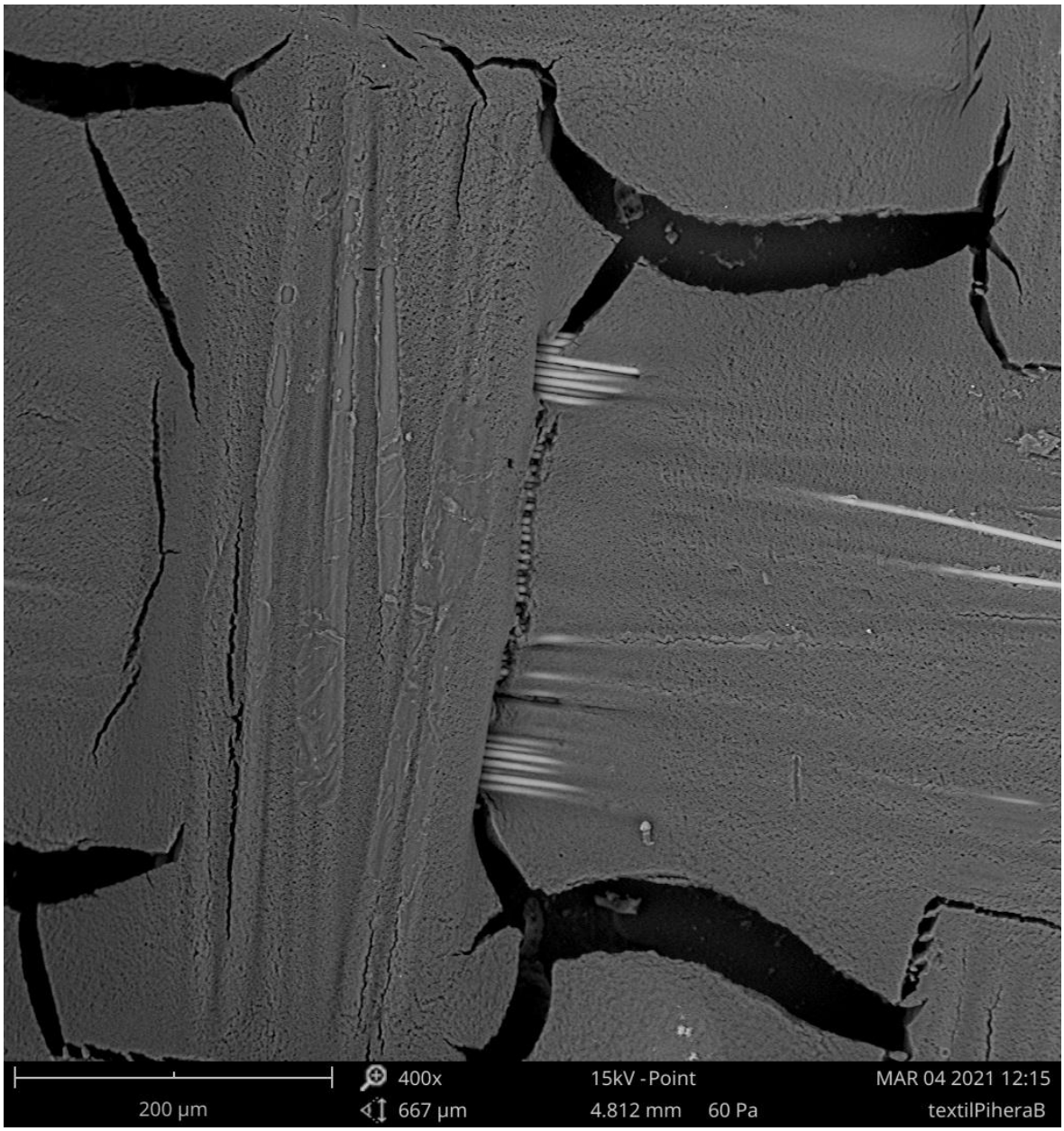

Photograph of tape Material B made using an electron microscope

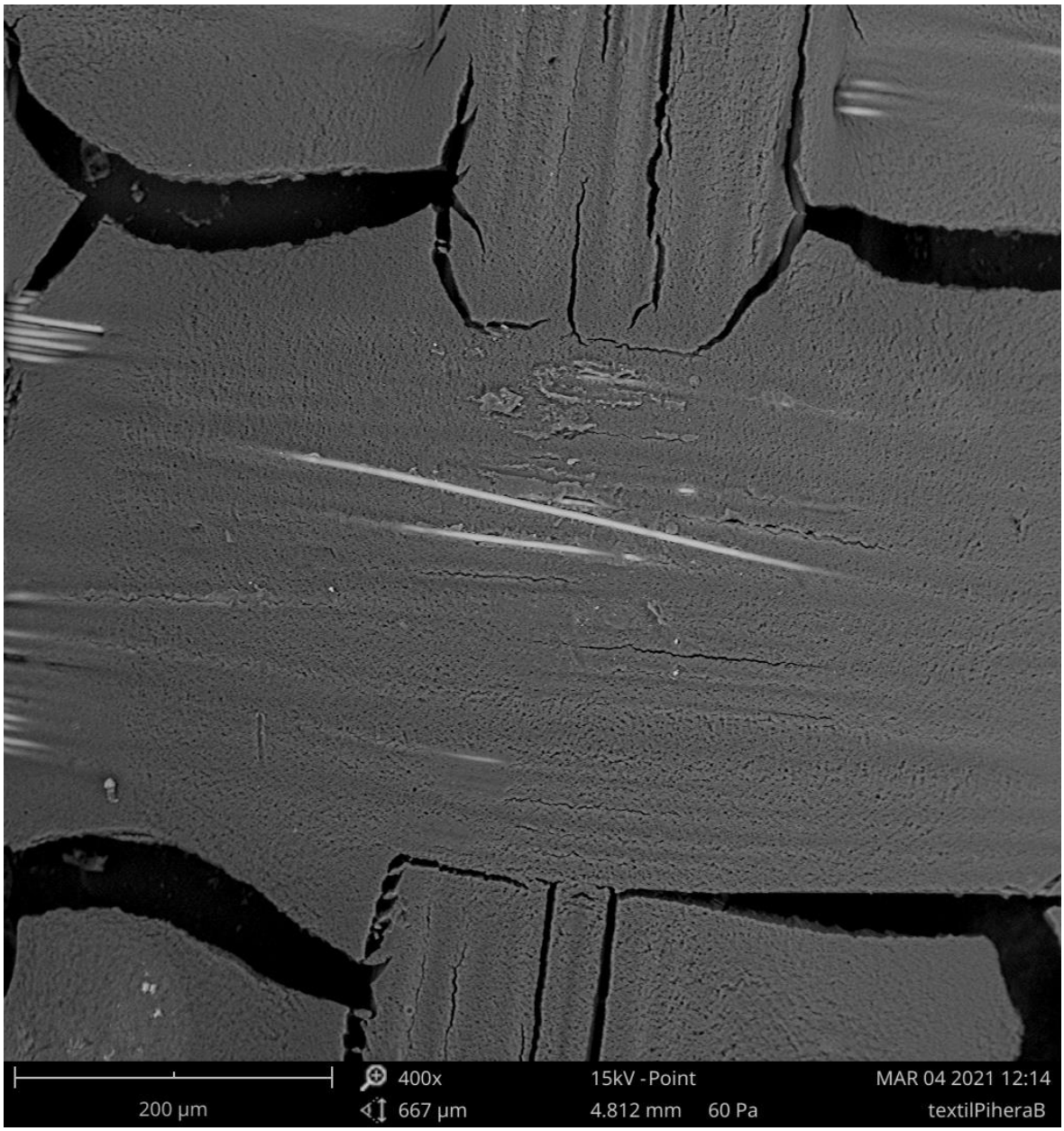

Photograph of tape Material B made using an electron microscope

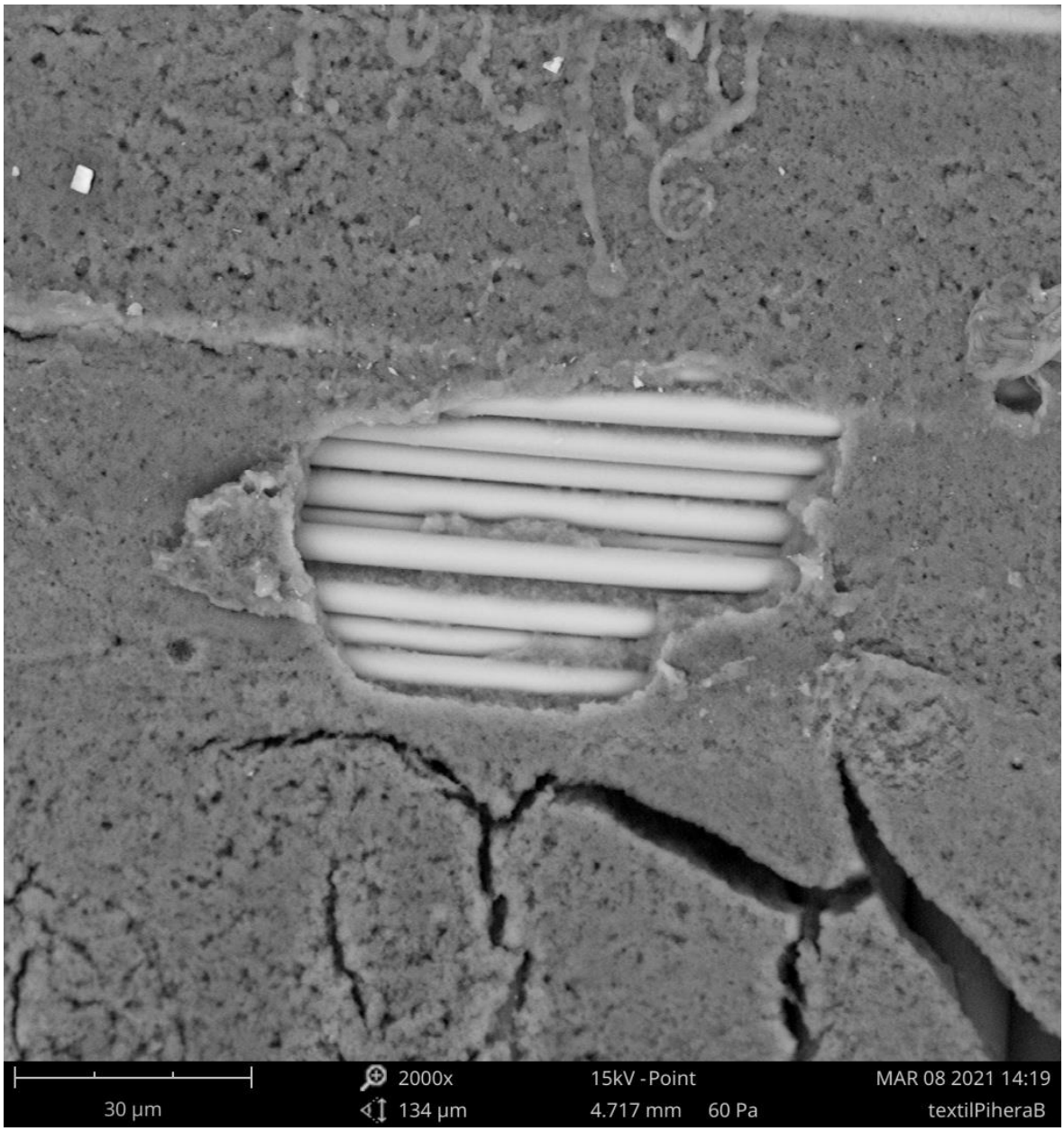

Photograph of tape Material B made using an electron microscope

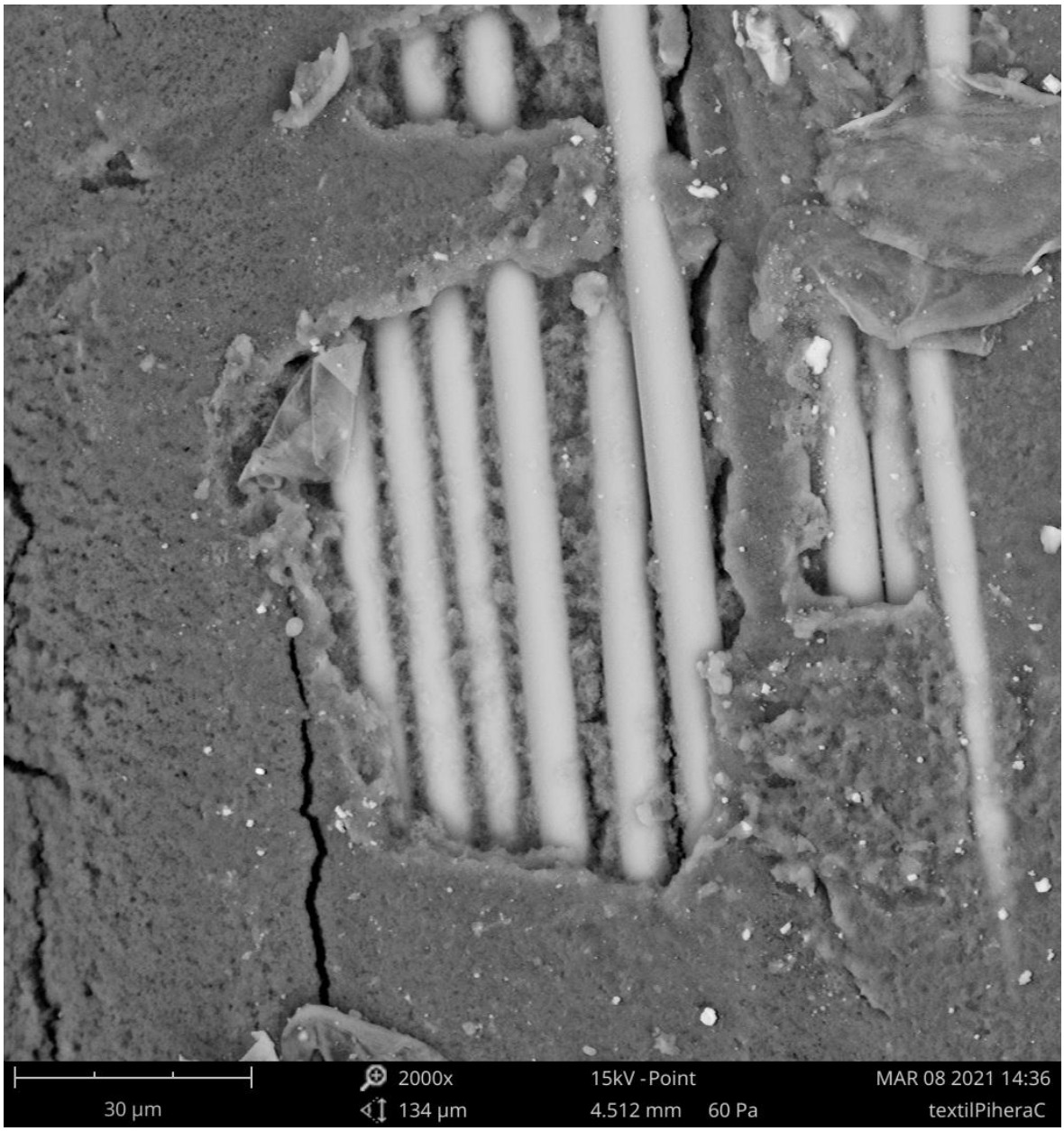

Photograph of tape Material C made using an electron microscope

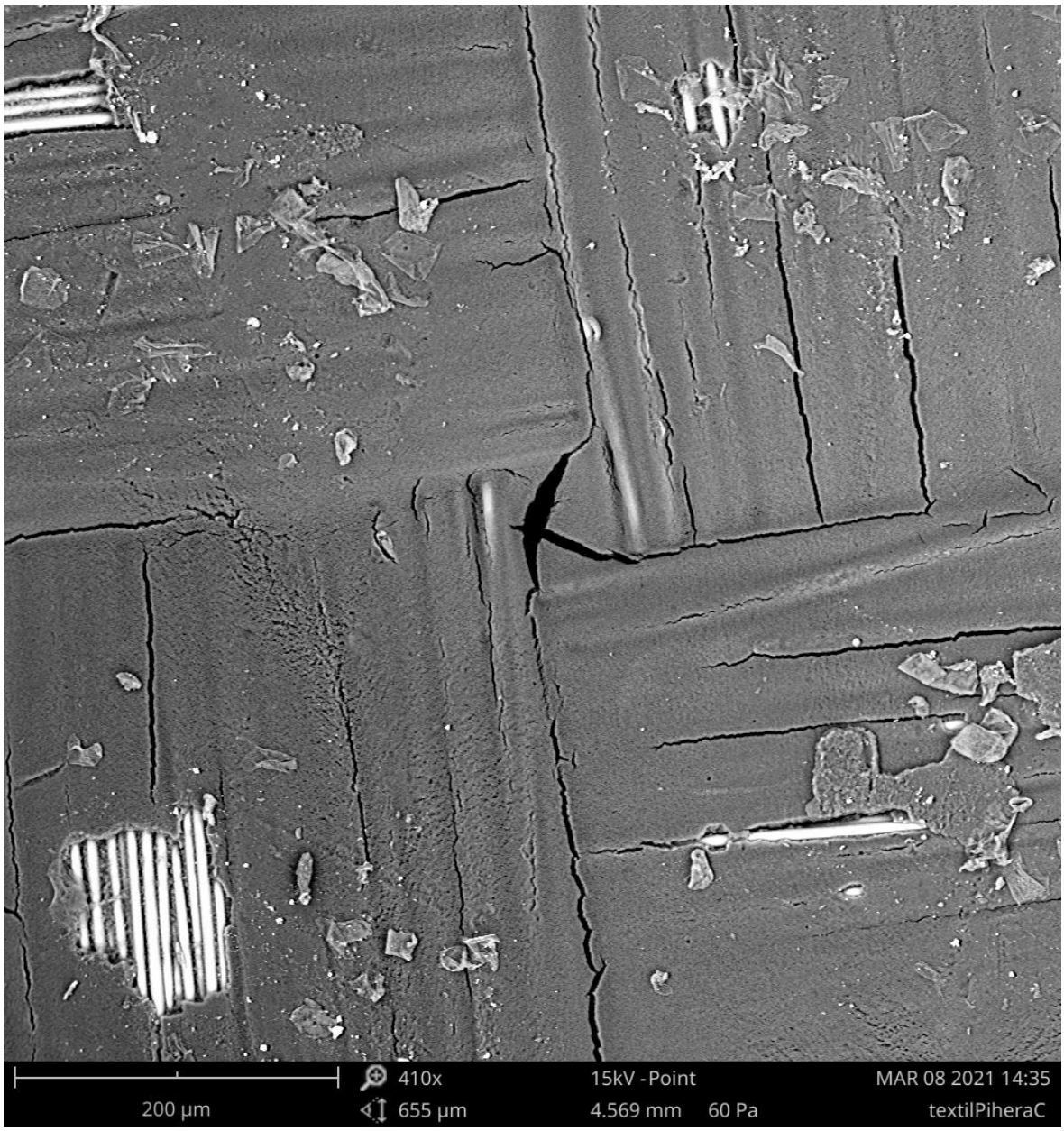

Photograph of tape Material C made using an electron microscope

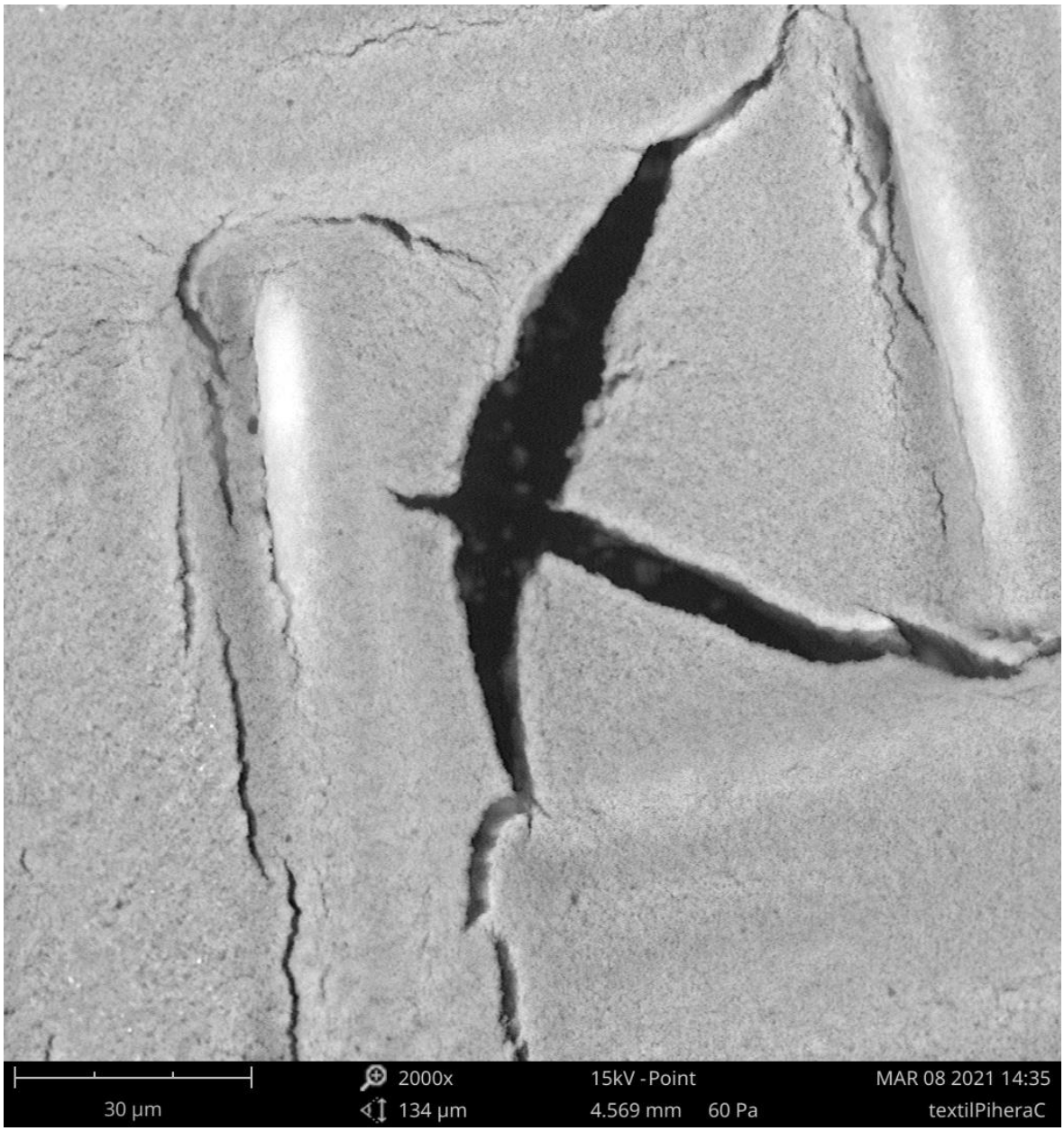

Photograph of tape Material C made using an electron microscope

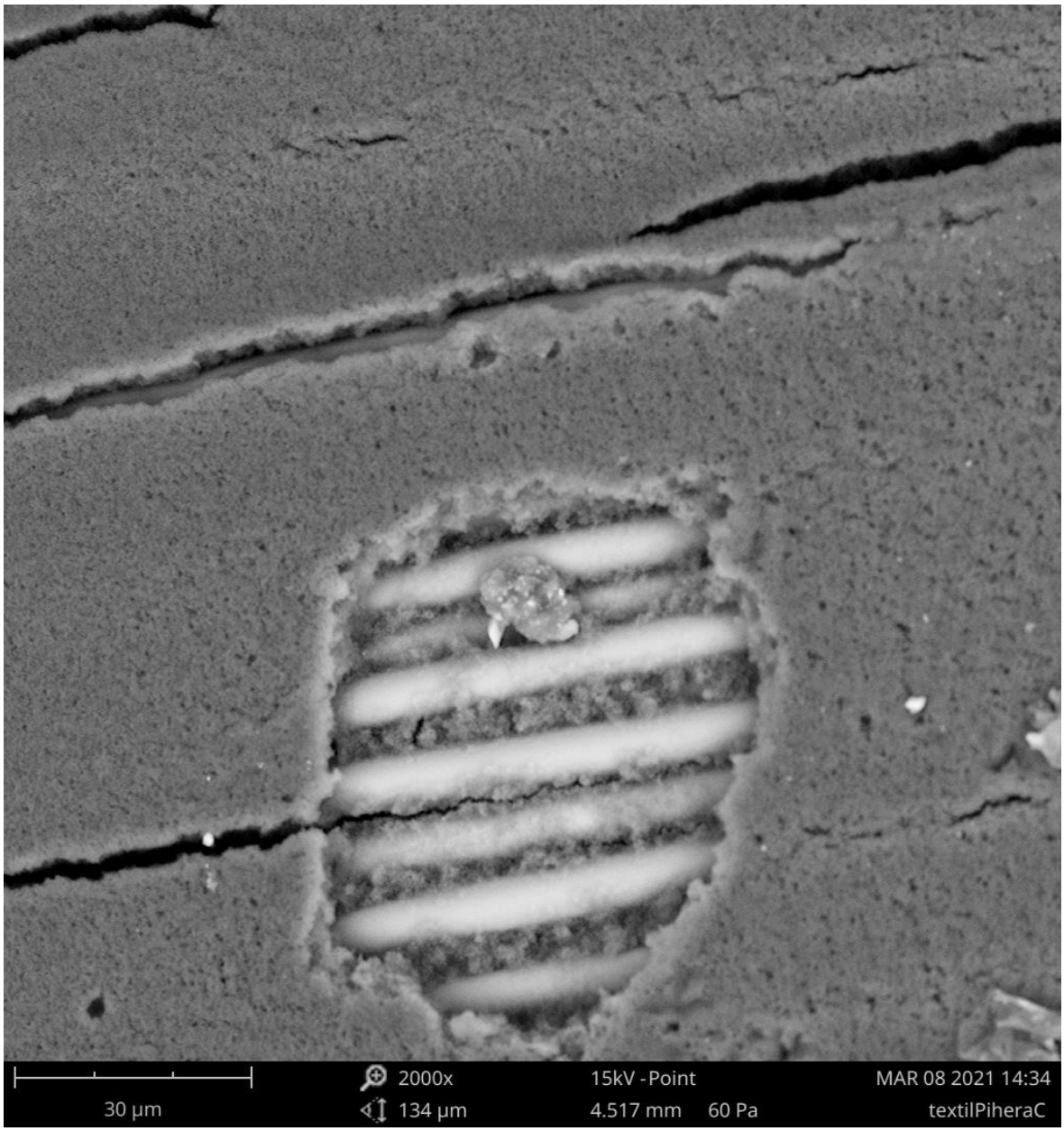

Photograph of tape Material C made using an electron microscope

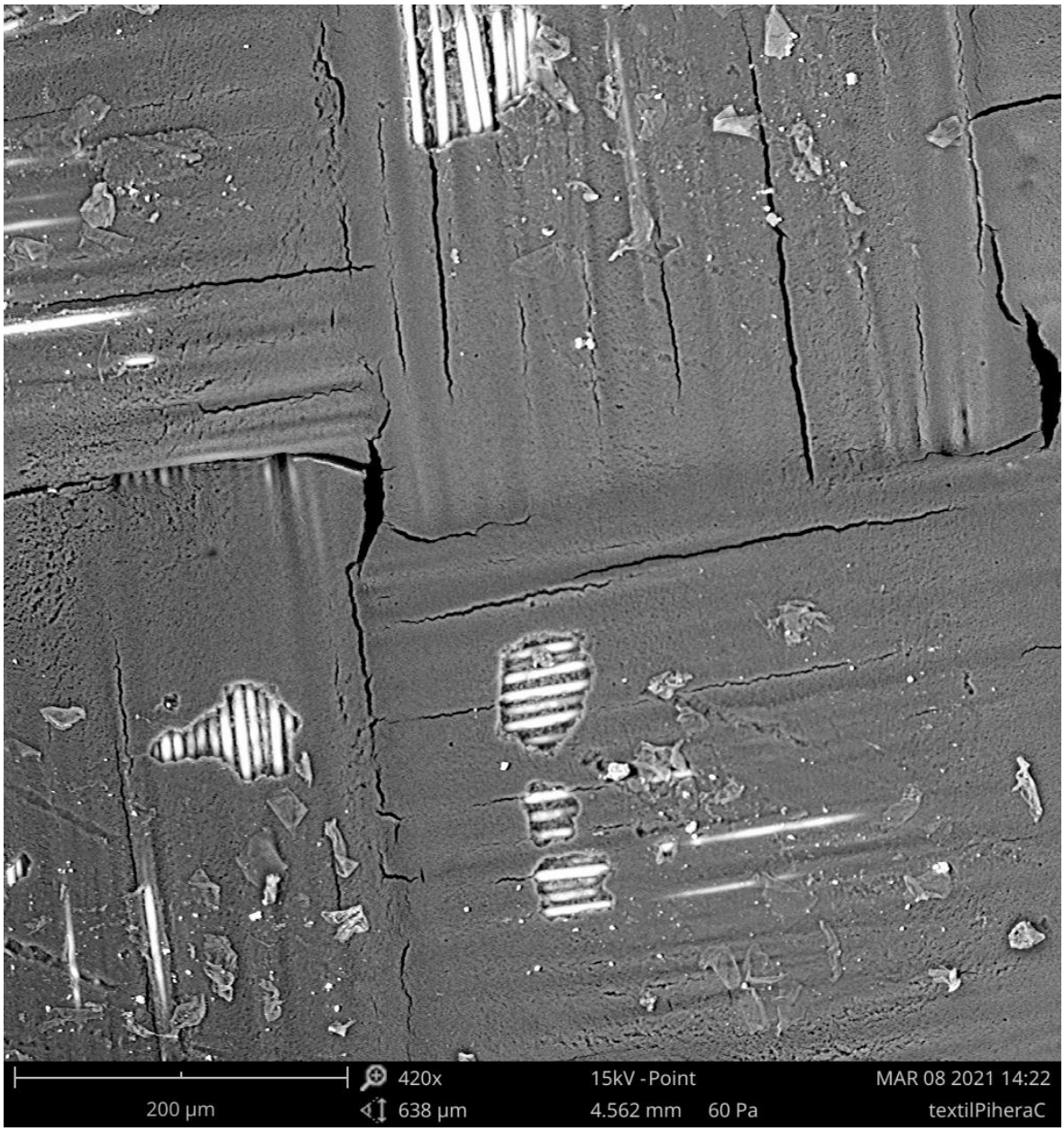

Photograph of tape Material C made using an electron microscope

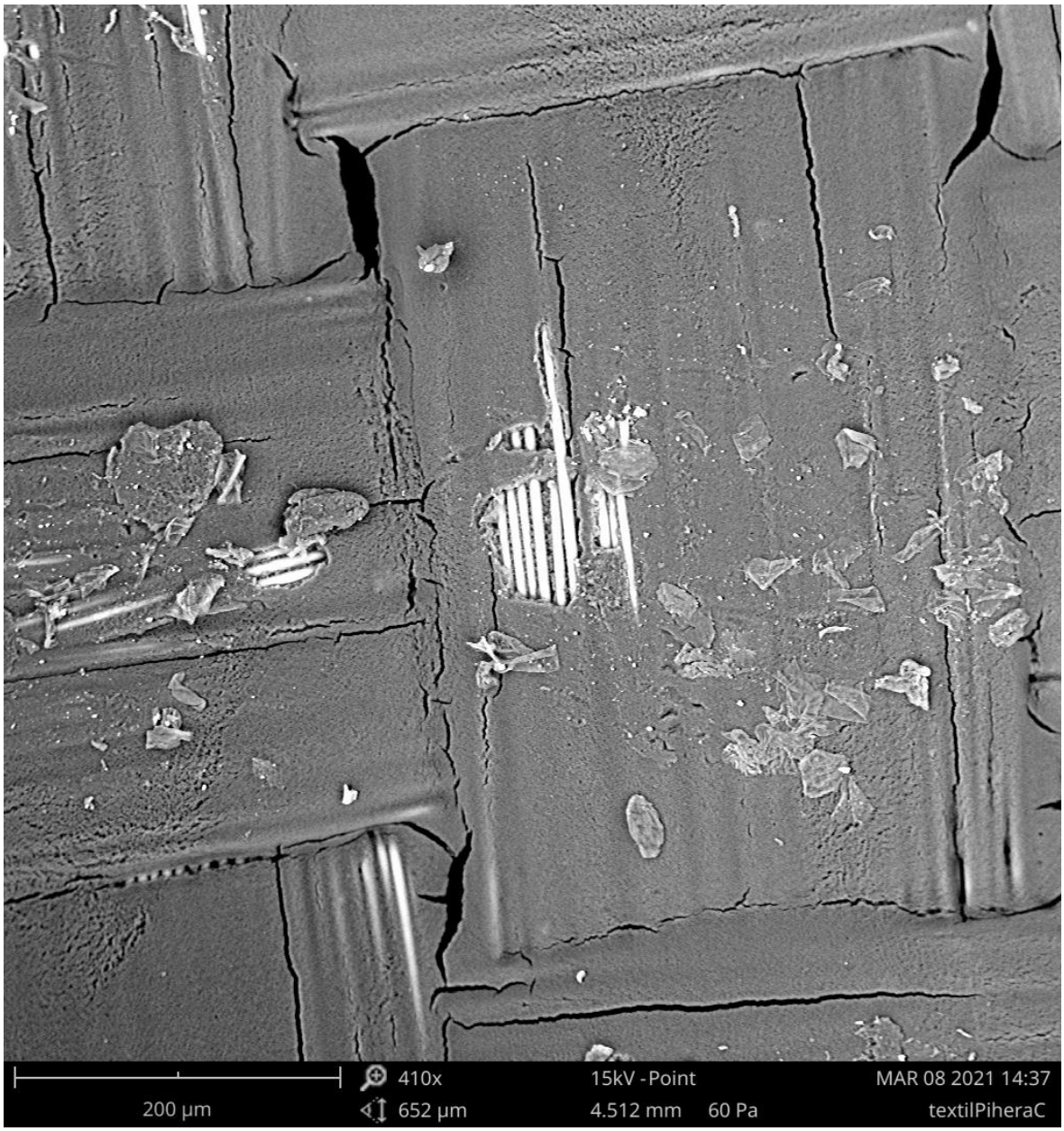

Photograph of tape Material C made using an electron microscope

EXDA analysis

In this section of attachments, a full report of EXDA analysis is shown.

Material A point analysis

1. spot

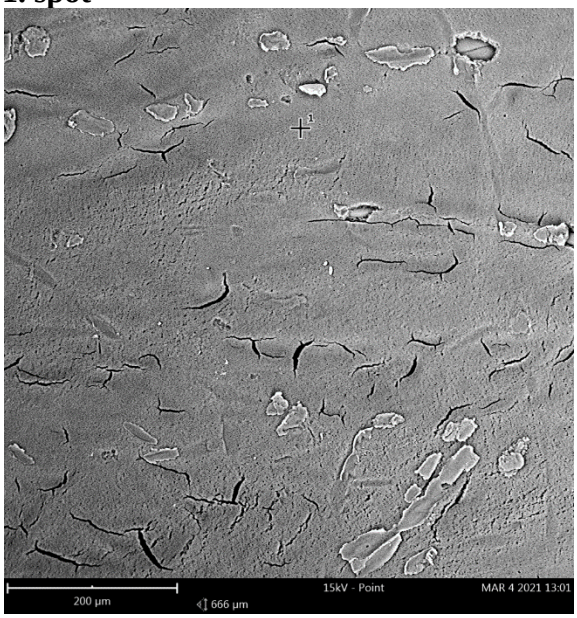

Element Number	Element Symbol	Element Name	Atomic Conc.	Weight Conc.
6	C	Carbon	100.00	100.00

FOV: 666 µm, Mode: 15kV - Point, Detector: BSD Full, Time: MAR 4 2021 13:01

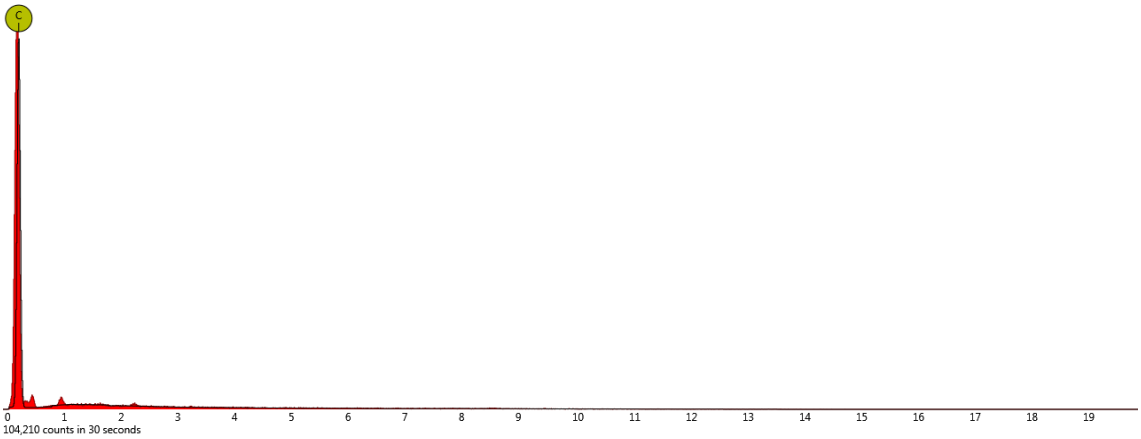

Disabled elements: B

2. spot

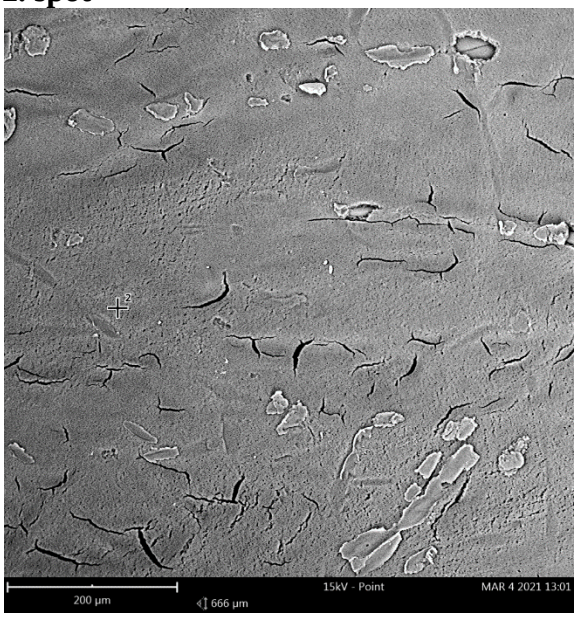

Element Number	Element Symbol	Element Name	Atomic Conc.	Weight Conc.
6	C	Carbon	100.00	100.00

FOV: 666 µm, Mode: 15kV - Point, Detector: BSD Full, Time: MAR 4 2021 13:01

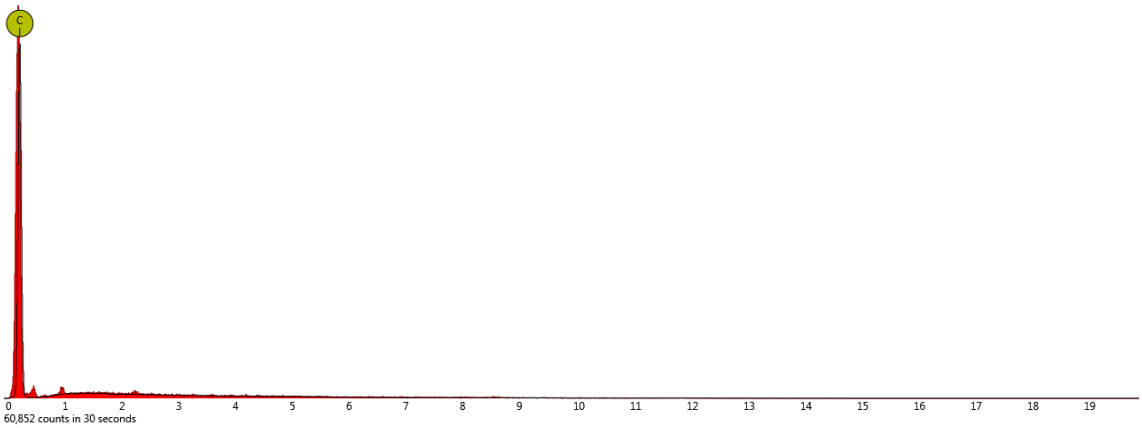

Disabled elements: B

3. spot

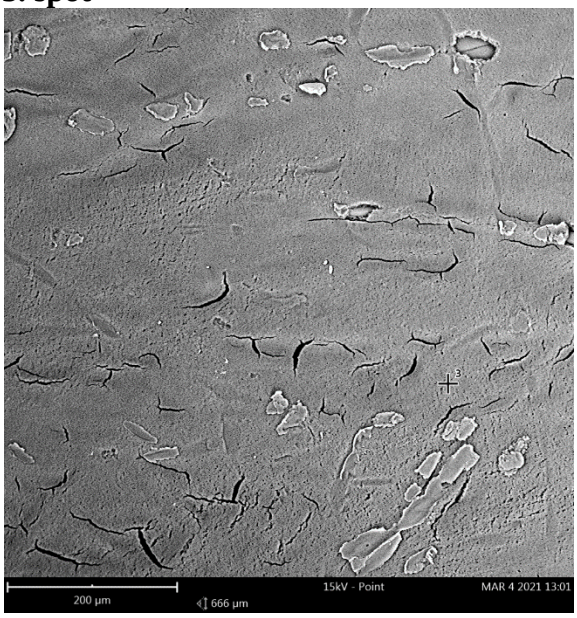

Element Number	Element Symbol	Element Name	Atomic Conc.	Weight Conc.
6	C	Carbon	100.00	100.00

FOV: 666 µm, Mode: 15kV - Point, Detector: BSD Full, Time: MAR 4 2021 13:01

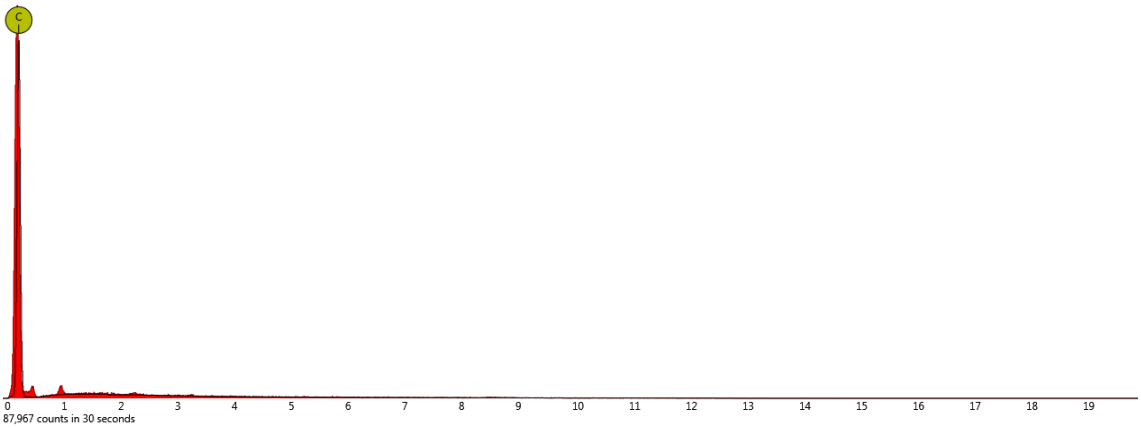

Disabled elements: B

4. spot

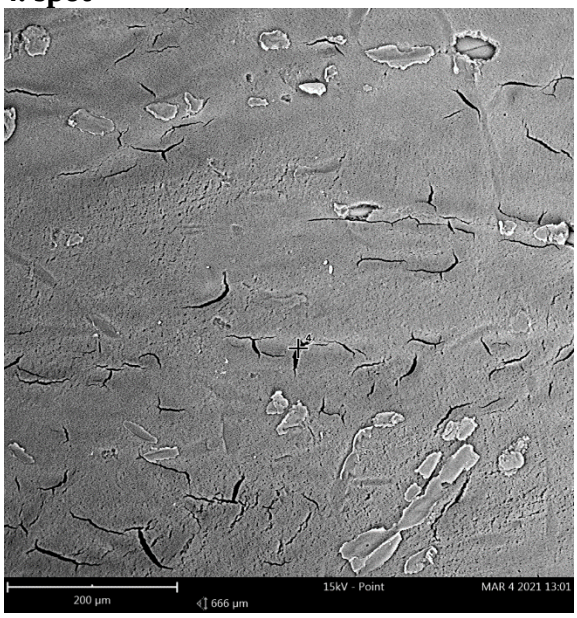

Element Number	Element Symbol	Element Name	Atomic Conc.	Weight Conc.
6	C	Carbon	100.00	100.00

FOV: 666 µm, Mode: 15kV - Point, Detector: BSD Full, Time: MAR 4 2021 13:01

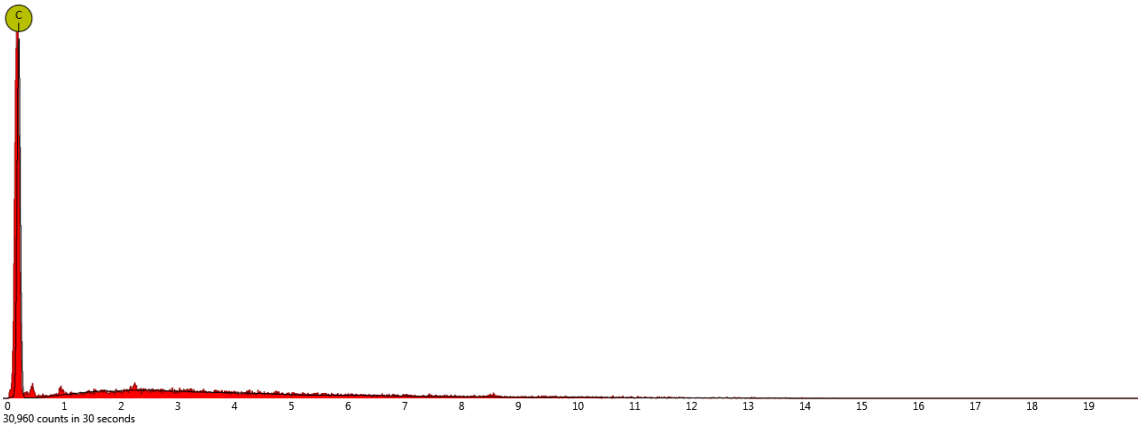

Disabled elements: B

5. spot

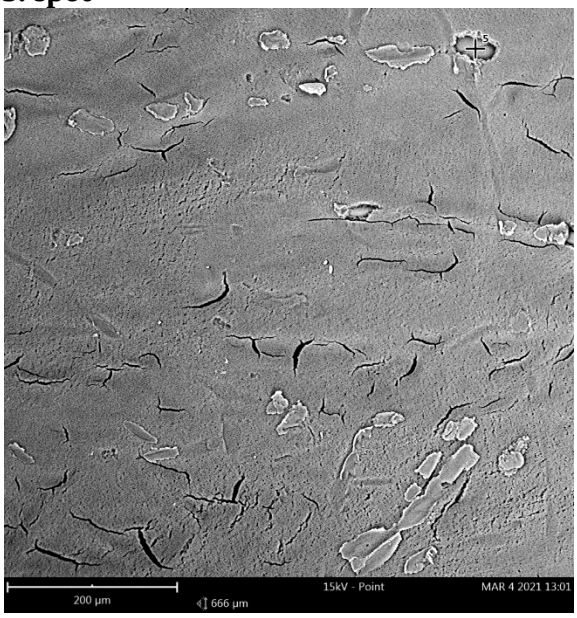

Element Number	Element Symbol	Element Name	Atomic Conc.	Weight Conc.
6	C	Carbon	100.00	100.00

FOV: 666 µm, Mode: 15kV - Point, Detector: BSD Full, Time: MAR 4 2021 13:01

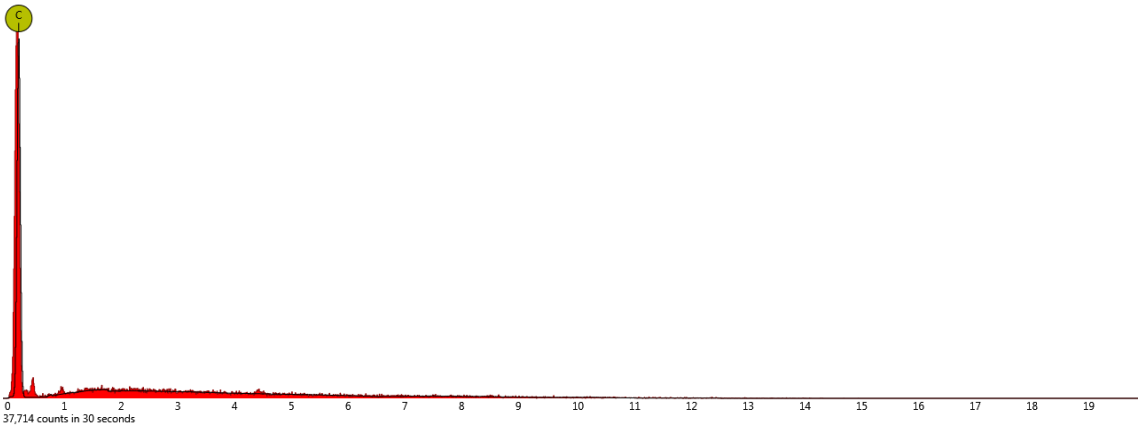

Disabled elements: B

Material A map analysis

1. map

Combined map

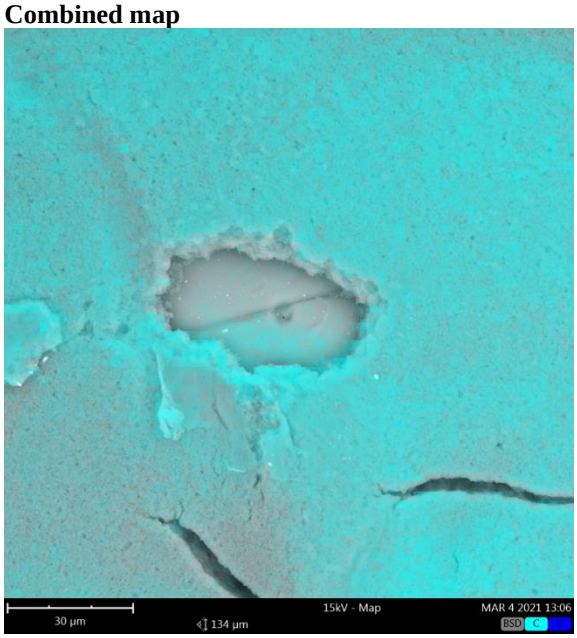

Element Number	Element Symbol	Element Name	Atomic Conc.	Weight Conc.
6	C	Carbon	62.47	55.55
8	O	Oxygen	37.53	44.45

FOV: 134 µm, Mode: 15kV - Map, Detector: BSD Full, Time: MAR 4 2021 13:06

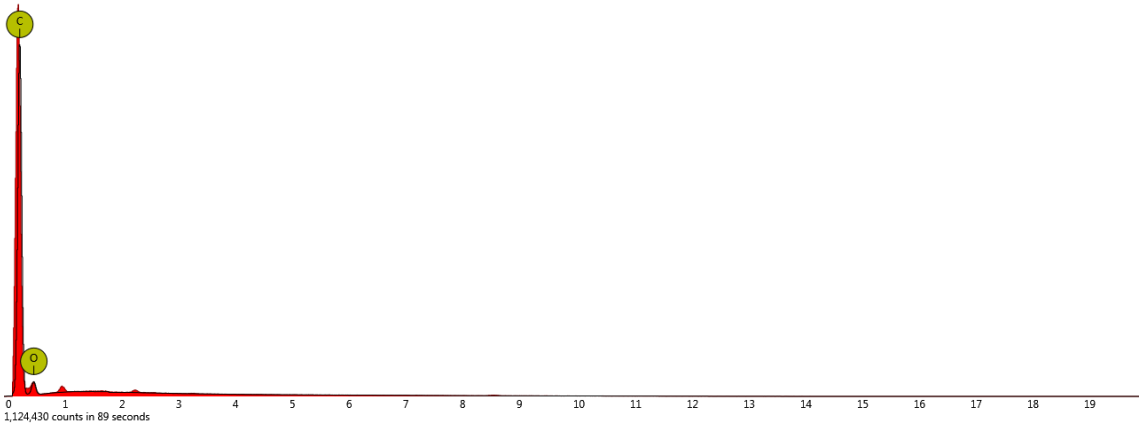

Disabled elements: B

Cut out of the map (resolution: 64x64 pixels)

Carbon

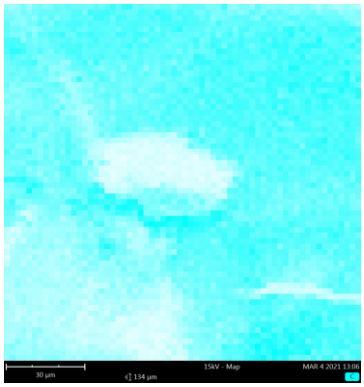

Oxygen

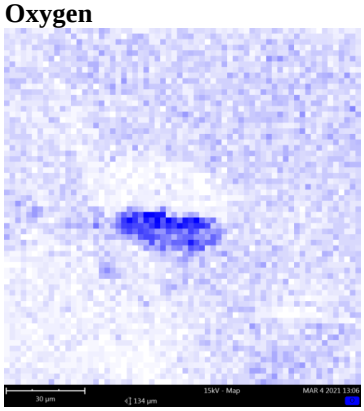

Material B point analysis

1. spot

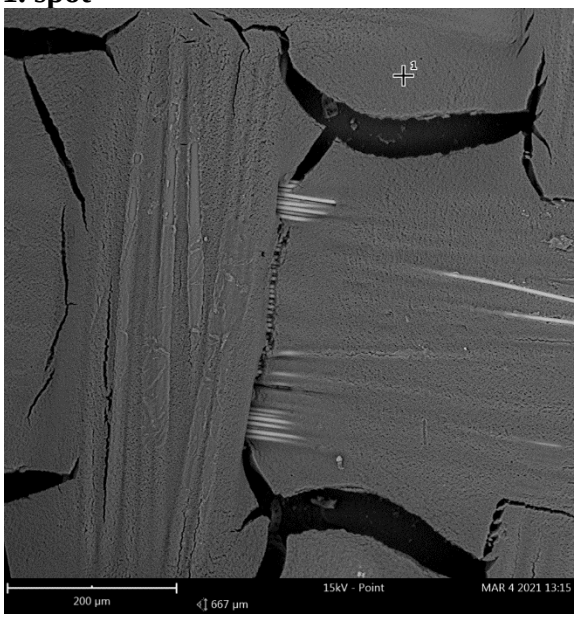

Element Number	Element Symbol	Element Name	Atomic Conc.	Weight Conc.
6	C	Carbon	100.00	100.00

FOV: 667 µm, Mode: 15kV - Point, Detector: BSD Full, Time: MAR 4 2021 13:15

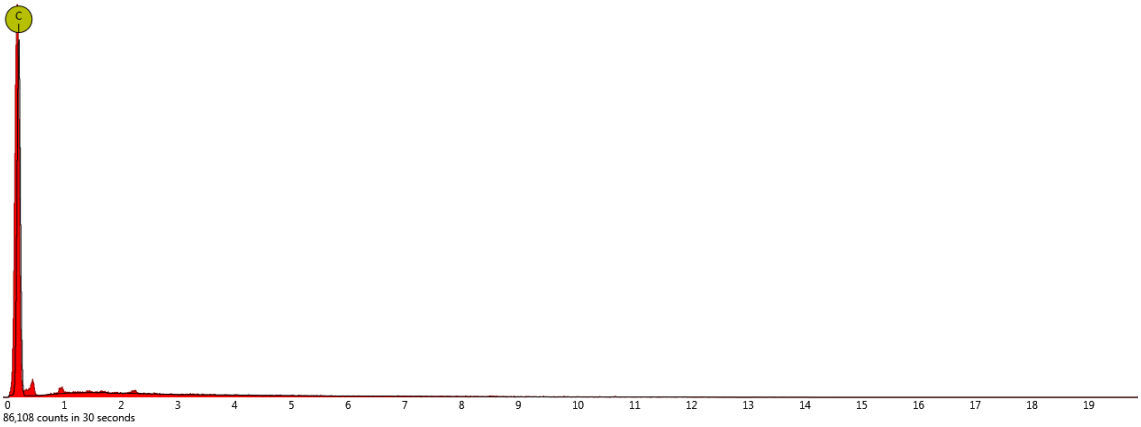

Disabled elements: B

2. spot

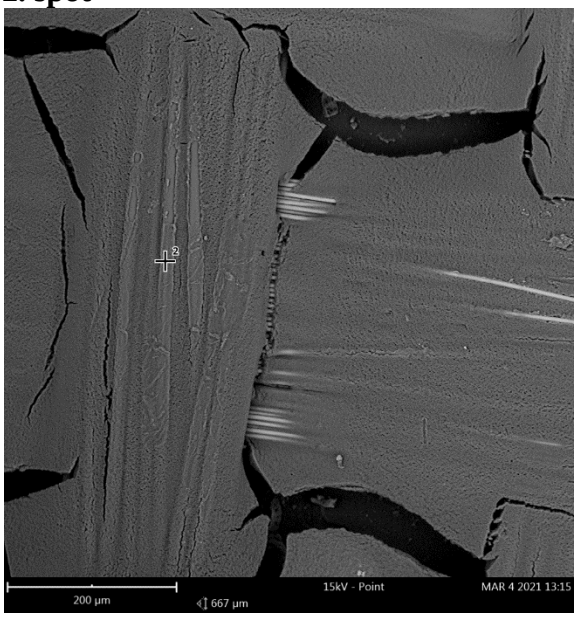

Element Number	Element Symbol	Element Name	Atomic Conc.	Weight Conc.
6	C	Carbon	100.00	100.00

FOV: 667 µm, Mode: 15kV - Point, Detector: BSD Full, Time: MAR 4 2021 13:15

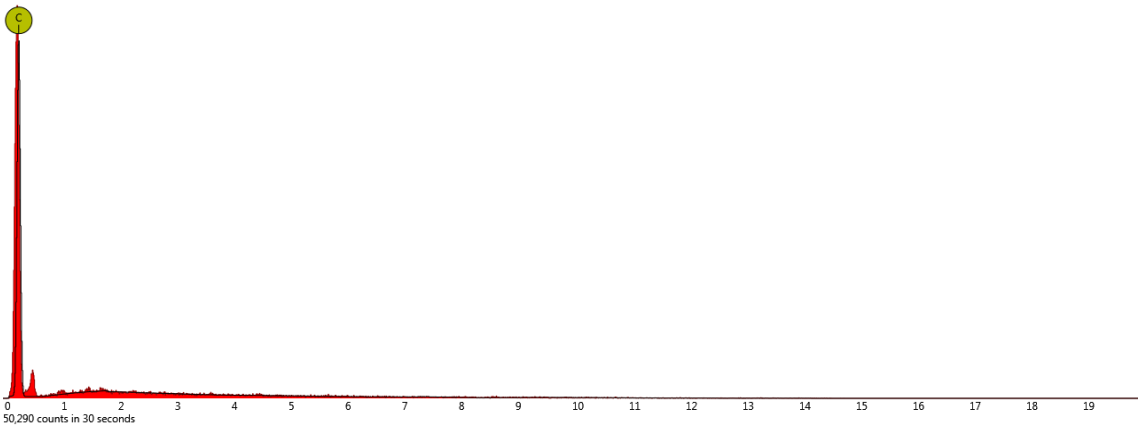

Disabled elements: B

3. spot

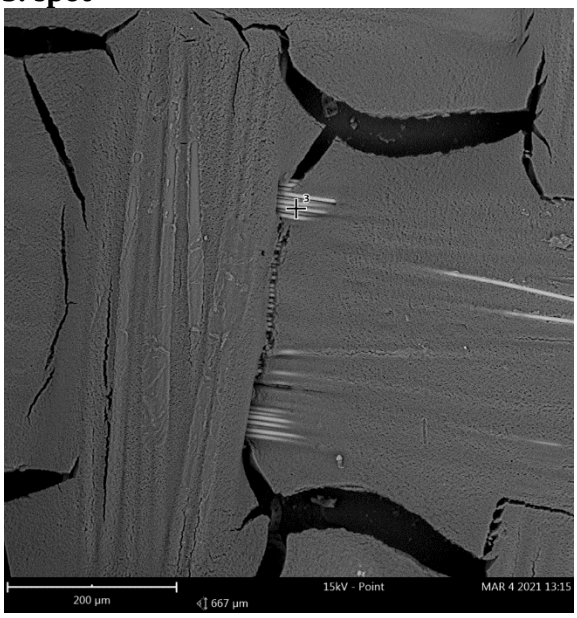

Element Number	Element Symbol	Element Name	Atomic Conc.	Weight Conc.
8	O	Oxygen	46.72	37.78
14	Si	Silicon	17.74	25.17
20	Ca	Calcium	7.24	14.66
6	C	Carbon	21.42	13.00
13	Al	Aluminium	6.89	9.39

FOV: 667 µm, Mode: 15kV - Point, Detector: BSD Full, Time: MAR 4 2021 13:15

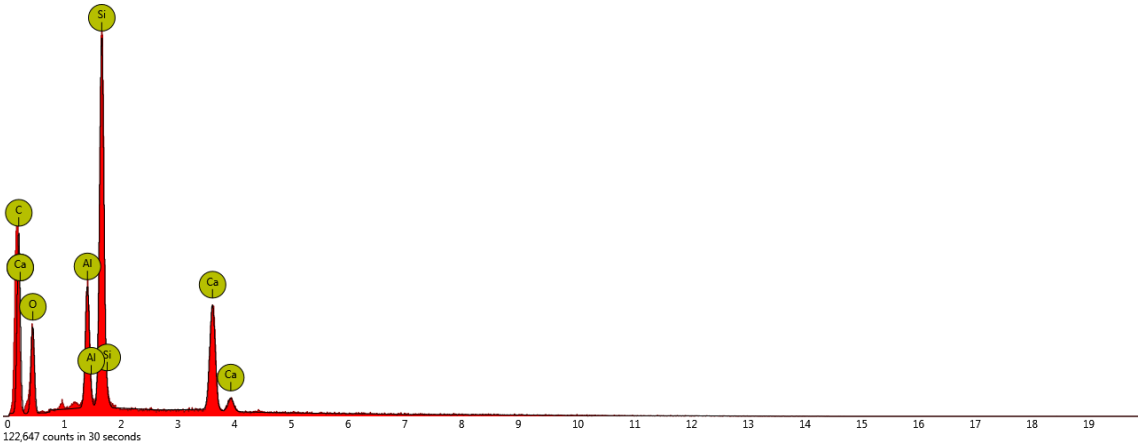

Disabled elements: B

4. spot

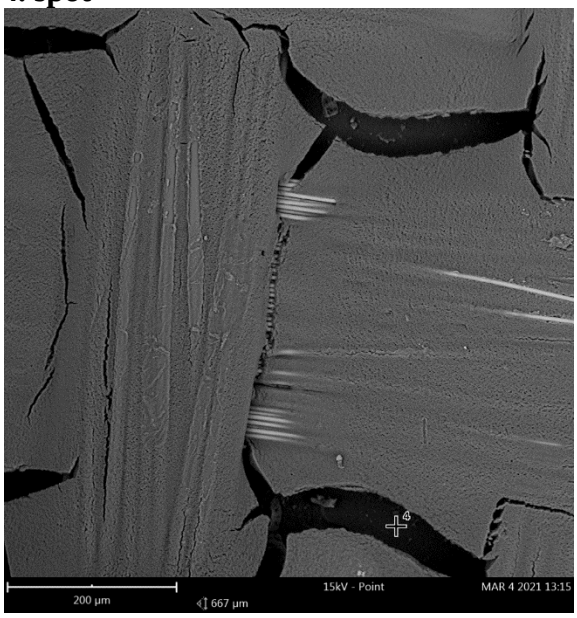

Element Number	Element Symbol	Element Name	Atomic Conc.	Weight Conc.
6	C	Carbon	100.00	100.00

FOV: 667 µm, Mode: 15kV - Point, Detector: BSD Full, Time: MAR 4 2021 13:15

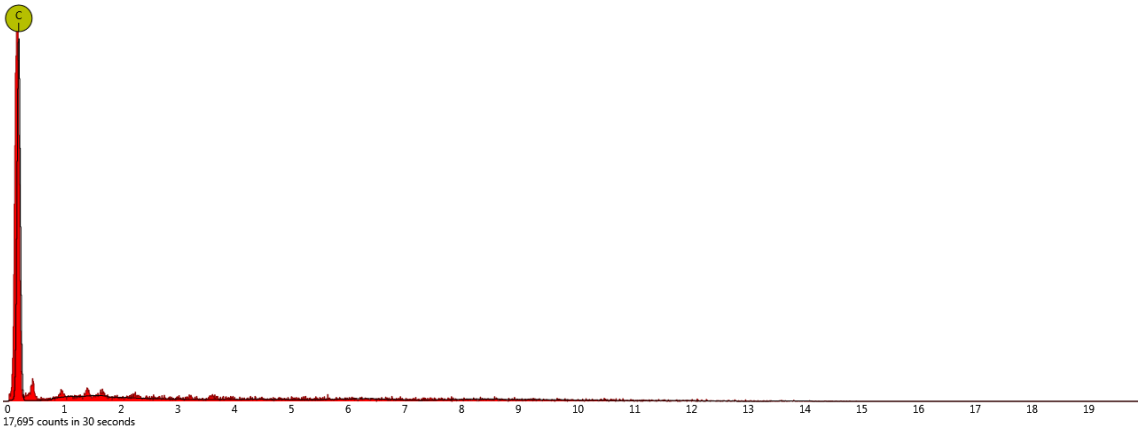

Disabled elements: B

Material B map analysis

1. map

Combined map

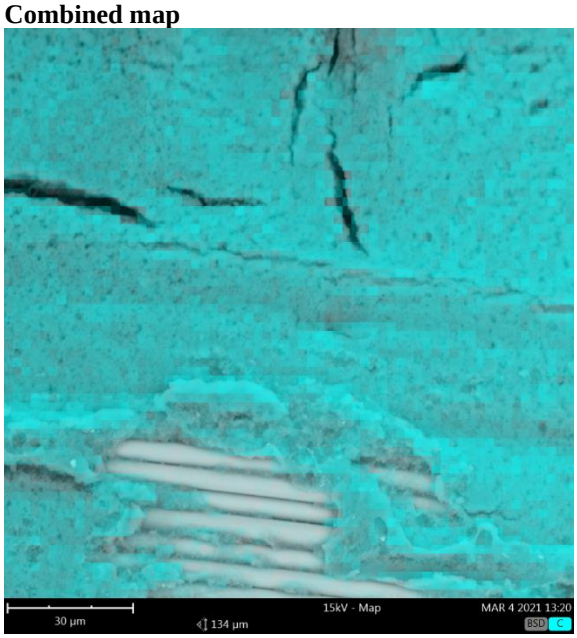

Element Number	Element Symbol	Element Name	Atomic Conc.	Weight Conc.
6	C	Carbon	100.00	100.00

FOV: 134 µm, Mode: 15kV - Map, Detector: BSD Full, Time: MAR 4 2021 13:20

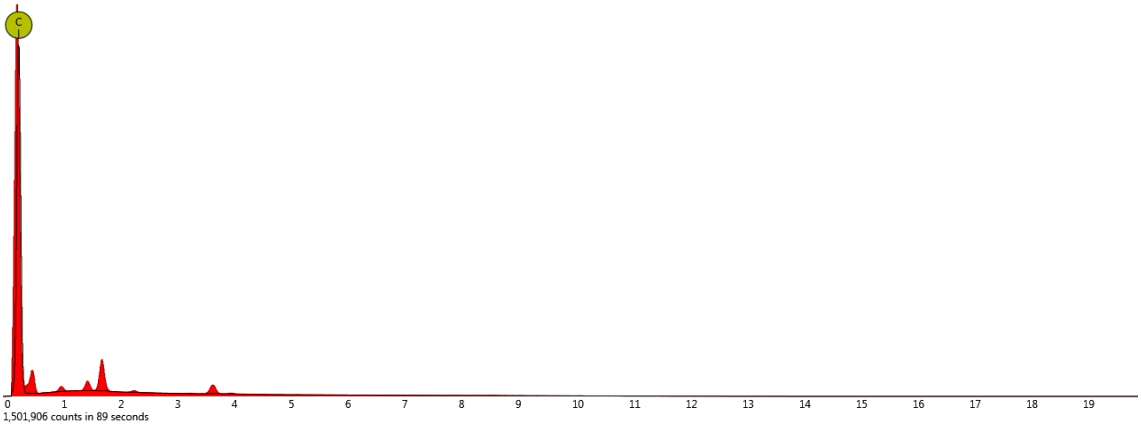

Disabled elements: B

Cut out of the map (resolution: 64x64 pixels)

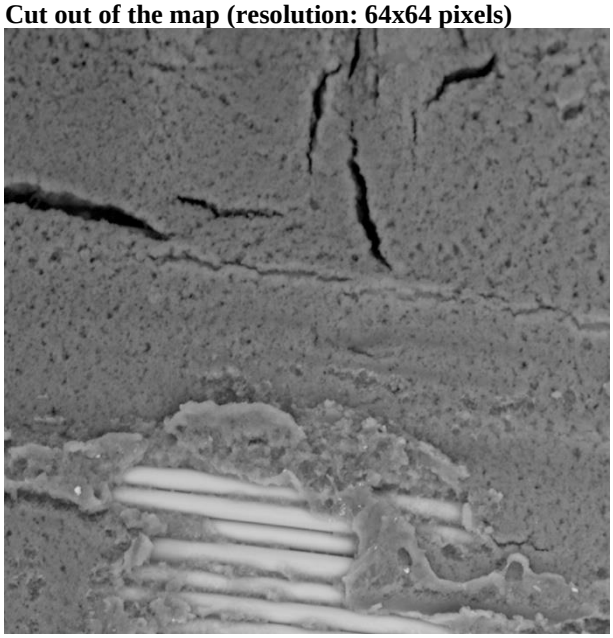

Carbon

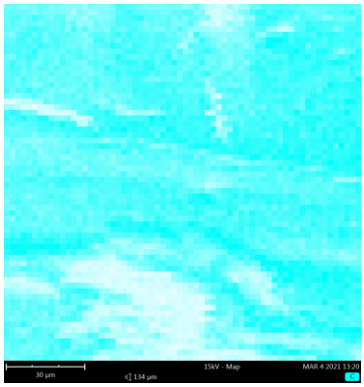

Material C point analysis

1. spot

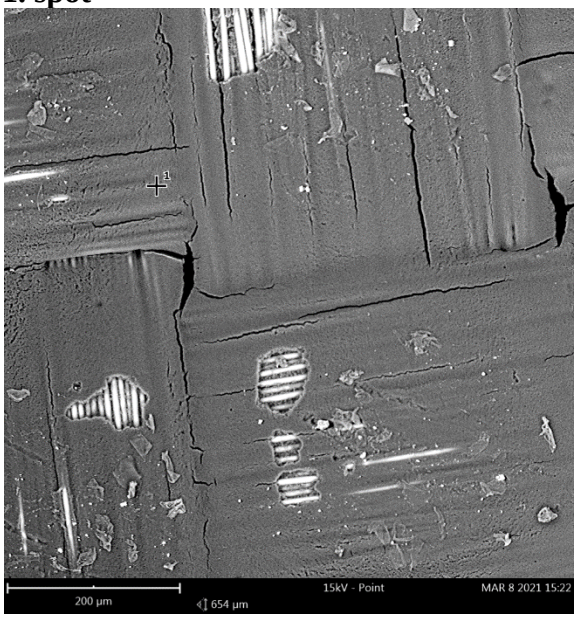

Element Number	Element Symbol	Element Name	Atomic Conc.	Weight Conc.
6	C	Carbon	100.00	100.00

FOV: 654 µm, Mode: 15kV - Point, Detector: BSD Full, Time: MAR 8 2021 15:22

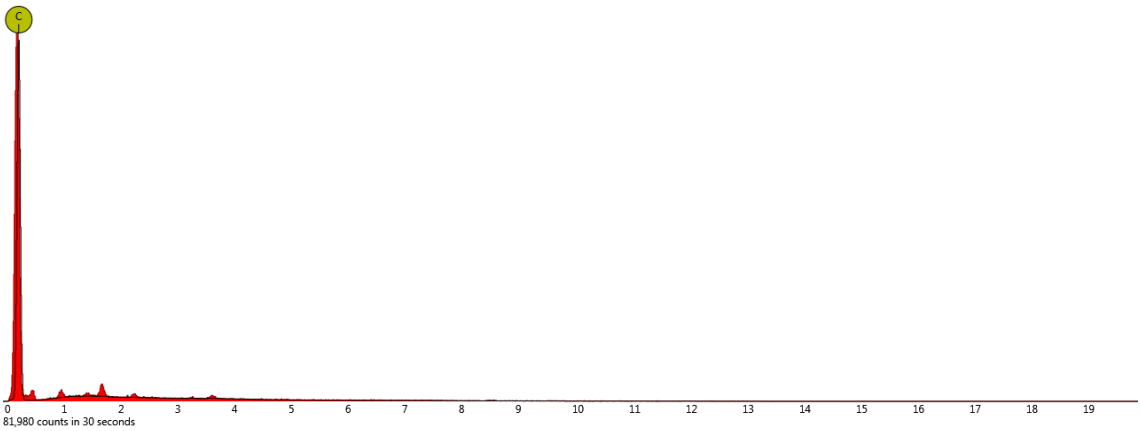

Disabled elements: B

2. spot

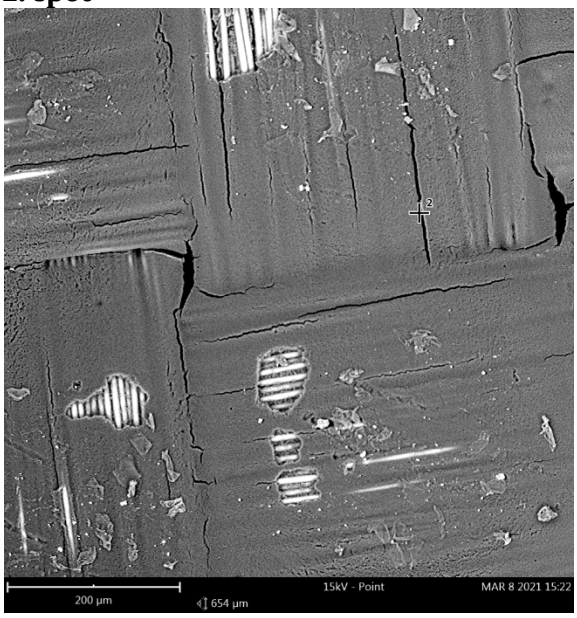

Element Number	Element Symbol	Element Name	Atomic Conc.	Weight Conc.
6	C	Carbon	100.00	100.00

FOV: 654 µm, Mode: 15kV - Point, Detector: BSD Full, Time: MAR 8 2021 15:22

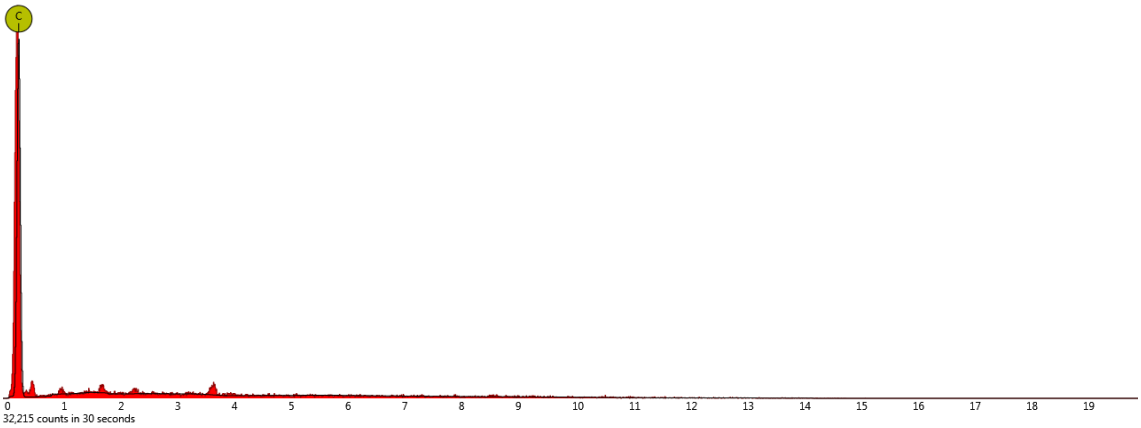

Disabled elements: B

3. spot

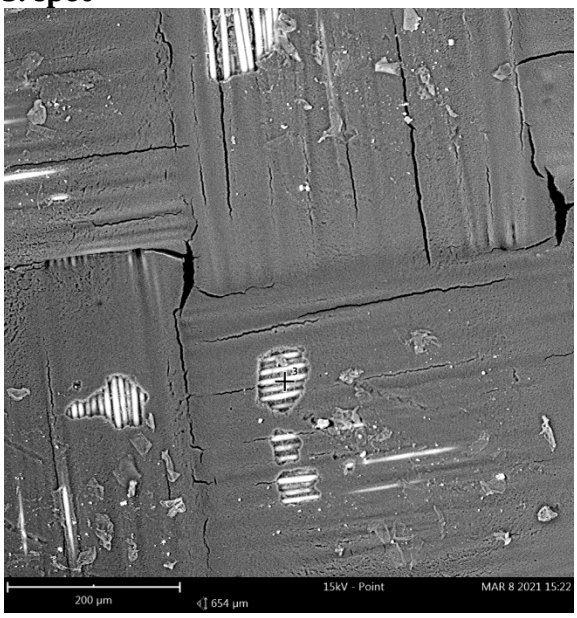

Element Number	Element Symbol	Element Name	Atomic Conc.	Weight Conc.
6	C	Carbon	72.91	49.05
20	Ca	Calcium	12.41	27.85
14	Si	Silicon	14.69	23.10

FOV: 654 µm, Mode: 15kV - Point, Detector: BSD Full, Time: MAR 8 2021 15:22

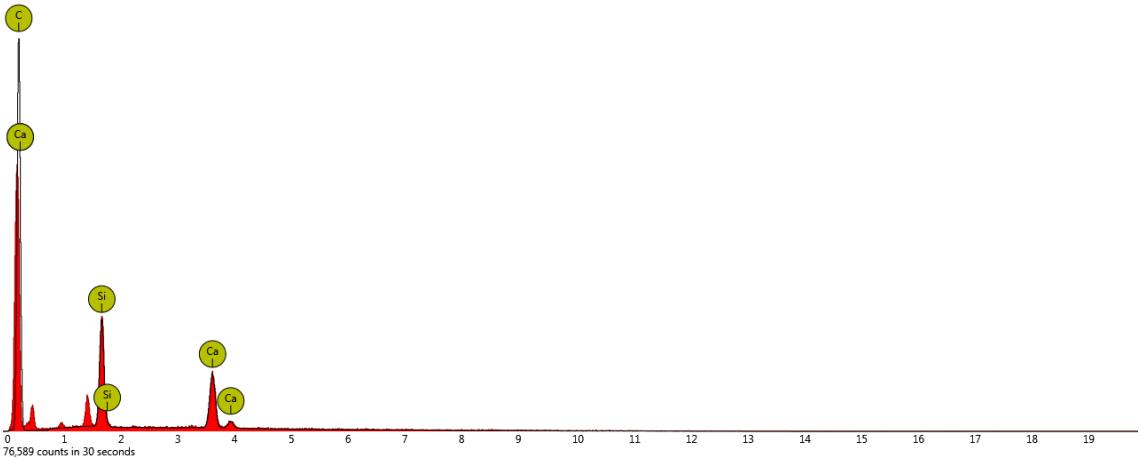

Disabled elements: B

4. spot

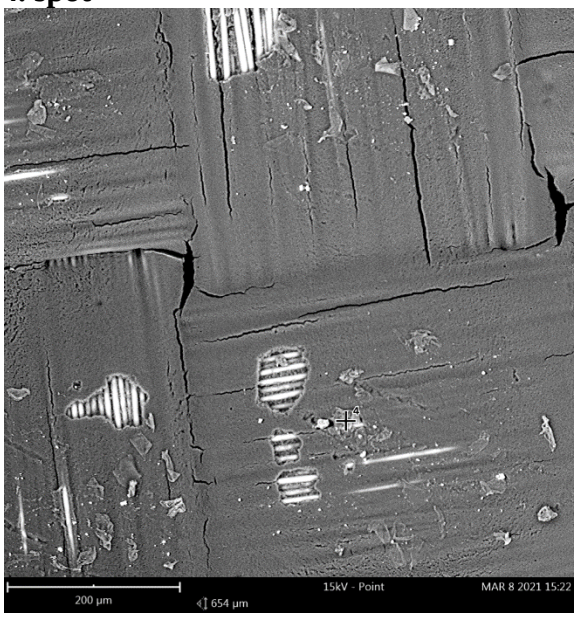

Element Number	Element Symbol	Element Name	Atomic Conc.	Weight Conc.
8	O	Oxygen	48.01	51.69
6	C	Carbon	46.19	37.33
14	Si	Silicon	5.81	10.98

FOV: 654 µm, Mode: 15kV - Point, Detector: BSD Full, Time: MAR 8 2021 15:22

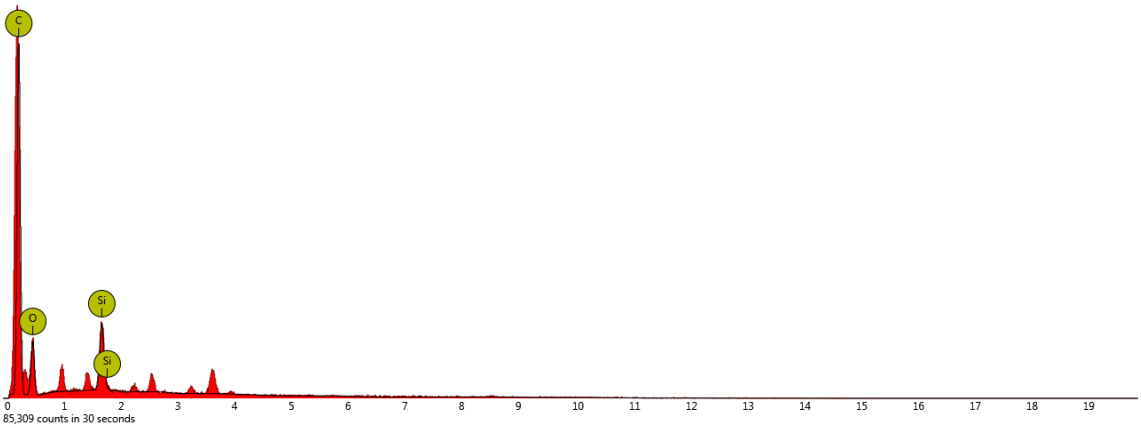

Disabled elements: B

5. spot

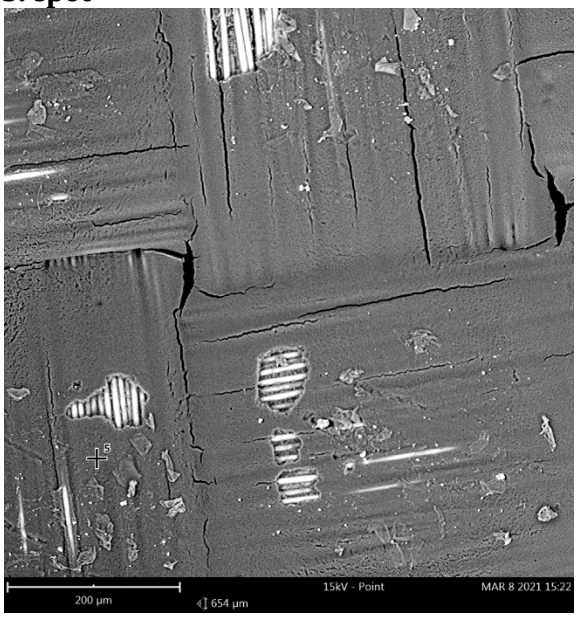

Element Number	Element Symbol	Element Name	Atomic Conc.	Weight Conc.
6	C	Carbon	100.00	100.00

FOV: 654 µm, Mode: 15kV - Point, Detector: BSD Full, Time: MAR 8 2021 15:22

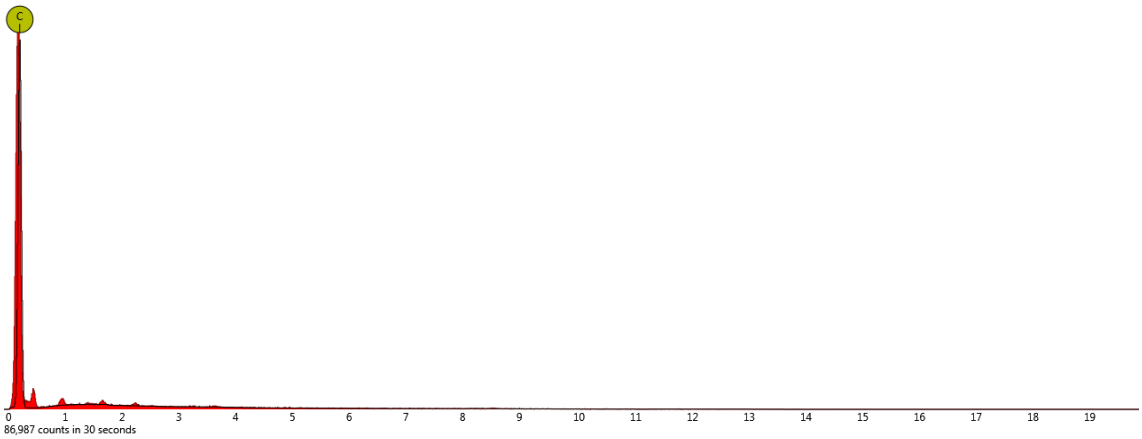

Disabled elements: B

Material C map analysis

1. map

Combined map

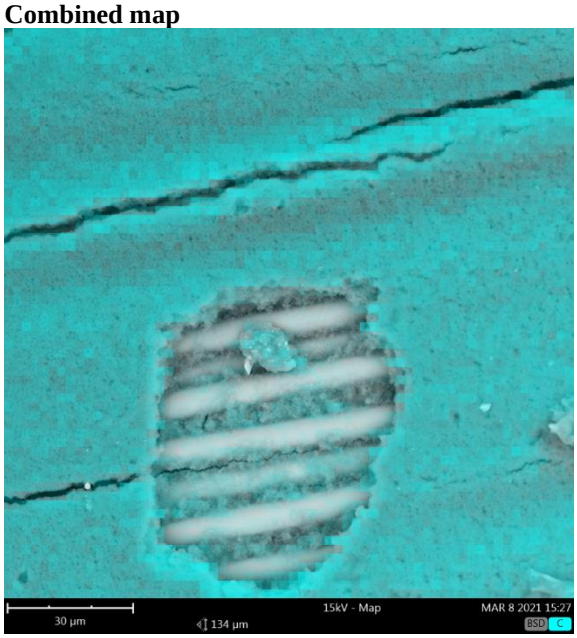

Element Number	Element Symbol	Element Name	Atomic Conc.	Weight Conc.
6	C	Carbon	100.00	100.00

FOV: 134 µm, Mode: 15kV - Map, Detector: BSD Full, Time: MAR 8 2021 15:27

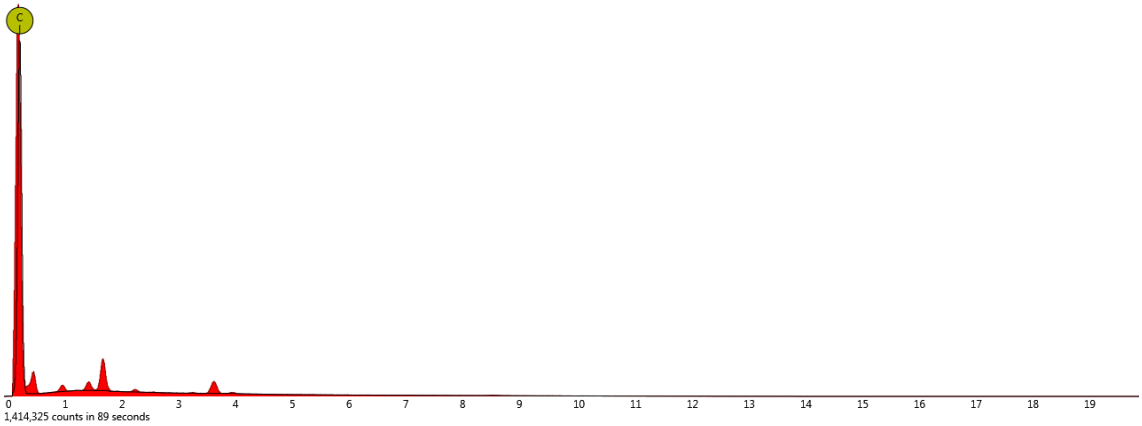

Disabled elements: B

Cut out of the map (resolution: 64x64 pixels)

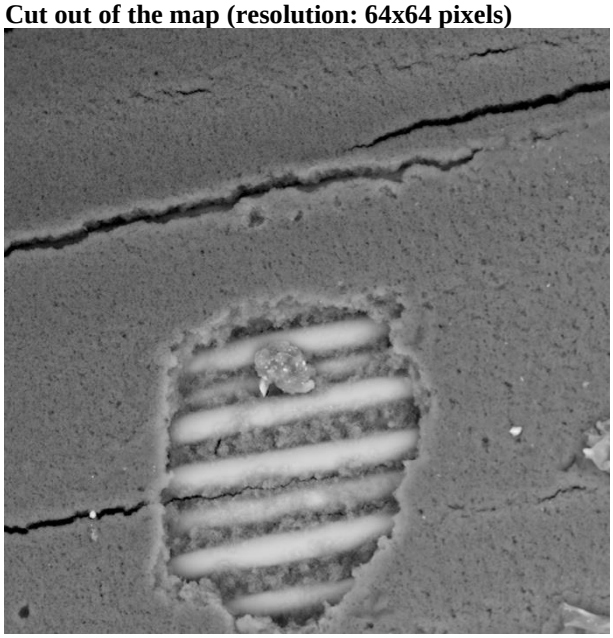

Carbon

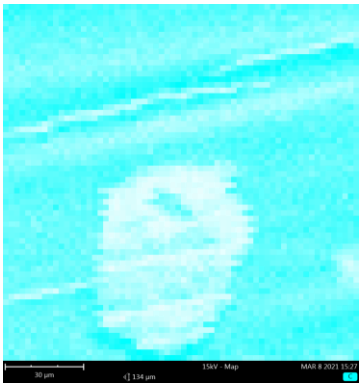

Infrared camera photos

This section of attachments shows the rest of the unshown images taken with an infrared camera during one of the experiments performed for this thesis.

Multiple scales of temperature photos

BU 34 50V

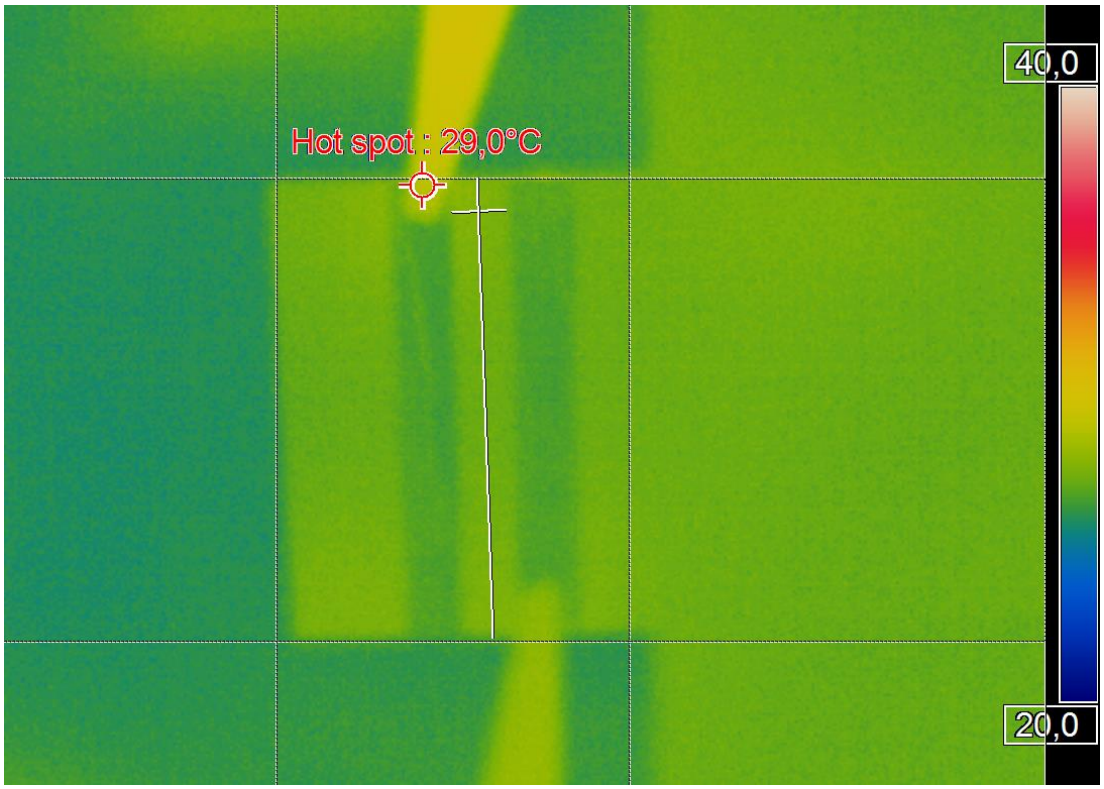

BU 34 100V

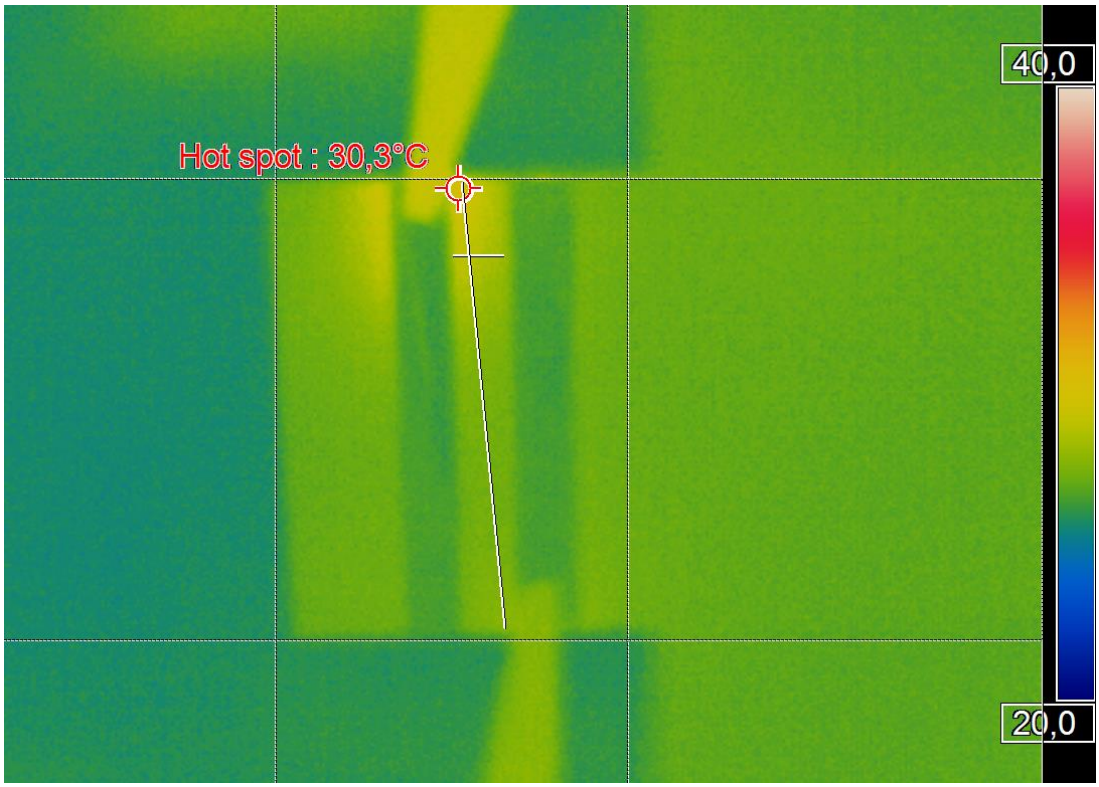

BU 34 150V

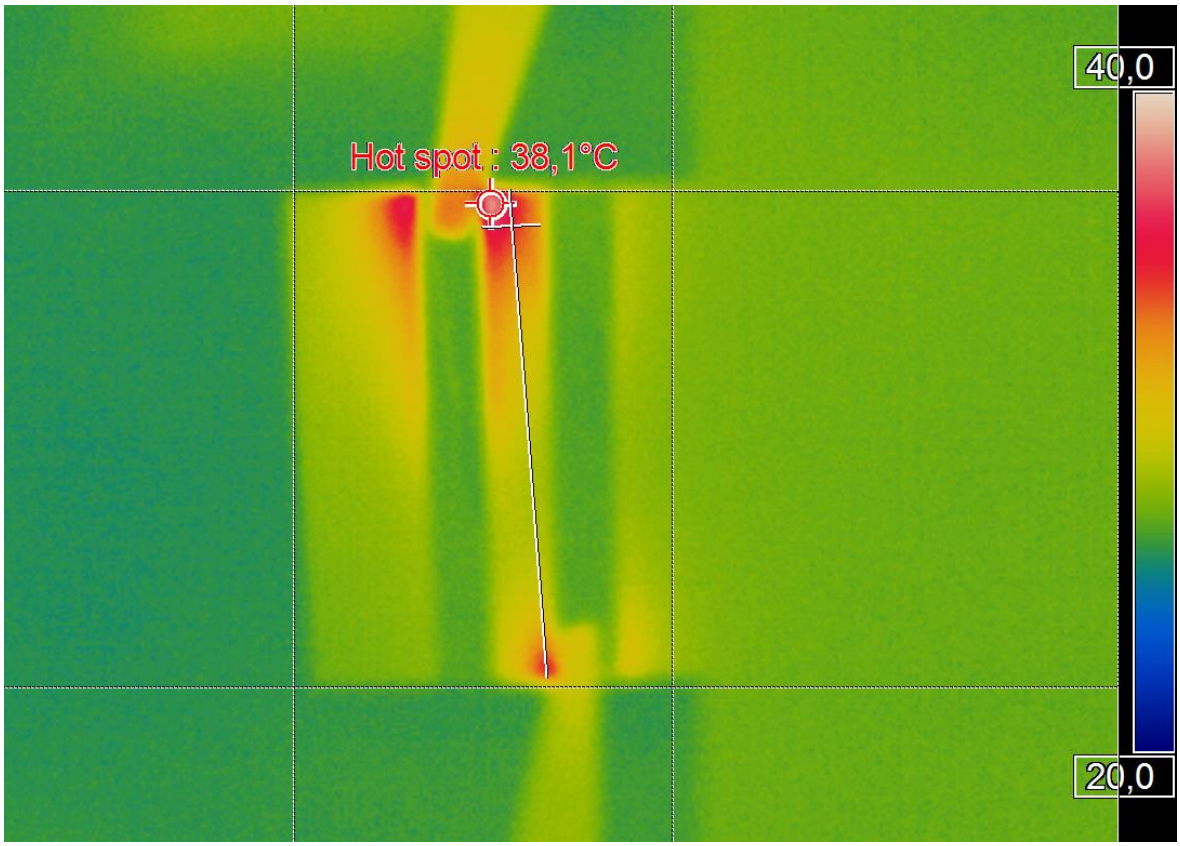

BU 34 200V

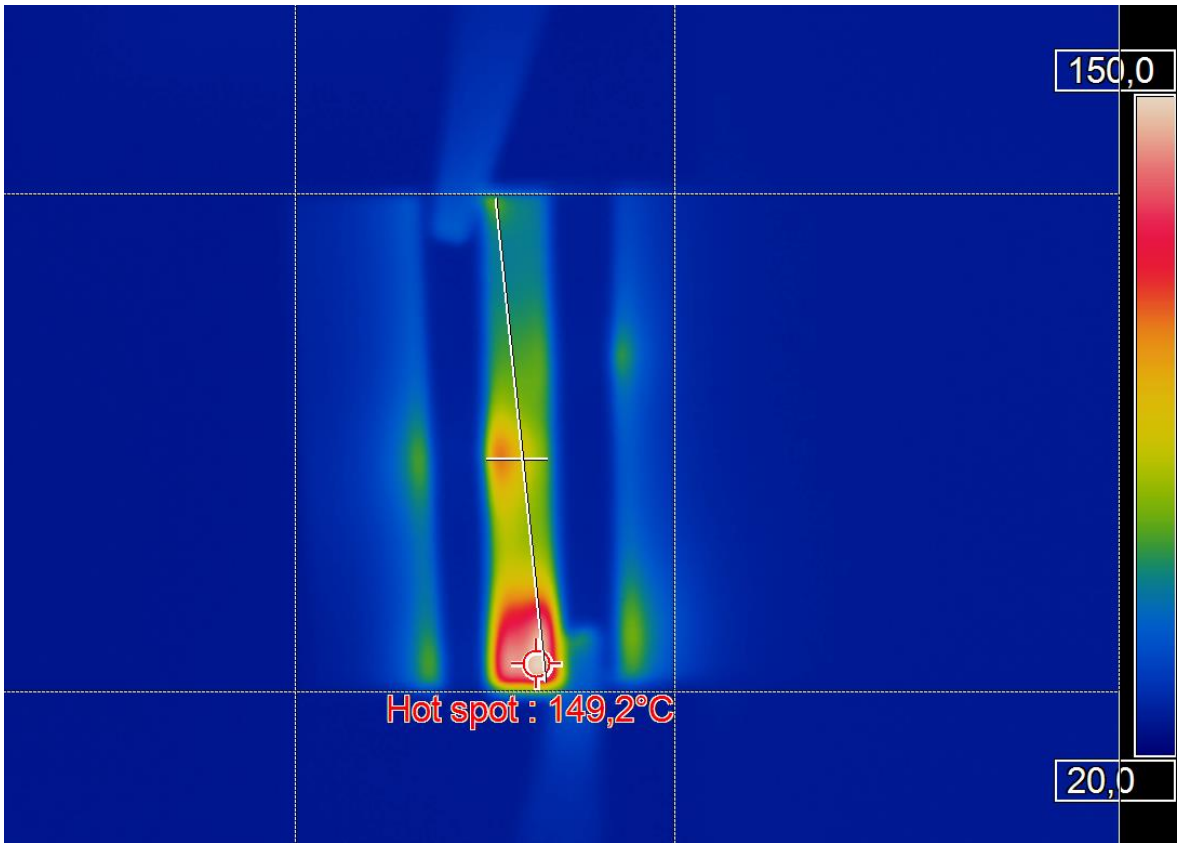

BU 34 250V

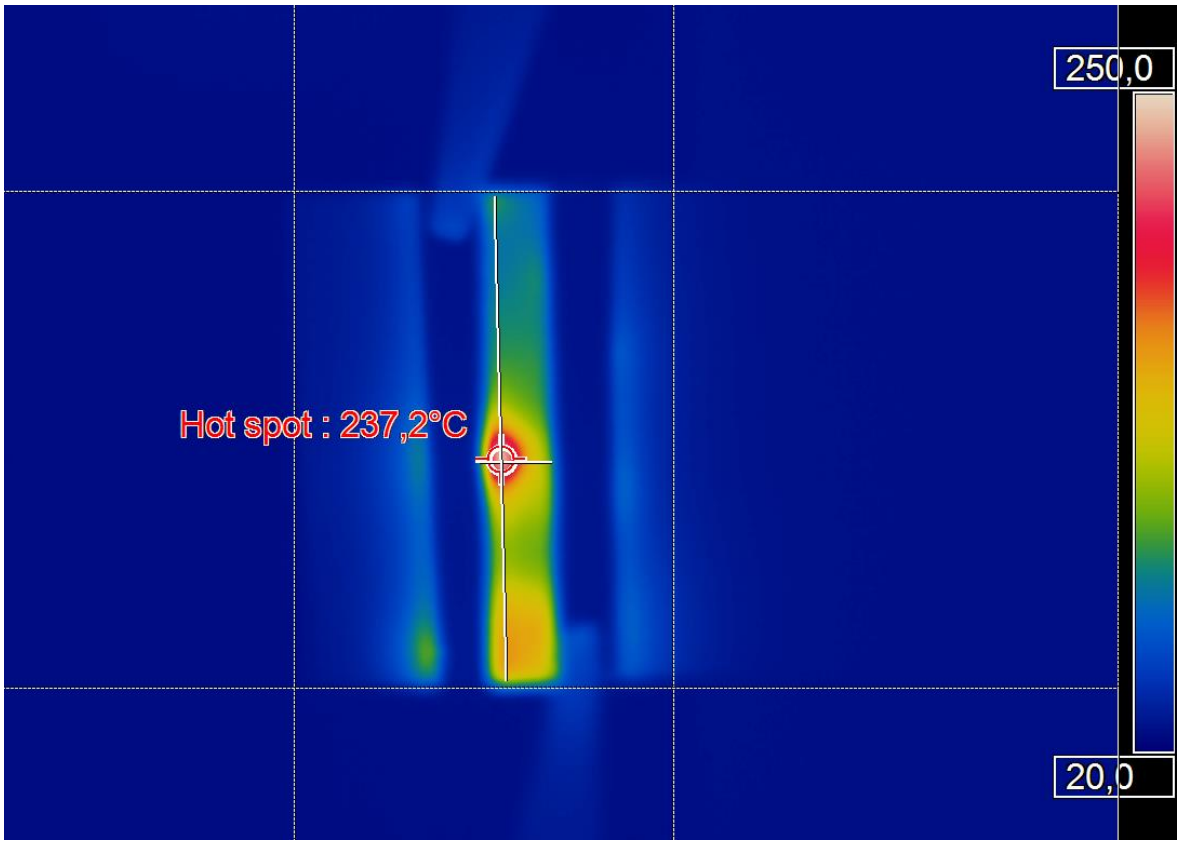

BU 81 50V

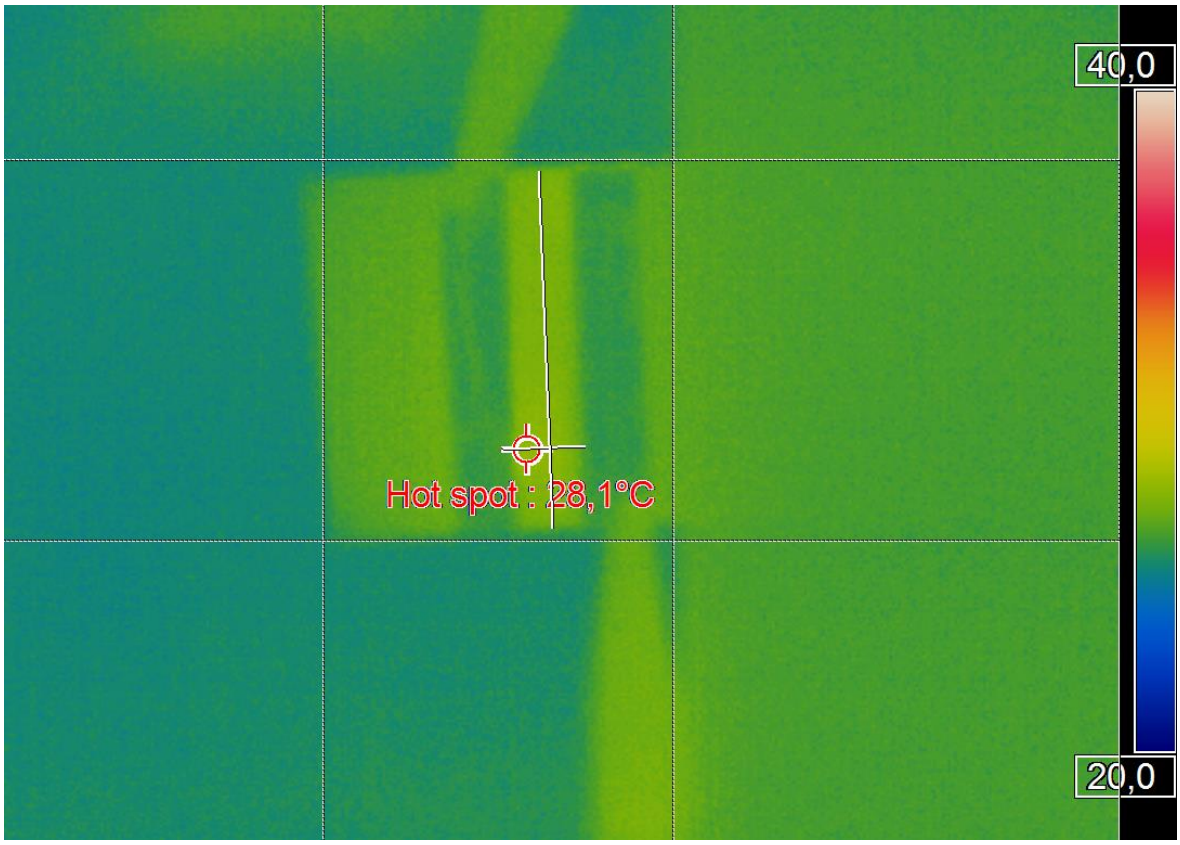

BU 81 100V

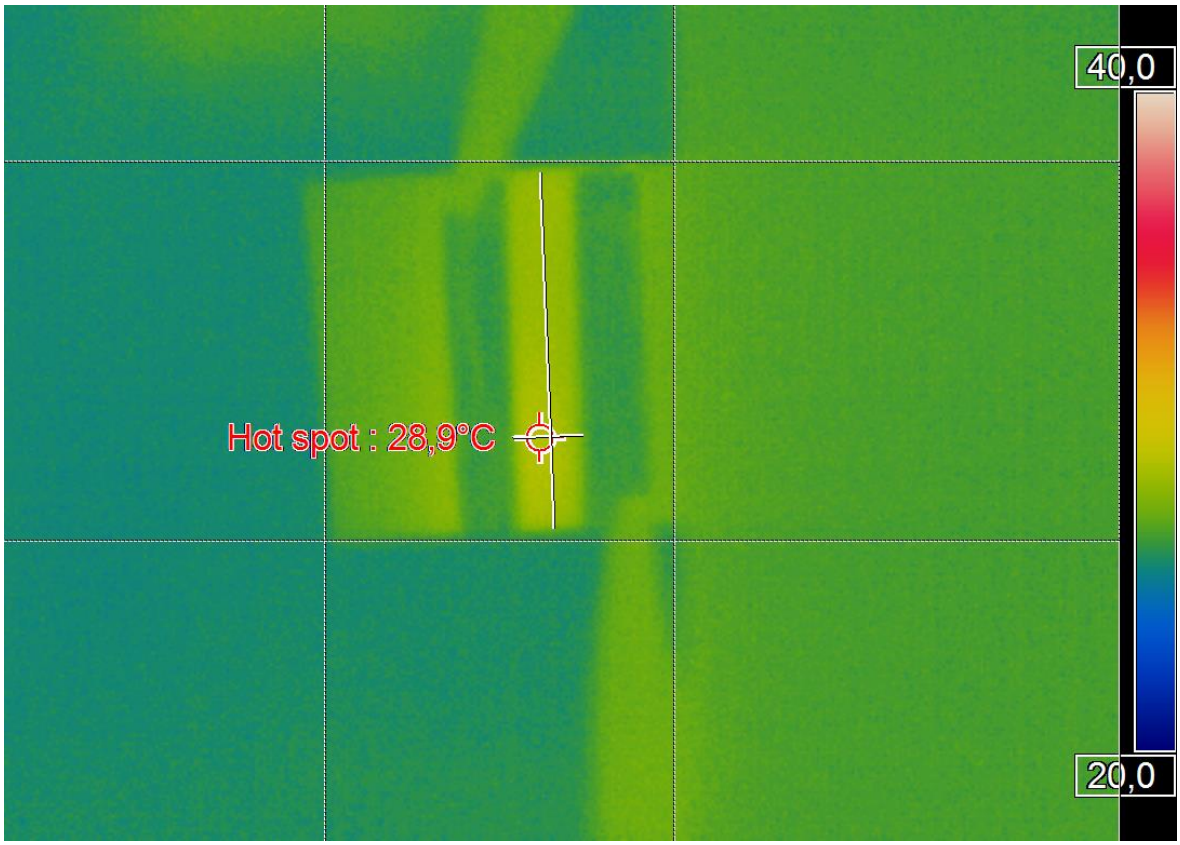

BU 81 150V

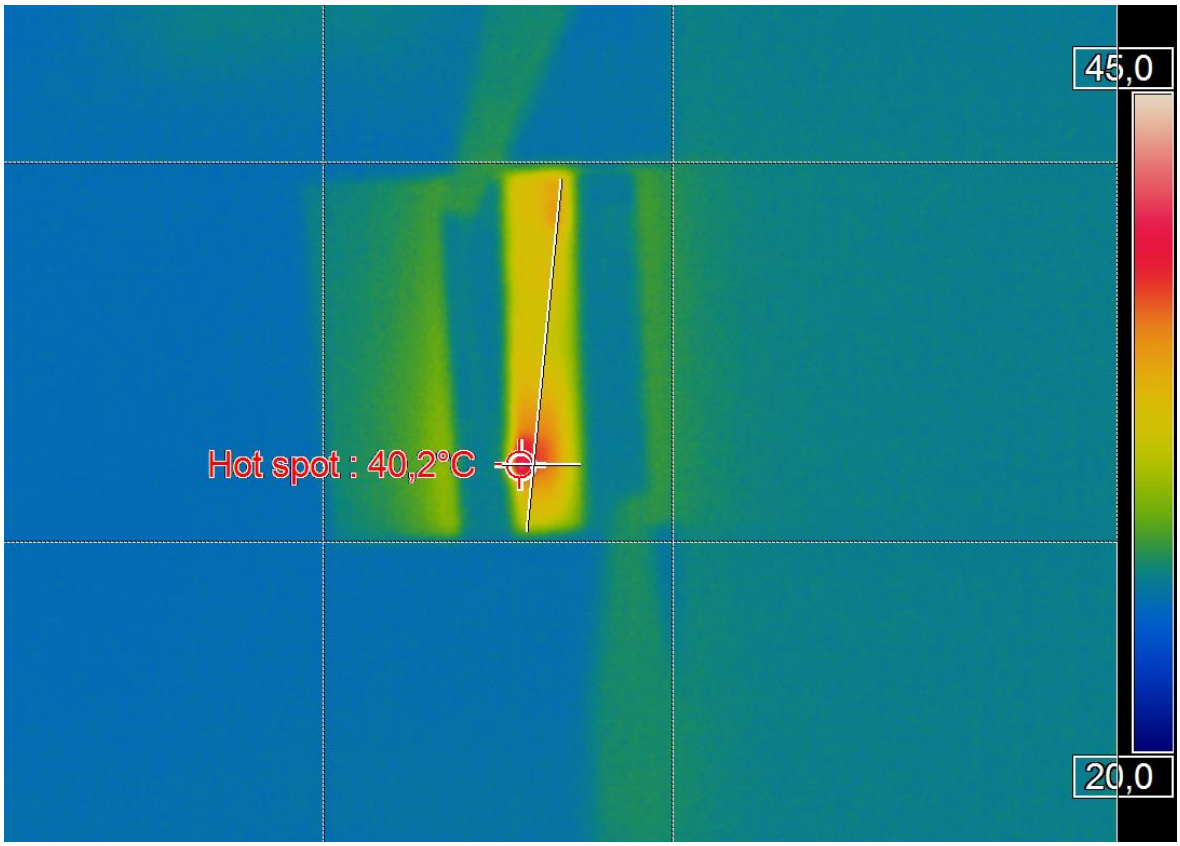

BU 81 200V

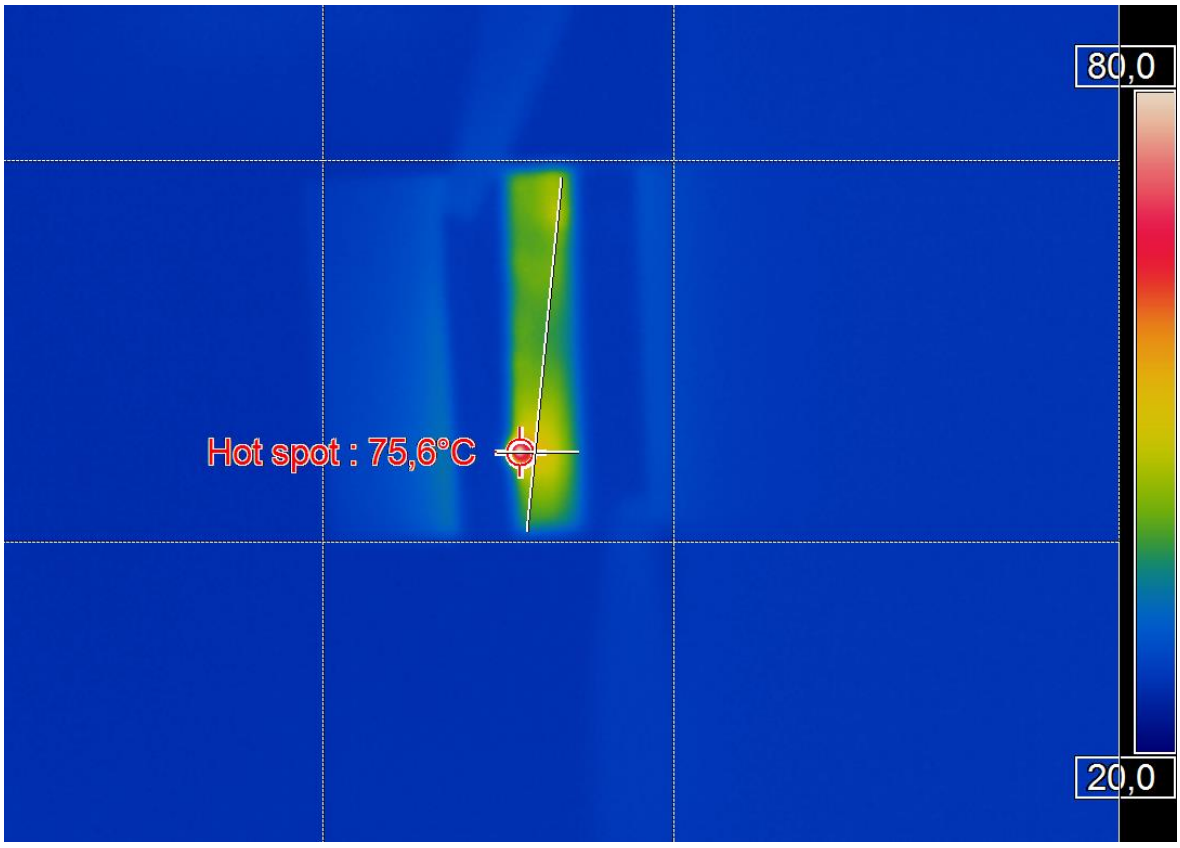

BU 81 250V

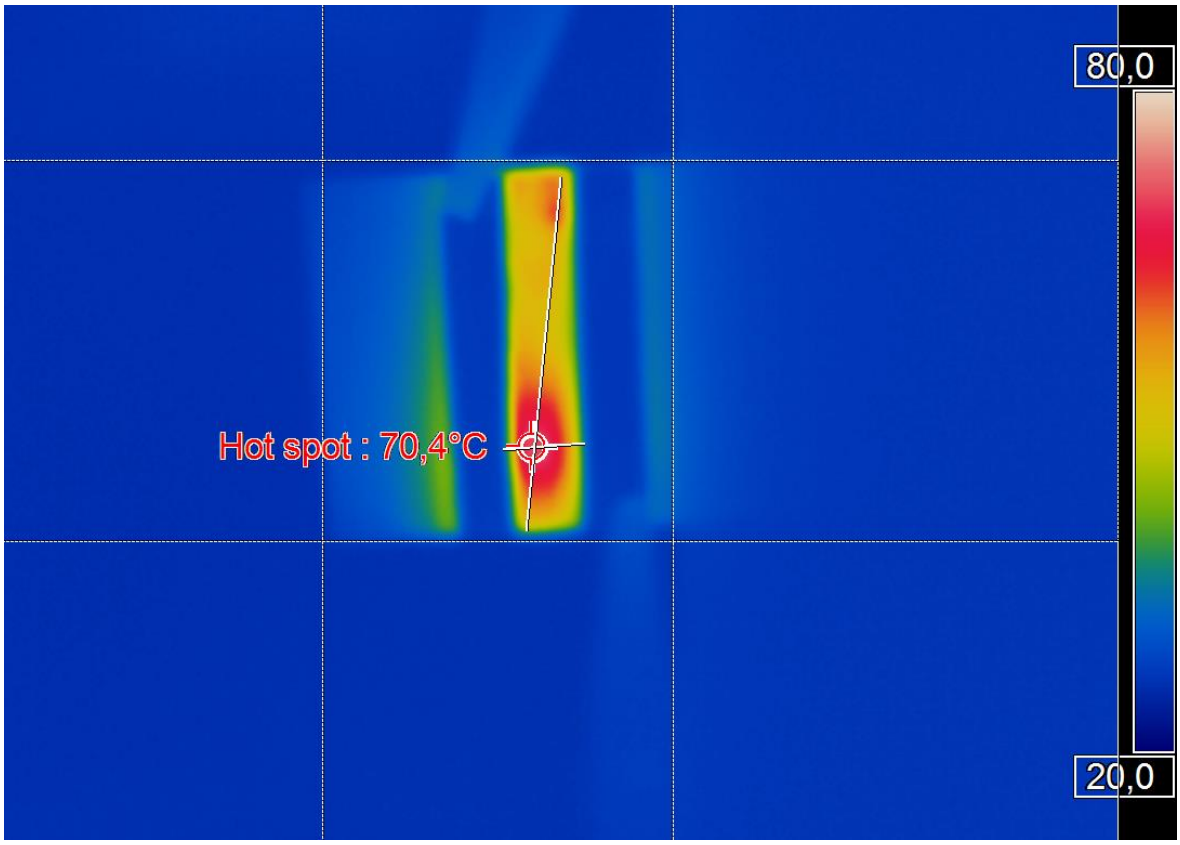

TB 51 50V

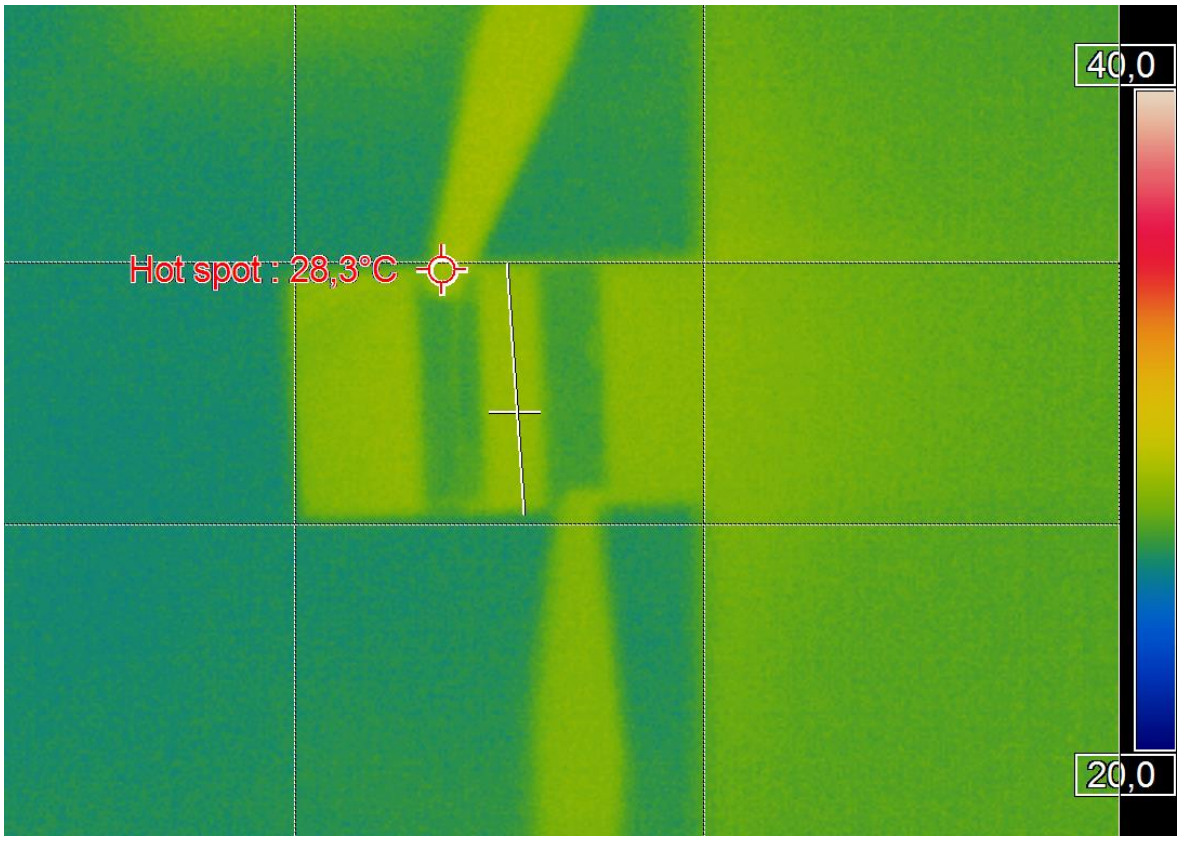

TB 51 100V

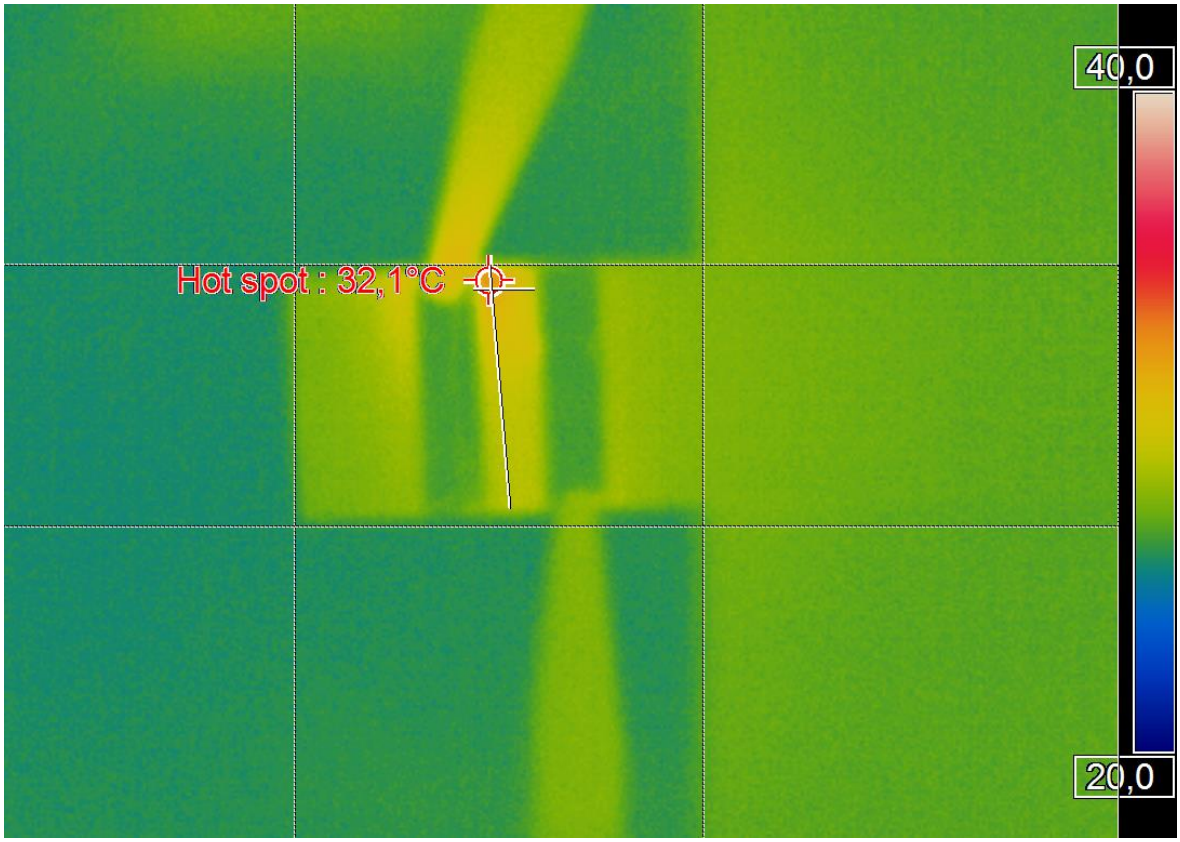

One scale of temperature photos

BU 34 50V

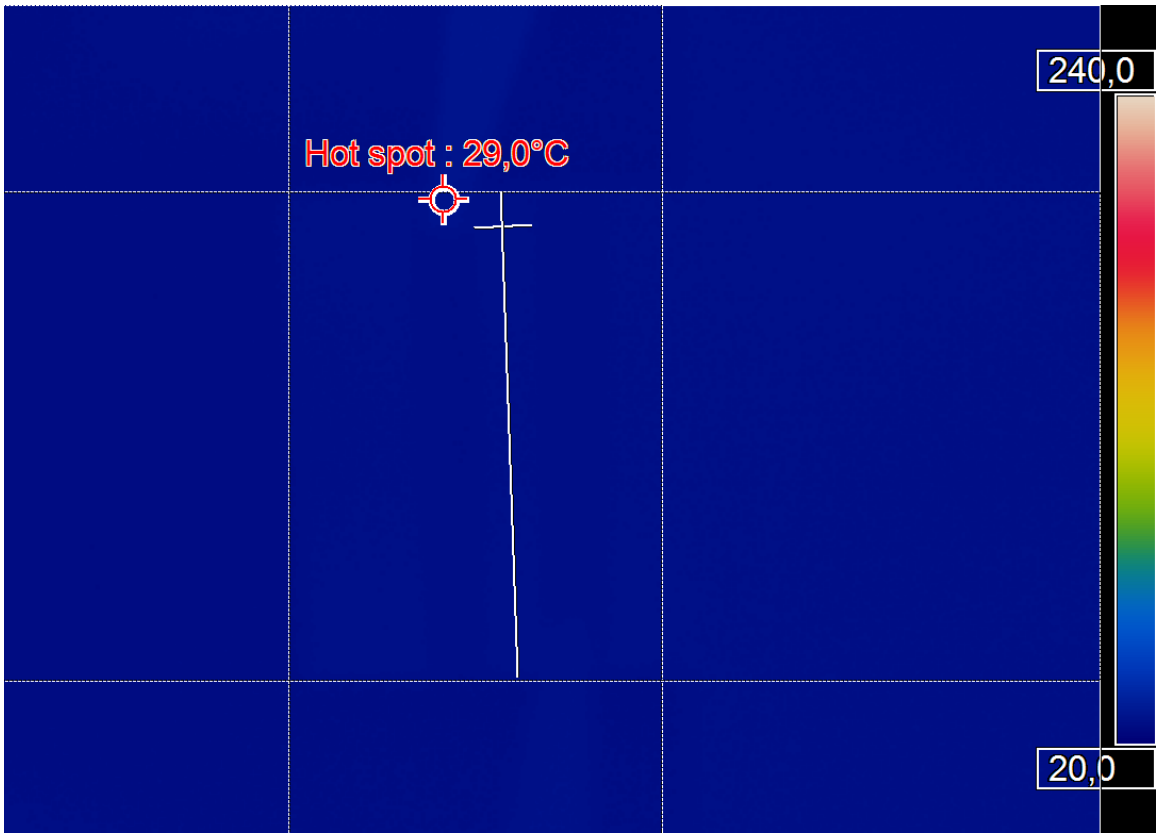

BU 34 100V

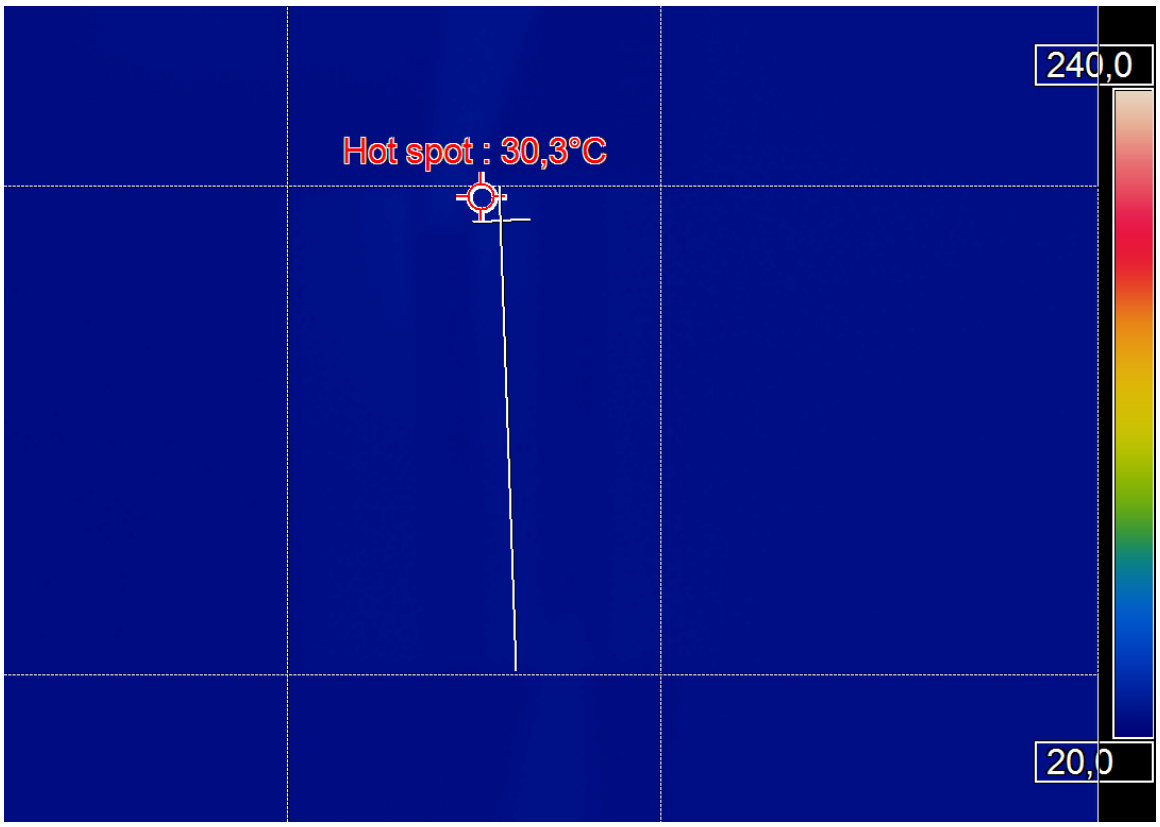

BU 34 150V

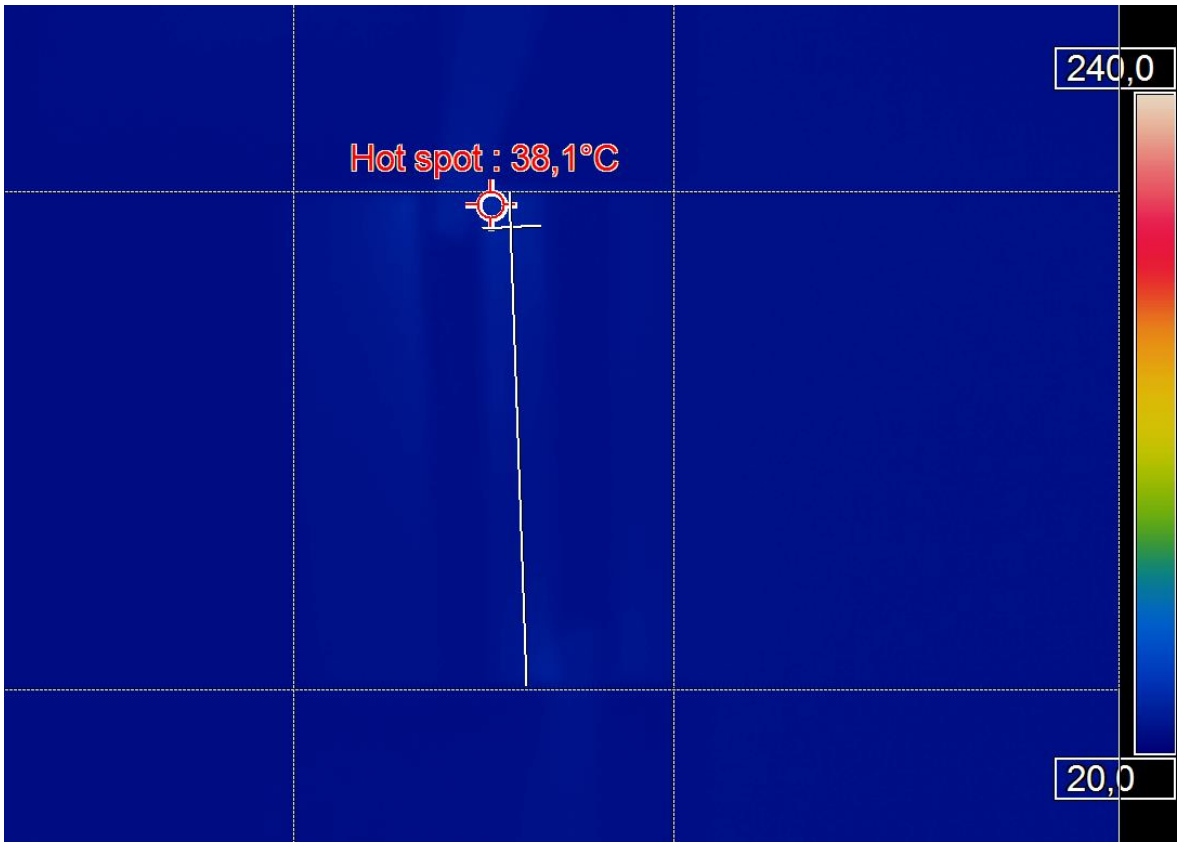

BU 34 200V

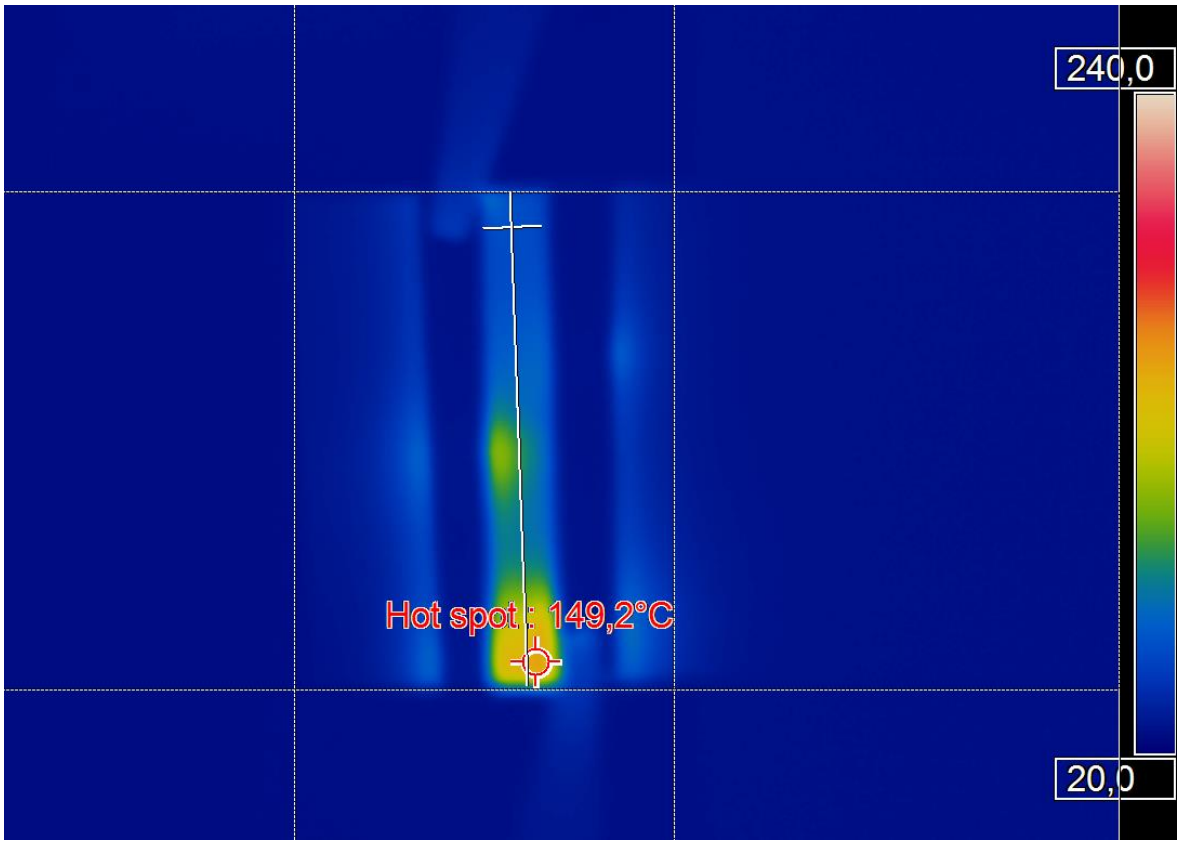

BU 34 250V

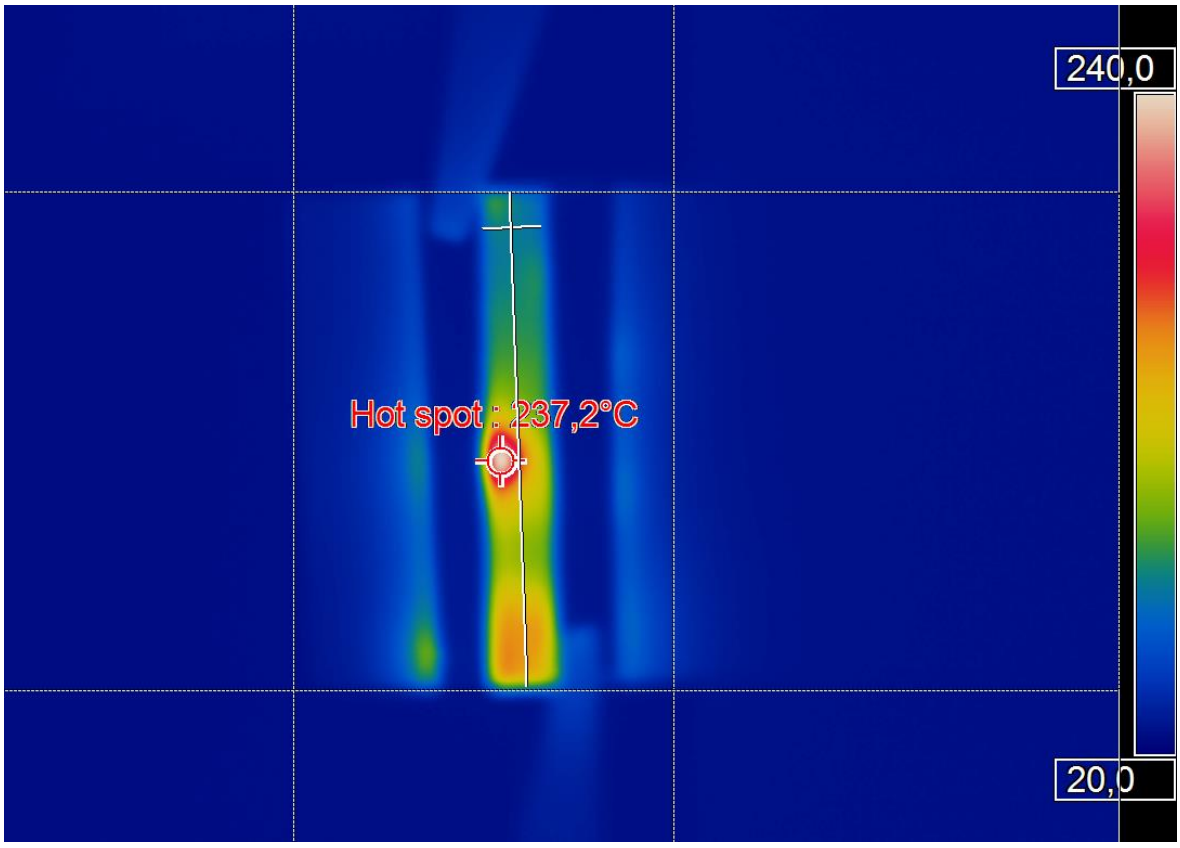

BU 81 50V

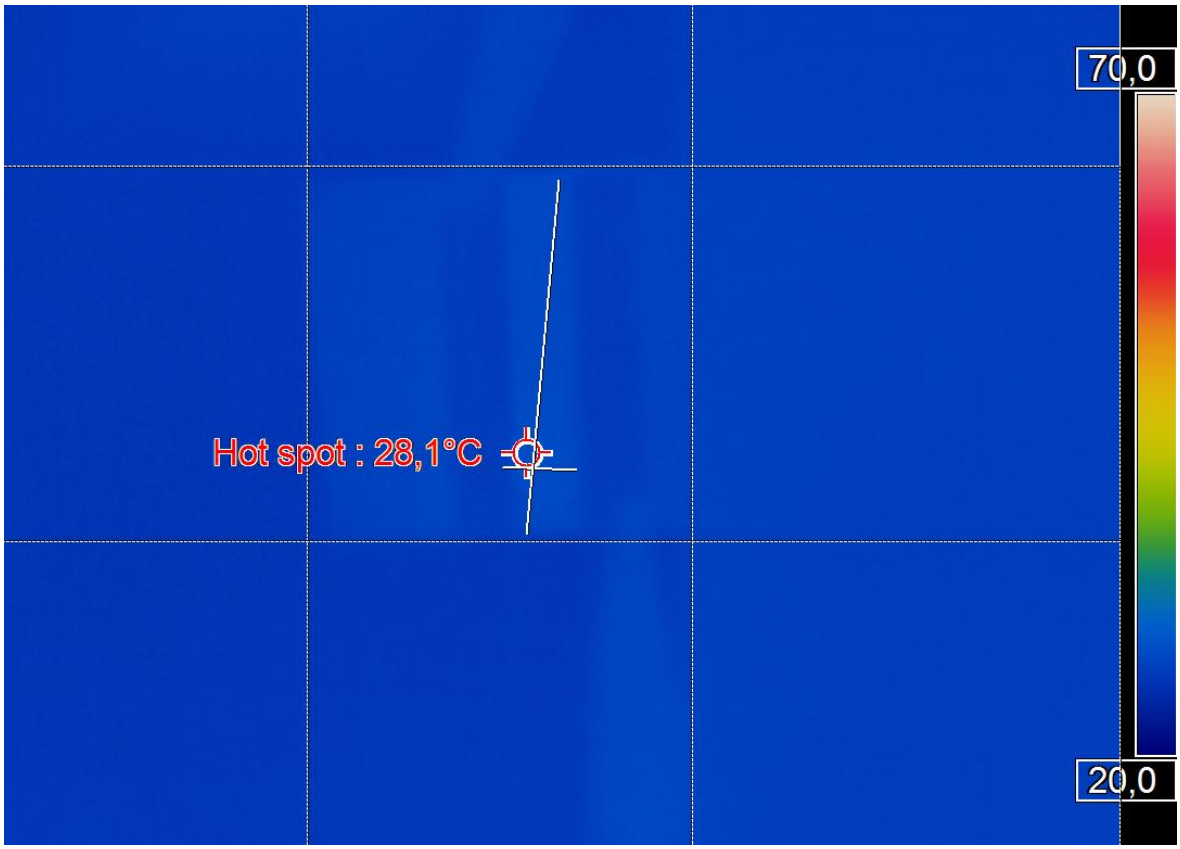

BU 81 100V

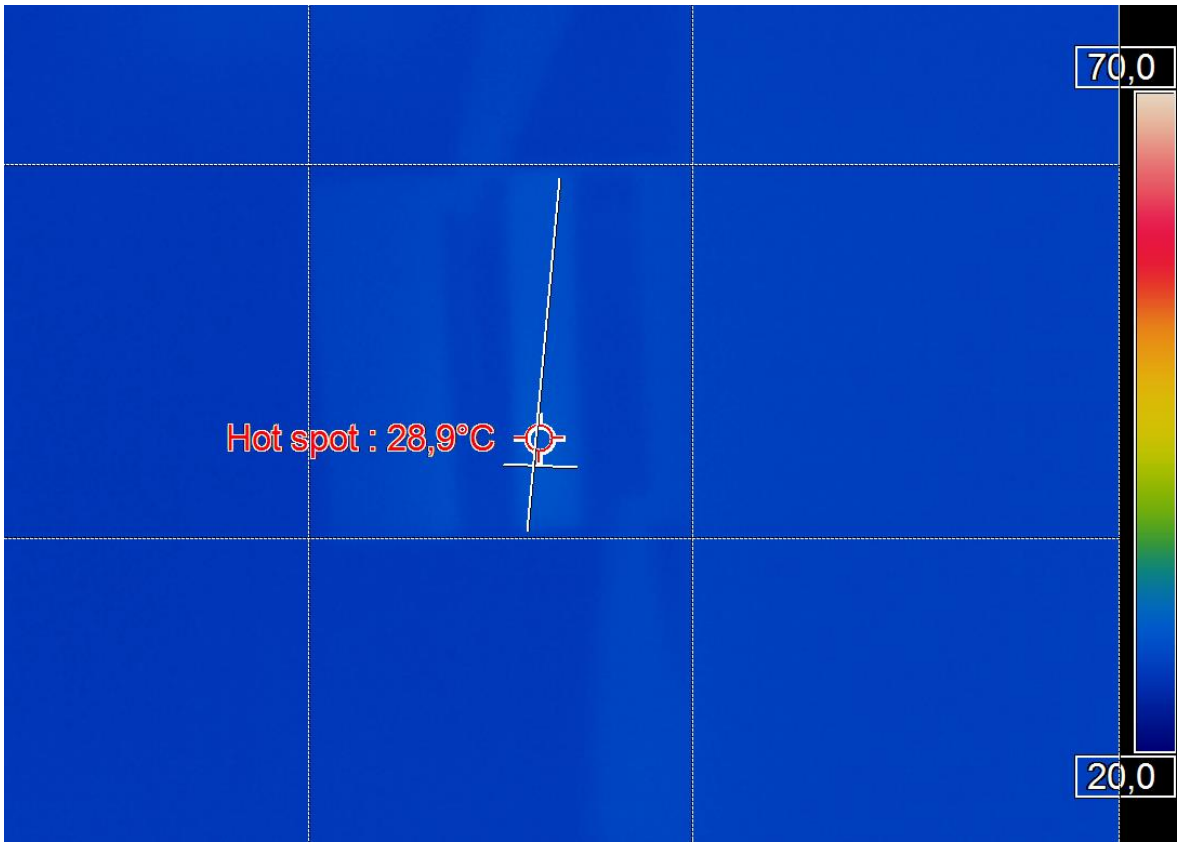

BU 81 150V

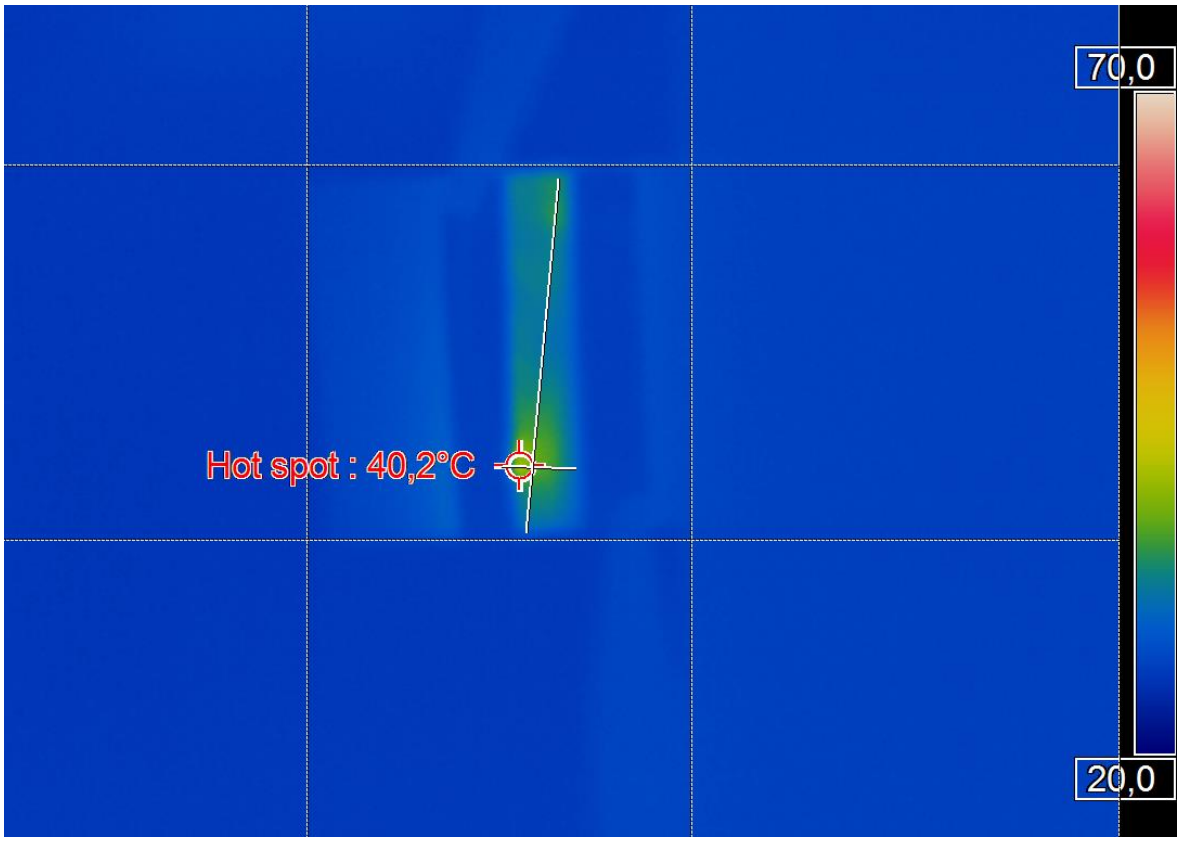

BU 81 200V

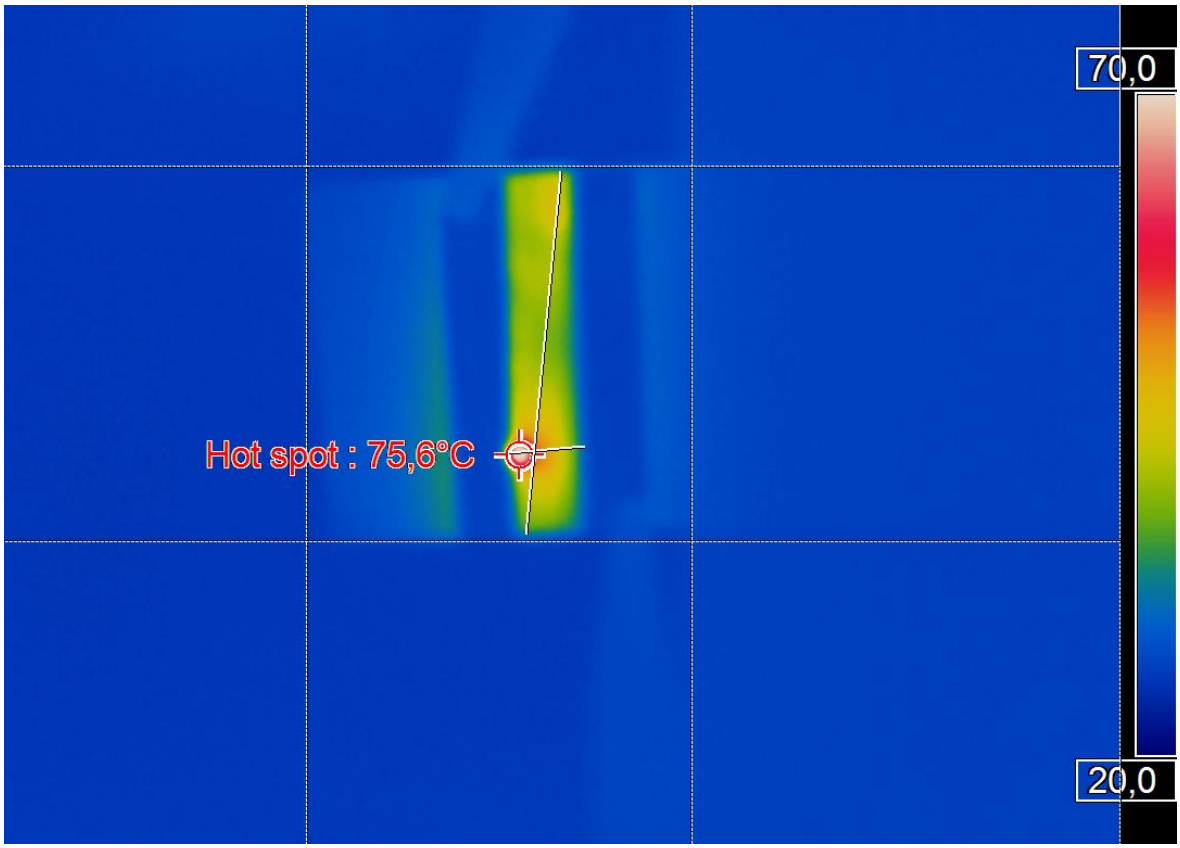

BU 81 250V

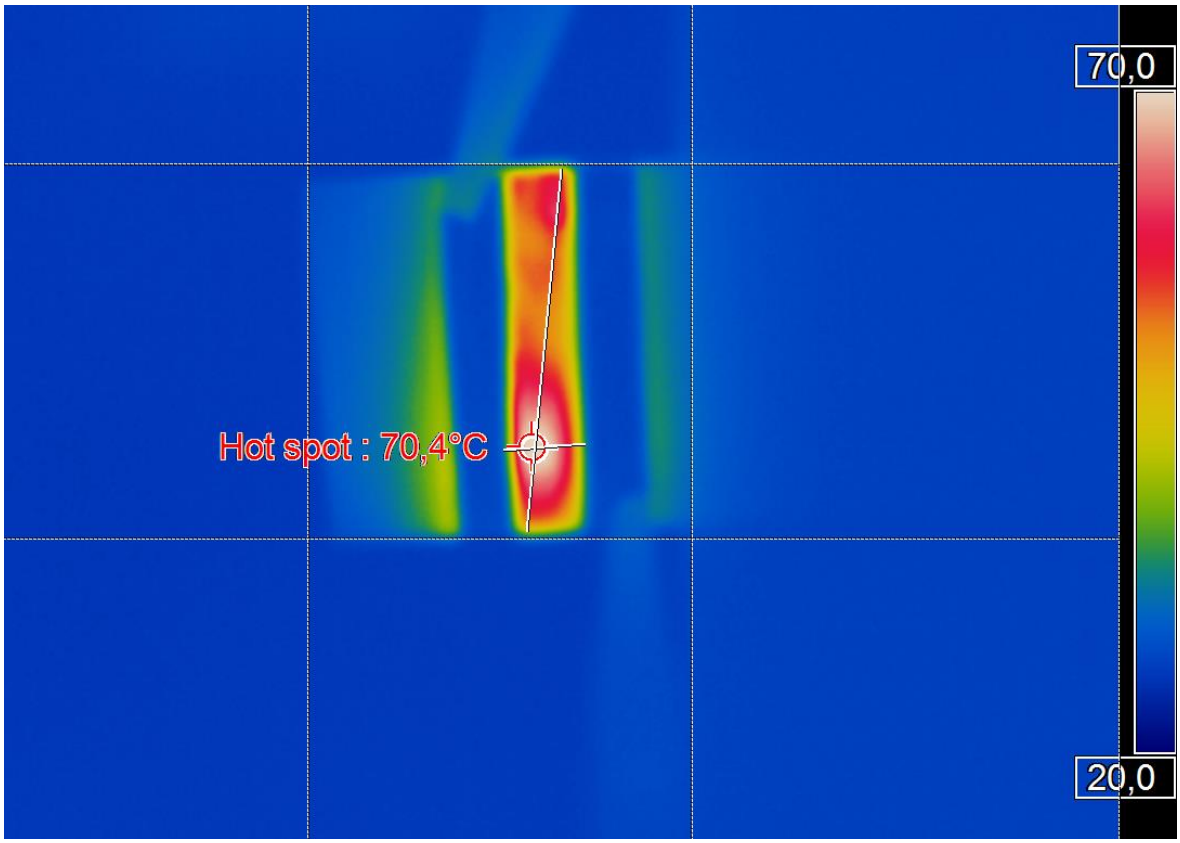

TB 51 50V

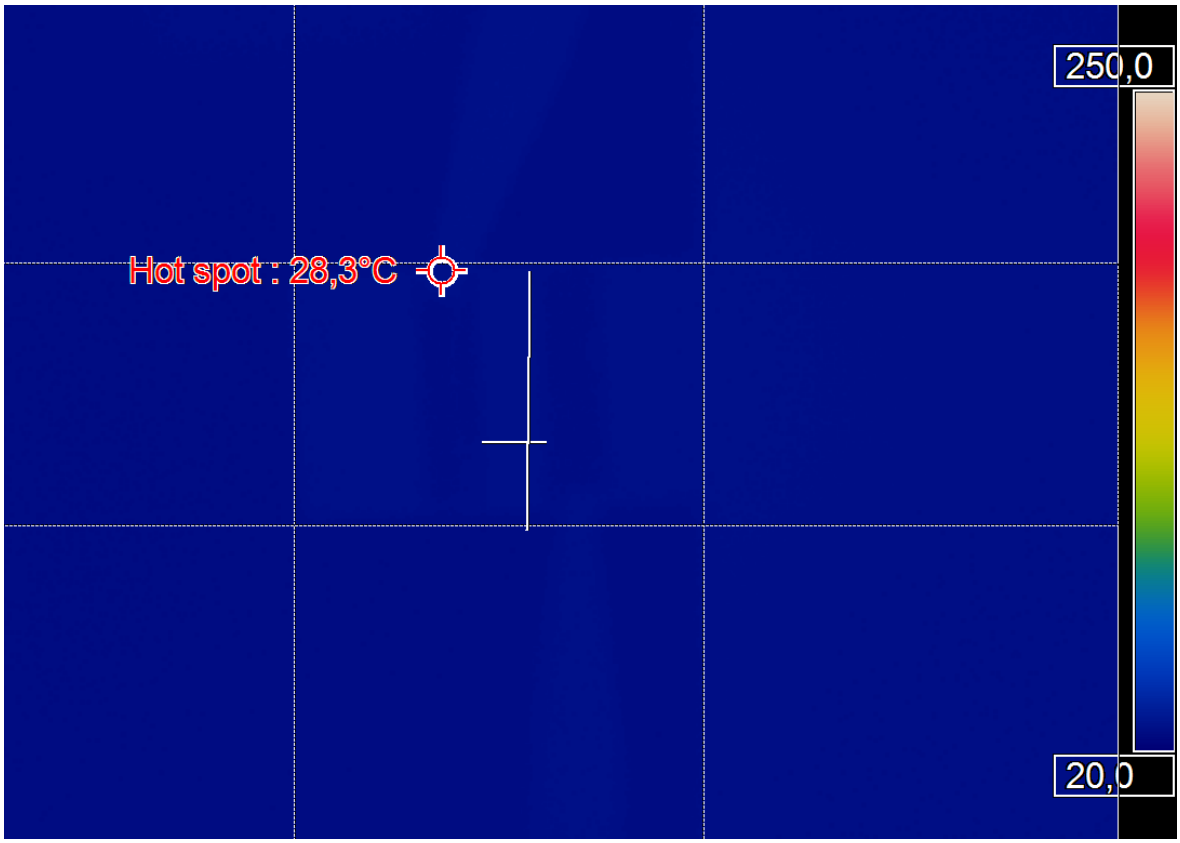

TB 51 100V

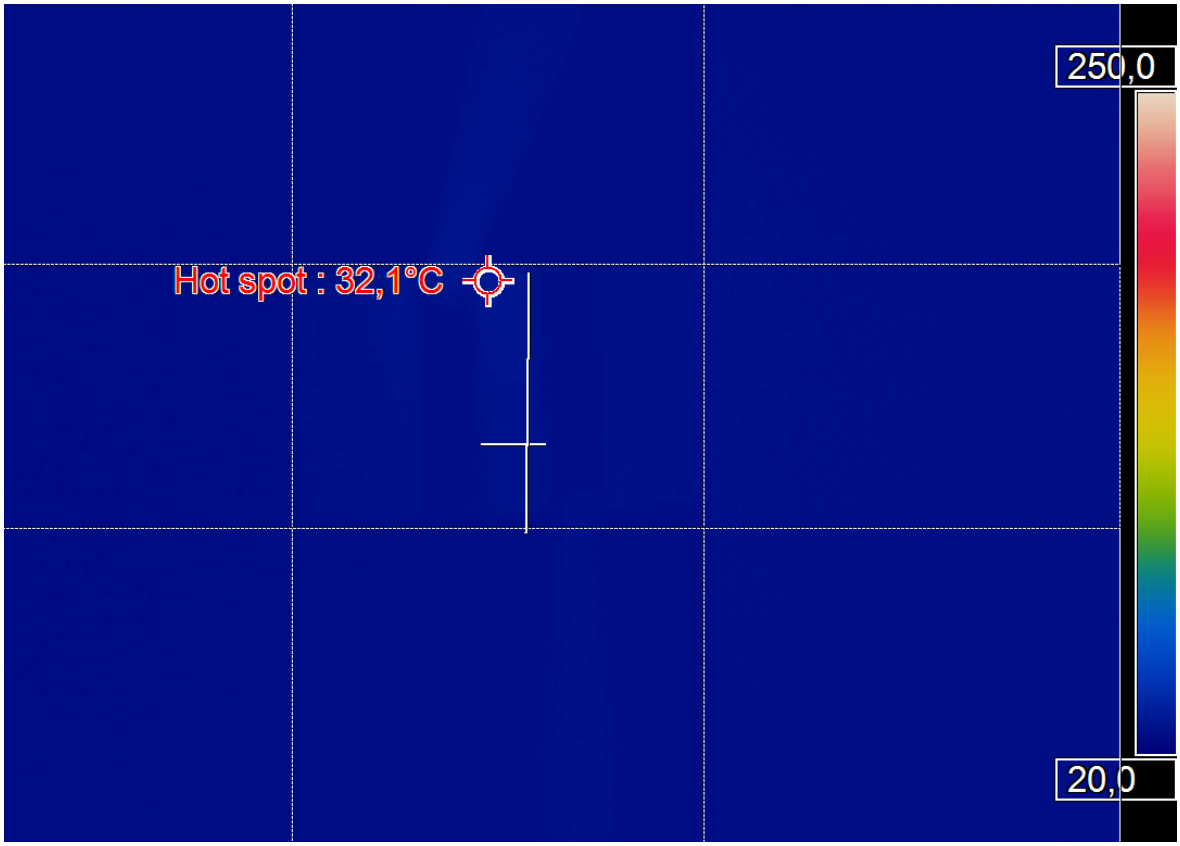

TB 51 150V

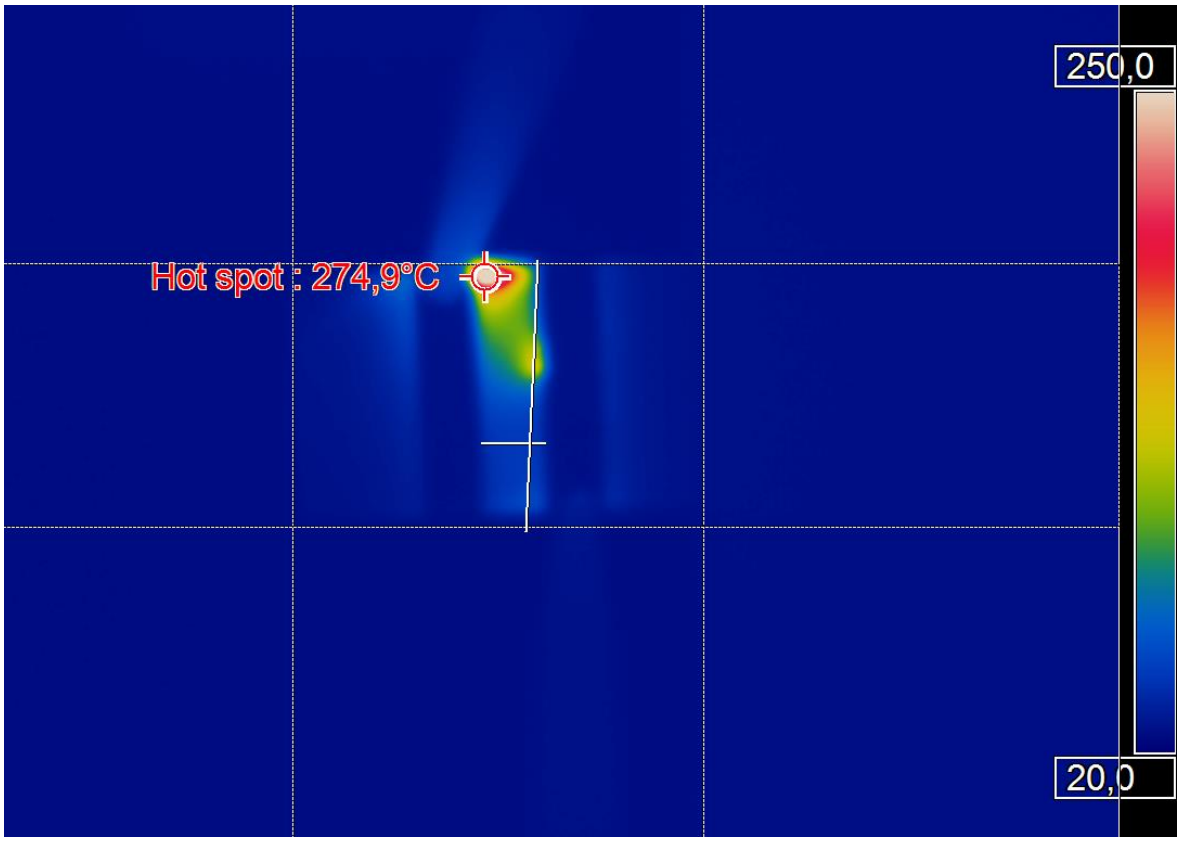

Photos of samples BU 34, BU 81 and TB 51 made with electron microscope

BU 34


410x
15kV - Point
APR 01 2021 13:08
200 µm
656 µm
4.597 mm 60 Pa
BU 84


410x
15kV - Point
APR 01 2021 13:07
200 µm
654 µm
4.549 mm 60 Pa
BU 84

BU 81

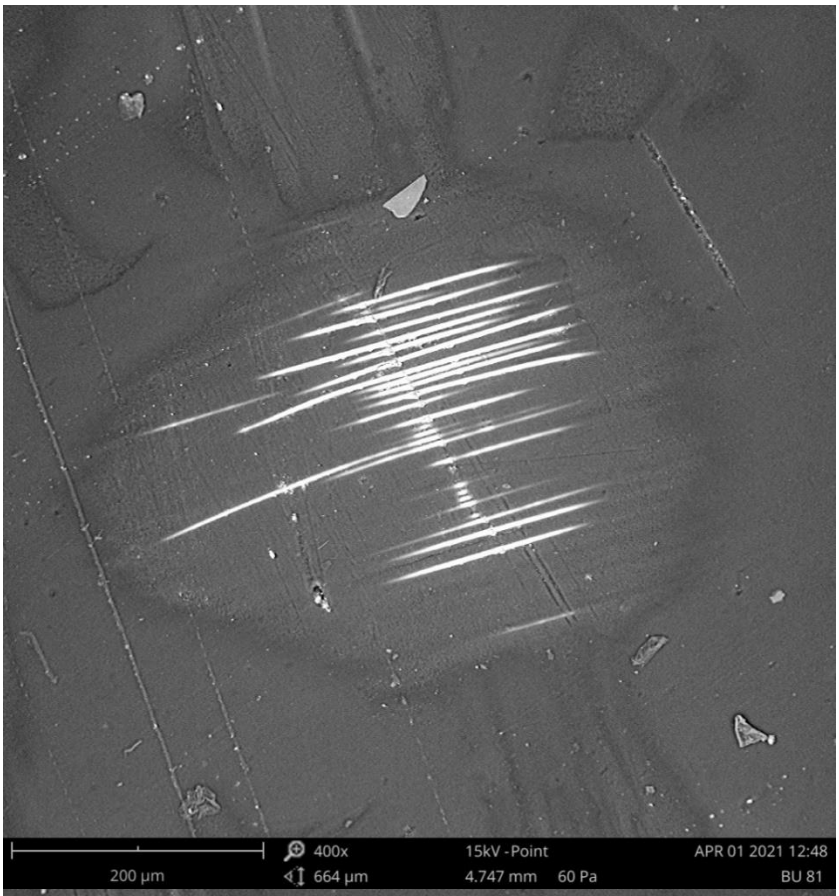
400x
15kV - Point
APR 01 2021 12:48
200 µm
664 µm
4.747 mm
60 Pa
BU 81


410x
15kV - Point
APR 01 2021 12:47
200 µm
661 µm
4.694 mm
60 Pa
BU 81

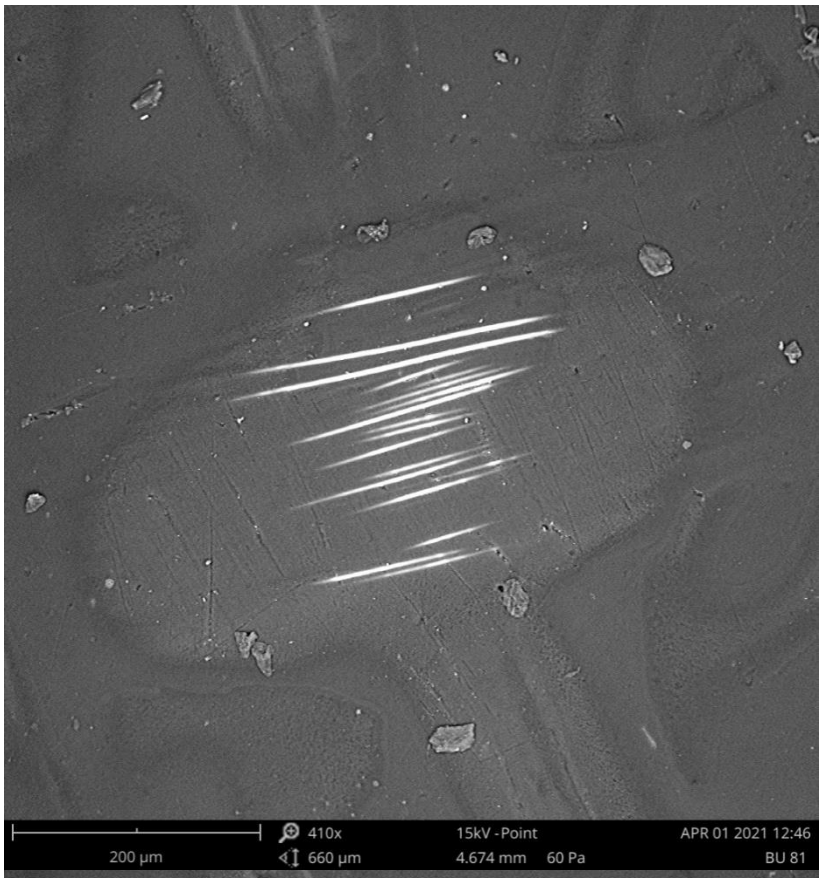
410x
15kV - Point
APR 01 2021 12:46
200 µm
660 µm
4.674 mm
60 Pa
BU 81

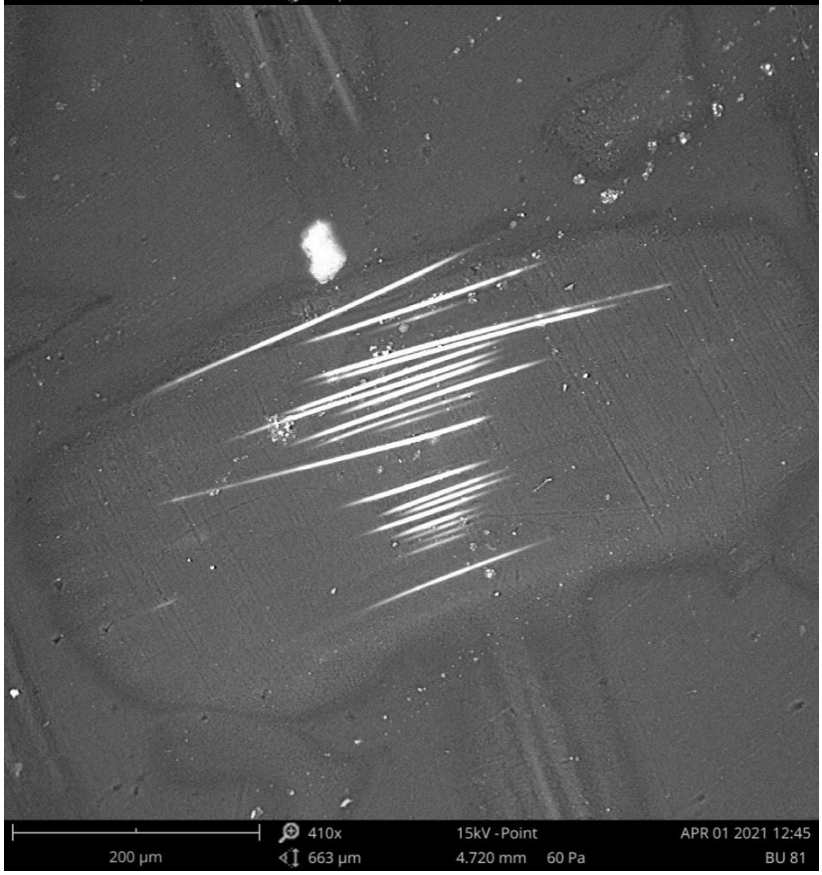
410x
15kV - Point
APR 01 2021 12:45
200 µm
663 µm
4.720 mm
60 Pa
BU 81

TB51

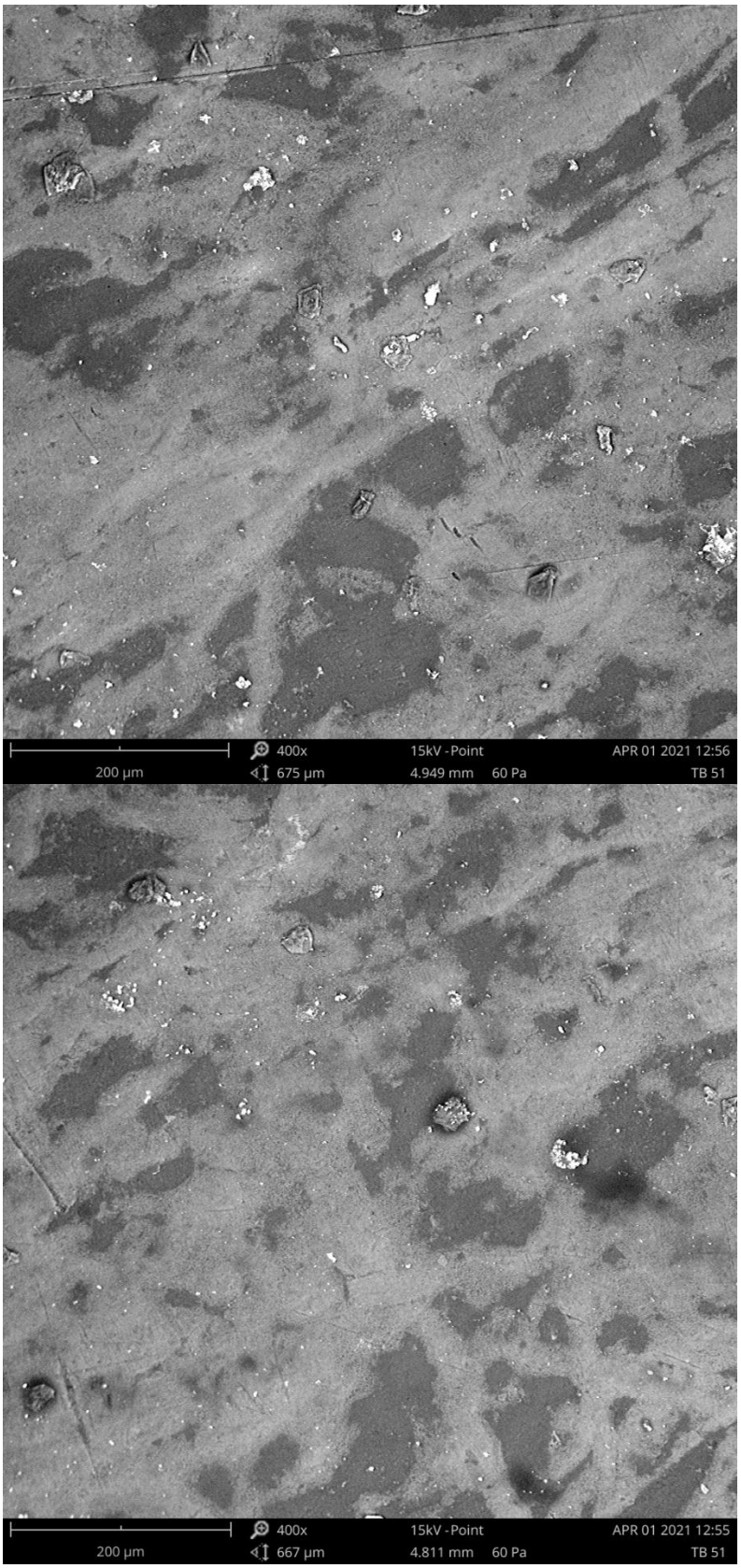
400x
15kV - Point
APR 01 2021 12:56
200 µm
675 µm
4.949 mm
60 Pa
TB 51
400x
15kV - Point
APR 01 2021 12:55
200 µm
667 µm
4.811 mm
60 Pa
TB 51

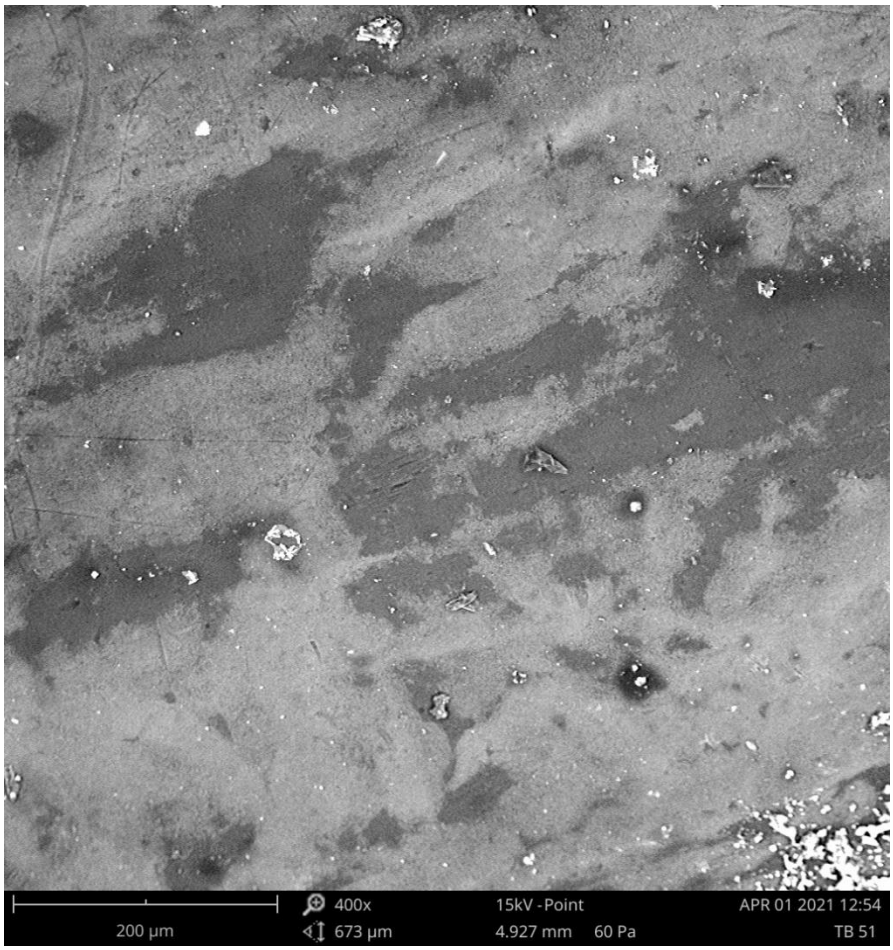
400x
15kV - Point
APR 01 2021 12:54
200 µm
673 µm
4.927 mm
60 Pa
TB 51